Experimental study of the atrial septal puncture, linear ablation, and monophasic action potential contact force resulting in proposed medical device enhancements to improve ablation procedure outcomes

A DISSERTATION SUBMITTED TO THEFACULTY OF THE UNIVERSITY OF MINNESOTA BY

Mark A Benscoter

IN PARTIAL FULFILLMENT OF THE REQUIREMENTS FOR THE DEGREE OF DOCTOR OF PHILOSOPHY

Dr. Paul A. Iaizzo, PhD

May 2015

Acknowledgements

First, I would like to thank the University of Minnesota for the opportunity and more specifically my advisor Dr. Paul Iaizzo PhD and my mentor Dr. Timothy Laske PhD. I'd also like to thank Dr. William Durfee PhD, Dr. Art Erdman PhD, and Dr. Anthony Weinhaus PhD as part of the review committee. Thanks for their guidance and suggestions that helped shape this work.

These studies were conducted in partnership with a great team of collaborators. I would like to thank that group; Dr. Chris McLeod, MB, ChB, PhD, Dr. Boaz Avitall, MD, PhD, Dr. Steve Howard PhD, Dr. Chris Rolfes PhD, Steve Quallich, Megan Schmidt, Lars Mattison, Dr. Ryan Goff PhD, Dr. Julianne Spencer PhD, Monica Mahre, and Tinen Iles for your support in the creation of this work.

Finally, I would like to thank my family (Cathy, Sam, William, Matt, and Marin), my parents (Walt and Kate Benscoter, Carl and Virginia Anderson) for their ongoing support to allow me to have the ability to spend time on this effort. Their support allowed me to conduct this research.

Dedication

This thesis is dedicated to my wife Catherine, for her kindness and for her endless support.

Thesis Abstract

Background: This thesis presents novel research relative to medical device enhancements used to improve the treatment of atrial fibrillation. Specifically, atrial septal punctures, mitral isthmus linear ablations, and the recording of monophasic action potentials all retain important roles in overall procedure success for the clinical intervention of atrial fibrillation using an ablative therapy. The fundamental premise for these medical device innovations is to improve procedural safety and therapeutic outcomes. The continued development of clinical tools and approaches for such procedures will require medical device innovators to understand variability in underlying patient anatomies. I believe this thesis provides critical insights on underling anatomic features and engineering parameters that could dictate how such innovations could be advanced.

Approach: My thesis is composed of a series of studies that focus on: 1) characterizing device efficacy for transseptal puncture; 2) improvements in device utilization for the creation of linear lesions in the region of the mitral isthmus; 3) detailed descriptions of proposed ablation procedural approaches that provide critical insights as to potential effect on adjacent anatomies; and 4) applications of innovative monitoring tools to collect monophasic action potentials and associated contact forces, thereby enhancing detection of arrnythmogenic myocardium therapeutic targets and resultant lesion formations.

Specifically, fossa ovalis anatomy was evaluated using swine and human specimens;

direct assessments of fossa ovalis biomechanical properties were performed and means to perform transseptal puncture procedures were identified. To accomplish this, I developed novel methodologies for assessing both puncture and tear. I also sought to determine the relative utility of employing the swine fossa ovalis as a predictive indicator for human tissue responses. Further, novel approaches were evaluated against a set of clinically available puncture devices, e.g., those that use either mechanical or radiofrequency puncture approaches. The specimens were also subjected to different sized sheath devices as another means to better understand the relative properties of the given species' septal anatomy for eliciting punctures and/or tearing.

In another set of studies described within my thesis, using human cardiac tissue, a new procedural technique (with currently available clinical devices) was developed as a means to potentially augment a physician's ability to generate effective linear lesions in the regional anatomy of the mitral isthmus; it was possible to assess such approaches within human cardiac specimens as well. Additionally, magnetic resonance imaging was employed on multiple perfusion-fixed human specimens to provide detailed associated anatomies of the mitral isthmus and coronary sinus, as a means to provide important insights to both clinicians and medical device designers regarding improved procedural approaches taking into consideration collateral structures as well as next generation ablative devices.

Finally, I have described experimental approaches to record monophasic action potential

contact force data using custom constructed catheters. It was shown that this approach allowed me to evaluate how varied cardiac anatomies may affect a user's ability to collect reproducible monophasic action potentials as a means to obtain important clinical information during a clinical ablative procedure.

Summary: In this thesis, I have shown that the fossa ovalis anatomy of the swine can serve as a useful surrogate, within the range of responses that one may encounter clinically in humans. Furthermore, I have also shown what the impact may be of utilizing various methods for performing transseptal puncture procedures, as well as, the relative impact of employing a range of delivery catheter sizes. I consider that the results of the novel studies I describe here will contribute to the future of individuals working in this field, to develop safe transseptal devices that will also reduce damage of associated anatomies. Further, I describe unique ablative procedural techniques as well as various device improvements which could specifically improve therapeutic outcomes for creating linear mitral isthmus ablation lines. Finally, I describe the required contact forces and other recording parameters that would be needed to appropriately collect monophasic action potentials in various locations throughout cardiac anatomies (endocardial and epicardial). This information should provide novel clinical insights that could then be used to design future tools and/or techniques that may even change how a given ablative procedure is conducted.

Therefore, the overall described experimental outcomes within my thesis will increase

one's understanding of associated cardiac anatomy relative to therapeutic approaches for treating atrial fibrillation and the procedures to do so, and also inspire novel clinical approaches and/or the next generation of catheter-based detection of arrhythmogenic tissue and lesion generation.

Table of Contents

ACKNOWLEDGEMENTS ..... **I**

DEDICATION ..... **II**

THESIS ABSTRACT ..... **III**

LIST OF TABLES ..... **XI**

LIST OF FIGURES ..... **XIII**

1. VISUALIZATION OF CATHETER ABLATION FOR PAROXYSMAL, PERSISTENT, AND PERMANENT ATRIAL FIBRILLATION: IMPACT OF DEVICE AND ANATOMY RELATED FACTORS ON PROCEDURE SUCCESS USING VISIBLE HEART® **1**

PREFACE 2

SUMMARY 3

INTRODUCTION 4

NAVIGATING THE RA 6

Fossa Ovalis *6*

Coronary Sinus *13*

Right Atrial Appendage 15

Ablating left atrial structures: PV, MI, and LAA Roofline *16*

Left atrial pulmonary veins *17*

Left atrial appendage *23*

Mitral isthmus and roofline ablation *25*

CONCLUSION 27

2. MECHANICAL PROPERTIES OF THE FOSSA OVALIS TISSUE DURING TRANSSEPTAL PUNCTURES **28**

PREFACE: 29

SUMMARY 30

Background: *30*

Methods and Results: *30*

Conclusions: *30*

INTRODUCTION 32

METHODS 35

Obtaining tissue and preparation *35*

Catheter and fossa holder method *36*

Tenting and puncture testing *39*

Fossa shear force analyses *42*

Tensile testing *44*

Statistical analyses *45*

RESULTS 45

Tenting studies *45*

Puncture forces: human vs. swine comparisons *46*

Puncture forces: sheath size comparisons *50*
Septal ripping forces *53*
Tensile testing *56*
DISCUSSION 59
STUDY LIMITATIONS 61
CONCLUSION 61

3. IMPACT OF TRANSSEPTAL PUNCTURE FORCE ON THE FOSSA OVALIS: COMPARISON OF 12- TO 23-FRENCH CATHETER DELIVERY SYSTEMS AND USE OF TRADITIONAL AND RADIOFREQUENCY NEEDLES 63
PREFACE 64
SUMMARY 65
Background *65*
Objective *65*
Methods *66*
Results *66*
Conclusions *66*
Keywords *66*
Abbreviations *66*
BACKGROUND 67
METHODS 68
Study population *68*
Puncture devices *69*
Force testing *70*
FO puncturing *71*
Septal tearing *73*
Statistical analysis *74*
RESULTS 74
FO puncturing *76*
Septal tearing *79*
Anatomic variation *81*
Anatomy for puncture 81
FO puncturing 81
Septal tearing 83
DISCUSSION 84
FO puncturing *84*
Septal tearing *86*
Study limitations *87*
CONCLUSION 88
ACKNOWLEDGMENTS 88

4. VISUALIZATION OF AN INNOVATIVE APPROACH FOR MITRAL ISTHMUS ABLATION 89
PREFACE 90
INTRODUCTION 91

EXPERIMENTAL SETUP 91
DISCUSSION 95
CONCLUSION 97
APPENDIX A 97
APPENDIX B 97
KEY TEACHING POINTS 98

5. ANATOMIC INFLUENCES ON CATHETER ABLATION EFFECTIVENESS: CREATION OF MITRAL ISTHMUS LINEAR LESIONS IN HUMAN HEART SPECIMENS FROM PATIENTS WITH ATRIAL FIBRILLATION 99
PREFACE 100
SUMMARY 102
Background: *102*
Methods: *102*
Results: *102*
Conclusions: *103*
INTRODUCTION 104
METHODS 106
MRI with Anatomic Reconstructions and Measurements *107*
CS vasculature anatomy *107*
MI morphology *110*
Statistical analysis *111*
RESULTS 111
Study specimens *111*
CS vasculature anatomy *112*
MI morphology *112*
DISCUSSION 114
Major findings *114*
CS vasculature anatomy *114*
MI morphology *115*
STUDY LIMITATIONS 117
CONCLUSIONS 117

6. IN VIVO CATHETER CONTACT FORCE AND CORRELATION WITH MONOPHASIC ACTION POTENTIALS IN EPICARDIAL AND ENDOCARDIAL ANATOMIC LOCATIONS 119
PREFACE 120
SUMMARY 121
Background: *121*
Methods: *121*
Results: *121*
Conclusion: *121*
INTRODUCTION 123
METHODS 126

Study population *126*
Mapping procedure 131
Contact force measurement 132
Statistical analysis 132
RESULTS 133
Epicardial and endocardial mapping *135*
Epicardial RV mapping *137*
Endocardial mapping *139*
Variation from heart to heart *140*
Anatomic point variation *142*
DISCUSSION 146
Study limitations *147*
CONCLUSION 148
ACKNOWLEDGEMENTS 148

7. ASSESSING THE INTEGRITY OF FORMED CARDIAC LINEAR LESIONS BY RECORDING FOCAL MONOPHASIC ACTION POTENTIALS AND CONTACT FORCES: A TECHNICAL BRIEF 149
PREFACE 150
SUMMARY 151
INTRODUCTION 152
METHODOLOGY 152
CONCLUSION 159

THESIS SUMMARY 160
REFERENCES 166

List of tables

Table 2.1 Baseline characteristics of human hearts (n=7) 35

Table 2.2 Size and dimensions of catheters. 38

Table 2.3 Summary of fossa ovalis dimensions and sheath tearing forces listed by sheath size. 53

Table 2.4 Directional differences in septal tearing forces using a 12F sheath 54

Table 2.5. Summary of tensile testing stress, strain, and Young's modulus . 56

Table 3.1 Dilator dimensions 70

Table 3.2 Sheath dimensions 70

Table 3.3 Baseline tearing characteristics by needle type. 80

Table 3.4 Baseline tearing characteristics by sheath size. 80

Table 3.5 Anatomic measurements of the fossa ovalis 82

Table 3.6 Baseline fossa ovalis characteristics by needle type. 83

Table 3.7 Baseline fossa ovalis characteristics by sheath size. 83

Table 5.1 Donor characteristics (n = 30) (mean ± standard deviation) 111

Table 5.2 CS anatomic measurements, mm (n = 30) 112

Table 5.3 MI anatomic measurements, mm (n = 30) 113

List of Figures

Figure 1.1 In this image of the RA, all of the 5 locations shown on the FO are transseptal puncture possibilities. The green arrow depicts the path of device delivery to the FO. CS Os – coronary sinus ostium, ER – eustachian ridge, FO – fossa ovalis, IVC – inferior vena cava, RA – right atrium. 7

Figure 1.2 In the diagram on the left (A), the green arrows depict the IVC approach to transseptal punctures. The image on the top right (B) shows the FO and ER. The image on the bottom right (C) shows a patent foramen ovale in the FO, with the ER adjacent to the FO. ER – eustachian ridge, FO – fossa ovalis, IVC – inferior vena cava . 8

Figure 1.3 This image shows the catheter dilator and sheath in the RA. The red rectangle contains pectinated muscles that border the ER. ER – eustachian ridge, RA – right atrium 9

Figure 1.4 The image on the left (A) shows deformation of the FO at the point of needle puncture in the LA. The image in the center (B) shows a transseptal puncture at the time of dilator insertion, with deformation of the FO (red oval) and a tight fit between the dilator and the FO. The image on the right (C) shows 3 areas: 1, the septal ridge around the FO; 2, the thin and highly compliant nature of the FO; and 3, the ER. ER – eustachian ridge, FO – fossa ovalis 10

Figure 1.5 The image on the left (A) shows the view from the LA of the FO at the point of needle puncture. The image on the right (B) shows the simultaneous view from the RA at the point of needle puncture. FO – fossa ovalis, LA – left atrium, RA – right atrium 11

Figure 1.6 In the diagram on the left (A), the green arrows depict the path of device delivery to the PV originating from the FO. The image on the right (B) shows LA sheath placement after a transseptal puncture, with a guidewire introduced into the RSPV. FO – fossa ovalis, LA – left atrium. PV – pulmonary vein 11

Figure 1.7 Example of potential complication as a result of catheter navigation performed in a swine showing FO tearing due to excessive deflection force from a delivery sheath attempting to navigate into a PV. 12

Figure 1.8 In the diagram on the left (A), the green arrows depict the device approach originating from the IVC into the CS ostium. The image on the right (B) shows the regional anatomy in the area of the CS bordered by the thebesian valve, including the IVC catheter introduction point. CS – coronary sinus, IVC - inferior vena cava. 14

Figure 1.9 In this image, the green arrow depicts the device approach originating from the IVC. IVC = inferior vena cava 15

Figure 1.10 The diagram on the left (A) shows the approach to the RAA through the IVC. The image on the top right (B) shows the large size of the RAA and pectinated muscles. The image on the bottom right (C) shows the pectinated muscles and thin tissue. 16

Figure 1.11 In the diagram on the left (A), the green arrows depict the directions of device introduction originating from the FO into the LA pulmonary anatomy. The image on the top right (B) shows the left PV ostium. The image on the bottom right (C) shows the right PV ostium. FO – fossa ovalis, LA – left atrium, PV pulmonary vein 18

Figure 1.12 The image on the left (A) shows the catheter sheath and the use of a guidewire for placement into the RSPV. The image in the center (B) shows the introduction of the catheter tip at the PV ostium. The image on the right (C) shows the retraction of the catheter sheath to the FO and the introduction of a balloon catheter.FO – fossa ovalis, RSPV – right superior pulmonary vein, PV – pulmonary vein 20

Figure 1.13 The image on the left (A) shows the catheter sheath and the use of a guidewire for placement into the LSPV. The image in the center (B) shows the placement of the guidewire into the PV ostium. The image on the right (C) shows the introduction of the balloon catheter across the LA. LA – left atrium, LSPV – left superior pulmonary vein, PV – pulmonary vein 21

Figure 1.14 In this image of a balloon-based LA RSPV occlusion, the sheath is

retracted to accommodate the ablation catheter (red circle). The catheter orientation (green arrow 1) is not aligned with the PV ostium orientation (green arrow 2). LA – left atrium, PV – pulmonary vein , RSPV – right superior pulmonary vein. 22

Figure 1.15 In the diagram on the left (A), the green arrow indicates the approach to the LAA from the FO. The image on the top right (B) shows the position of the LAA relative to the MVA and the presence of pectinated muscle. The image on the bottom right (C) shows the position of the LAA relative to both the MV and the LSPV.FO – fossa ovalis, LAA – left atrial appendage, LSPV – left superior pulmonary vein, MV – mitral valve 23

Figure 1.16 This image shows the catheter shaft circulating around the LAA ostium; the red circle depicts the ridge between the LAA and LSPV. LAA – left atrial appendage, LSPV – left superior pulmonary vein 24

Figure 1.17 The diagram on the left (A) shows the MV in the LA. The image (B) notes various structures, including the MVA, which serves as the starting point for creating a linear lesion in the MI. LA – left atrium, MV – mitral valve, MVA - mitral valve annulus. 25

Figure 1.18 The image on the left (A) shows MI lesion creation originating at the MVA. The image on the right (B) shows creation of a roofline linear lesion. MI – mitral isthmus, MVA – mitral valve annulus. 26

Figure 2.1 Radial adhering suction device for stabilization of the atrial septum for tissue puncturing. (A) Force testing machine with transseptal device attached and puncturing the atrial septum. (B) Close-up view of the atrial septum and stabilization device employed for puncturing. 37

Figure 2.2 Schematic of transseptal devices used for testing. The dilator was seated into the sheath and attached at the proximal end via adhesive. The center lumen was kept clear for a needle to be placed through it and protrude from the distal tip. 39

Figure 2.3 Location of the fossa ovalis (FO) in relation to other anatomy within the right atrium (RA): the inferior vena cava (IVC), and the coronary sinus ostium (CS Os). The numbers indicate various puncture locations: (1) center, (2) inferior, (3) posterior, (4) superior, and (5) anterior. 40

Figure 2.4 Characteristic force verses distance graph during fossa ovalis puncturing. Note the distinctive peaks during each transition of the dilator and sheath; upon reaching a new layer, the force increases due to the need for fossa ovalis expansions. . . 42

Figure 2.5 Schematic representation of the fossa ripping test setup. The muscular tissue adjacent to the septum primum (posterior rim of the fossa ovalis for posterior pulls and superior rim for inferior pulls) was cut off to allow the sheath to fully disengage from the atrial septum without consequence from the muscular portion of the atrium surrounding the floor of the fossa ovalis (A). The fossa ovalis was ripped by a catheter which was inserted through the floor of the fossa ovalis in the mechanical force tester (B). An example of the resultant force versus extension plot is shown in (C). 44

Figure 2.6 Example of prepared dog-bone shaped sample used for testing (A) and with 2-0 silk suture attached while mounted in the testing pull tester (B). . . . 44

Figure 2.7: Forces required to tent the fossa ovalis by 8mm. Experiments were performed on excised human (n=8) and swine (n=40) hearts. (*=$p<0.01$, **=$p<0.001$) 46

Figure 2.8 Average peak forces required to pass various portions of 10F sheath through the septum primum in isolated septa of human and swine hearts. Significant differences were found between these two species when comparing the tip of the dilator, dilation, and sheath forces (*=$p<0.01$, **=$p<0.001$) 47

Figure 2.9 Histogram of recorded peak forces required to traverse the septum with various portions of a 10F sheath. 49

Figure 2.10 Relative forces required to traverse the atrial septum with various portions of a transseptal sheath of difference sizes. (Ŧ=$p<0.001$ based on ANOVA) 50

Figure 2.11 Minimum and maximum diameters of induced iatrogenic atrial septal defects, following transseptal punctures employing various sized catheters. 51

Figure 2.12 Relative forces required to transition a catheter system through a septum from one portion of the transseptal puncture sheath to another. An increase in the cross-sectional area of the relative portions of the catheter required more force to pass the catheter through a given septum. 53

Figure 2.13 Catheter size versus average tearing force. Tearing forces of the fossa ovalis increased with the usage of a larger diameter sheath, but did not significantly differ between the 4F and 12F sheaths (p>0.05). Error bars depict mean±SE. *p-value<0.001 55

Figure 3.1 The photo on the left (A) shows a swine heart's torn fossa ovalis (FO), with a sheath through the opening made by a transseptal puncture, as viewed from the left atrium. The photo on the right (B) shows a human FO puncture, as viewed from the left atrium. 67

Figure 3.2 The photo on the left (A) shows our study's 3 transseptal puncture devices, from top to bottom (scale bar = 1 cm): a 5-French RF electrode with the tip of a transseptal needle (ETN), a radiofrequency transseptal needle (RFTN), and a conventional curved transseptal needle (TN). The diagram on the right (B) depicts the components of the 3 devices (purple = sheath, green = dilator). 69

Figure 3.3 The diagram on the left (A) depicts the setup for transseptal punctures, with the device positioned to be inserted through the fossa ovalis (FO) mounted on a plate; all 3 components—sheath (S), dilator (D), and needle (N)—were oriented perpendicular to the specimen. The photo on the right (B) shows septal tissue prepared for puncture (red oval = the FO). 72

Figure 3.4 The diagram on the left (A) depicts force data (in grams) for all tearing and puncturing, *by needle type*: transseptal needle (TN), radiofrequency TN (RFTN), or 5-French RF electrode with the tip of a TN (ETN). The diagram on the right (B) depicts force data (in grams) for all tearing and puncturing, *by sheath size*: 12-, 16-, 18-, or 23-French. 75

Figure 3.5 The diagram on the left (A) shows, for all specimens, the mean puncture force and standard deviation (SD) (in grams) for the needle, dilator, and sheath *by sheath size*. The diagram on the top right (B) shows, for all specimens, the mean puncture force and SD (in grams) *by needle type*: transseptal needle (TN), radiofrequency TN (RFTN), or 5-French RF electrode with the tip of a TN (ETN). The diagram on the bottom right (C) shows the relationship between dilator and sheath puncture forces with an overall R^2 of 0.29. 77

Figure 3.6 This diagram shows the mean puncture force and standard deviation (in grams) *by needle type and sheath size*. * $P \leq 0.05$ 78

Figure 3.7 The diagram on the left (A) depicts the puncture force (in grams), with data normalized against the transseptal needle (TN) and 12-French size, *by needle type*: TN, radiofrequency TN (RFTN), or 5-French RF electrode with the tip of a TN (ETN). The diagram on the right (B) depicts the transseptal crossing force (in grams) *by sheath size*: 12-, 16-, 18-, or 23-French. 79

Figure 3.8 This diagram depicts the peak septal tearing forces *by sheath size*: 12-, 16-, 18-, or 23-French. The only significant difference occurred when using the 23-French sheath, as compared with the other 3 sizes. *$P < 0.001$ 81

Figure 3.9 This 3-part diagram depicts the relationship between FO thickness (in mm) and puncture force (in grams) using (A) the transseptal needle (TN); (B) the 5-French radiofrequency electrode with the tip of a TN (ETN); and (C) the RFTN. 82

Figure 4.1 Mitral isthmus linear lesion was created in a reanimated human heart: (A) shown in the initiation of linear lesion with support from transseptal sheath and secondary diagnostic catheter; (B) the ablation catheter –1– is pulled along MI with twisting of diagnostic catheter -2- towards FO and retraction of transseptal sheath – 3 – from LA; (C) shown is an increased deflection of ablation catheter – 4 – and increased twisting of diagnostic catheter – 5. The uses of both the transseptal sheath and a support catheter was advantageous to maintain contact on the MI. LA – left atrium, MI – mitral isthmus, MV – Mitral valve, PV – pulmonary vein 92

Figure 4.2 Shown are several views of sectioned and TTC stained left atrial samples: (A) the ablated atrial tissue appear as blanched; (B) shown is the PV inverted and the MI line is circled; and (C) cross-section view of linear mitral isthmus lesion, depicting transmurality. 94

Figure 4.3 Shown is the movement of the catheter using a traditional approach A) catheter tip movement (green arrow) over the ridge (blue dash) B) catheter tip drag (green arrow) starting a MI in the direction of the ridge (blue dash). . . 96

Figure 5.1 Schematic diagram of the cross-section along the mitral isthmus (MI) from the mitral valve annulus to the left inferior pulmonary vein (LIPV). The blue vessel represents the coronary sinus (CS); the red vessel, the left circumflex artery. 1 indicates the long and thick MI; 2, the recess/pouch/crevice; 3, the muscular sleeve around the CS; 4, convective cooling by blood flow in the CS and the artery; 5, the 0° position of the CS circumference. 105

Figure 5.2 Anatomic reconstruction of the left atrium (LA), coronary sinus (CS),

and left inferior pulmonary vein (LIPV). The yellow mitral isthmus (MI) plane line intersects the CS center line as measured in the reconstructed 3-dimensional model. The light blue line depicts the CS center line. 108

Figure 5.3 A magnetic resonance imaging (MRI) image (left) and a photograph of the same human heart specimen (right). The left atrium (LA) endocardial space is labeled (left atrium). The specimen section includes the coronary sinus (CS); immediately inferior to it is a deposit of fat that is visible on both the MRI image and the photograph. 109

Figure 5.4 Analysis of the coronary sinus (CS) at the mitral isthmus (MI). The 0º to 180º line is parallel to the mitral annulus. Using the CS center line, we created degree positions around the CS (0º, 90º, and 180º), in order to measure distances to the endocardial MI. The left atrium (LA) and left ventricle (LV) are labeled for reference. 110

Figure 5.5 Presence of fat and distance to mitral isthmus (MI) at the position of the coronary sinus (CS) at the MI plane, in degrees around the CS: red, atrial fibrillation (AF) group; blue, non-AF group. (A) Distance around the CS at the MI plane to the left atrium (LA) space, in mm. (B) Bar chart comparing the percentage of hearts where fat was present, next to different positions on the CS. The shortest label (–) compares the 0° AF position with the shortest (15°) non-AF position. 113

Figure 6.1 Epicardial sites for CF/MAP signals collection. RVOT = right ventricular outflow tract, RV = right ventricle, LV = left ventricle RAA = right atrial appendage, CS = coronary sinus, RA = right atrium 127

Figure 6.2 (A) Design of the tip of the MAP catheter (4) with 4 distal electrodes (2) and 2 – 2 mm band electrodes (5) that are mounted on the shaft of the catheter. The tip electrodes are isolated from each other using a polymer (1, 3); the catheter is able to collect both unipolar and bipolar signals. (B) Illustrates the catheter tip as it engages the tissue surface. The electrodes and fiber Bragg grating strain sensor (orange tube) come in contact with the tissue at the same time. Contact is denoted by deformation of the fiber grating in the right panel of (B). This deformation is translated into grams of CF. CF = contact force, MAP = monophasic action potential 128

Figure 6.3 MAP depolarization and repolarization. During phase 0 (depolarization), sodium enters the cell; during phase 2, calcium enters the cell and contraction starts; during phase 3 (repolarization), potassium exits the cell. MAP = monophasic action potential 129

Figure 6.4 (A) Signals that served to define AT, APD, and RT. (B) A single MAP (purple) and ECG (black) signal captured on the RV epicardium. (C) Catheter orientation, direction of motion, and orientation for epicardial measurements. APD = action potential duration, AT = sum of activation time, ECG = electrocardiography, MAP = monophasic action potential, RT = repolarization time, RV = right ventricle 130

Figure 6.5 (A) The catheter contained within the delivery sheath/fixture was oriented to be perpendicular to the epicardial surface of the right ventricle (RV). (B) The catheter's electrode tip and fiber Bragg grating were near the endocardial surface in the right atrium on the Visible Heart® apparatus. 133

Figure 6.6 Catheter tissue CF (including the mean and SD) is depicted at all endocardial and epicardial mapping points. Color bars indicate 100% of measurements by anatomic location; the percentage breakdowns, bands of CF (grams); gray bars, the mean and SD at each anatomic point. At the far right, the number of points by anatomic location is indicated in either an epicardial (Epi) or endocardial (Endo) grouping. CF = contact force, RVOT = right ventricular outflow tract, RV = right ventricle, LV = left ventricle RAA = right atrial appendage, CS = coronary sinus, RA = right atrium, gm = grams 134

Figure 6.7 (A) We collected all of these points, in 7 anatomic locations. (B) We organized the 7 anatomic locations by CF color bands. (C) The blue dot is the mean CF, the grey dots are each observation. CF = contact force, RV = right ventricle, LV = left ventricle RA = right atrium, gm = grams 136

Figure 6.8 Each line represents an individual swine heart (n = 7). The "first 4" point indicates the mean contact force (CF) required to generate 4 consecutive monophasic action potentials (MAPs) across all epicardial anatomic points; the "all on" point, the mean CF when the catheter tip is fully engaged in the tissue; and the "last 4" point, the last 4 consecutive MAPs. 137

Figure 6.9 (A) a total of 9 anatomic locations showing the distribution of CF at each location. (B) 9 anatomic locations by CF color bands. (C) The mean is shown by blue dot, all observations are grey dots within 3 bands for all points. CF = contact force, RVOT = right ventricular outflow tract, RV = right ventricle, LV = left ventricle RAA = right atrial appendage, CS = coronary sinus, RA = right atrium. gm = grams 138

Figure 6.10 CF differences at each epicardial point collection location. (A) CF is shown at the right ventricular outflow tract (RVOT), right ventricular apex

(RV apex), and the left ventricular apex (LV Apex) 3 epicardial points. (B) CF is shown at 4 epicardial septum locations of the RV septum. RVOT = right ventricular outflow tract, RV = right ventricle 139

Figure 6.11 (A) 9 endocardial locations by whether CF was significantly (blue) or nonsignificantly (purple) different from the normalized epicardial reference (yellow). (B) 7 epicardial locations by whether CF was significantly (blue) or nonsignificantly (purple) different from the normalized epicardial reference (yellow) CF = contact force, RVOT = right ventricular outflow tract, RV = right ventricle, LV = left ventricle RAA = right atrial appendage, CS = coronary sinus, RA = right atrium 141

Figure 6.12 The signal on the left had sufficient CF (contact force). The change in the signal as the catheter was removed is depicted on the right: that CF was insufficient to generate monophasic action potentials (MAPs). 143

Figure 6.13 Changing the catheter tip orientation and position changed the contact force (CF) at the same anatomic epicardial location. 146

Figure 7.1 Shown is a depiction of the employed MAP catheter applied to the cardiac tissue: with a TAP moving past the type of the catheter with an amplitude of 30 mV. The simultaneous deflections of the fiber Bragg grating provided the simultaneous force information. TAP - transmembrane action potential, MAP – monophasic action potential 153

Figure 7.2 Imaged of ablations performed on the reanimated swine heart specimens: (A) epicardial linear lesion on the RV with upper oval as external pacing site and lower oval contains tip of MAP catheter, and (B) LA endocardial image showing mitral isthmus linear lesion creation moving towards mitral valve annulus (green arrow). LV – left ventricle, and MV mitral valve RAA – right atrial appendage, RV – right ventricle. 155

Figure 7.3 Elicited epicardial lesion patterns: (A) location of the linear lesion pattern on RV; (B) CF applied in different anatomic locations on or adjacent to the lesion pattern. CF is indicted for each location with red indicating no MAPs were detected and the green indicates that MAPs were elicited. CF – contact force, MAP – monophasic action potential, RV right ventricle. 157

Figure 7.4 Provided here are the noted CFs for the placements of our

assessment catheter at 9 anatomical locations on the endocardium of the LA in the region of the MI. Red bars indicates that no MAP was elicited and green indicates that a MAP recordings were obtained. CFs in grams are listed for each of 9 locations on the lesion. CF – contact force, LA – left atrium, MI – mitral isthmus. 158

1. Visualization of catheter ablation for paroxysmal, persistent, and permanent atrial fibrillation: impact of device and anatomy related factors on procedure success using Visible Heart®

Mark A. Benscoter, MS[1, 3]; Paul A. Iaizzo, PhD[1, 2]

[1] Department of Biomedical Engineering, University of Minnesota (Minneapolis, MN)

[2] Department of Surgery, University of Minnesota (Minneapolis, MN)

[3] Department of Engineering, Mayo Clinic (Rochester, MN)

Corresponding author:
Dr. Paul Iaizzo
iaizz001@umn.edu
University of Minnesota
B172 Mayo, MMC 195
420 Delaware Street SE
Minneapolis, MN 55455
Telephone: (612) 625-9965
Fax: (612) 624-2002

Brief Title: Systematic visualization review of atrial fibrillation ablation procedure

Relationship with Industry: Research contract with Medtronic, Inc. (Minneapolis, MN)

Preface

The inspiration for this study arose as a result of known limitations that originate with the devices that are used in the treatment of atrial fibrillation. The current procedure uses a number of different devices that perform unique steps in the procedure. Each of the devices have inherit limitations that originate from the device design and these limitations are confounded by the anatomy in which they are intended to operate. Variations in the anatomy pose challenges in that a given device design may not be appropriate for all instances of use.

The use of direct visualization in a functional heart uncovers where the limitations may exist in the device tissue interface that are not easily visible under current procedural imaging modalities.

This chapter is designed to review the current procedure and discover opportunities where limitations between device design and anatomy exist such that further study may be conducted to suggest areas of improvement to either the procedure or the device design. The material in this chapter has been submitted to World Journal of Cardiology. For this study, I was responsible for study design, image analysis, and publication creation. Paul Iaizzo provided editing.

Summary

Endocardial access to the left atrium is commonly achieved to treat patients with atrial fibrillation, using different device delivery systems for cardiac ablation. But the large variation in human anatomy presses the limits of existing medical devices. In our unique study, we used direct visualization with Visible Heart® of the device-tissue interface in fresh reanimated human hearts. Our goal was to better understand any opportunities to improve therapeutic approaches.

The visual images we obtained in our study (and feature in this article) allow a more intimate grasp of the key steps required in various ablation procedures and of any limitations of current device designs. These images show the potential risks of conducting transseptal punctures and the difficulties of placing catheter tips in certain scenarios (e.g., when creating circumferential lesions, and potential problems that could occur in attempting to place catheter tips on such anatomies like the mitral isthmus). In our analysis of these images, we focused on where enhancements are needed to refine device functionality.

Keywords: Atrial fibrillation, cryogenic catheter ablation, radiofrequency ablation, transseptal punctures

Abbreviation List: AF = atrial fibrillation, CS = coronary sinus, ER = Eustachian ridge, FO = fossa ovalis, IVC = inferior vena cava, LA = left atrium, LAA = left atrial

appendage, MI = mitral isthmus, MV = mitral valve, MVA = mitral valve annulus, PV = pulmonary vein, RA = right atrium, RAA = right atrial appendage, RIPV = right inferior pulmonary vein, RSPV = right superior pulmonary vein

Introduction

For many years, ablation (either radiofrequency or cryogenic) has been used to treat patients with atrial fibrillation (AF). [1-3] But variations in cardiac anatomy have consistently influenced therapeutic success. [4-8] Different medical device designs have been developed for creating effective lesions in such varied anatomic structures. [9-12] However, in order to apply therapies for left atrium (LA) targets, navigation is first required into the right atrium (RA) and then across the septum.

Reaching the anatomic locations within the left heart was initially made feasible by Cox's maze procedure.[13-16] In such a procedure, each step requires an intimate understanding of the endocardial anatomy.[17] Importantly, the inappropriate placement of devices in any ablation procedure can result in significant unintended consequences, including the creation of ineffective lesions (no transmurality), the need for subsequent ablation procedures, or cardiac tamponade during transseptal punctures.[18-20]

In an effort to reduce the incidence of such unintended consequences, ablation is commonly performed with the assistance of imaging tools such as fluoroscopy or echocardiography. Imaging tools not only help eliminate unintended consequences, such as perforation, but also help ensure occlusion of pulmonary veins (PVs). In addition, the

use of fluoroscopy, angiography, and noncontact mapping has improved the quality of the images.[21] However, no imaging method allows us to directly visualize the device-tissue interface or to take into consideration the impact of accuracy on heart rhythm.[21,22]

In our unique study, we used Visible Heart® methods to directly visualize the device-tissue interface in fresh human hearts reanimated in a clear Krebs-Henseleit buffer (Sigma-Aldrich Corporation, St. Louis, MO), as previously described.[22, 23] Our goal was to better understand any opportunities to improve therapeutic approaches during the key steps of various ablations procedures. The visual images we obtained in our study (and feature in this article) allow a more intimate grasp of the steps required and of any limitations of current device designs.

In particular, the images reveal the interaction of ablation technology with human tissue, providing a sense of the spatial relationship between the device and anatomic structures. In our analysis of these images, we focused on where enhancements are needed to refine device functionality. For purposes of our analysis, we separated the key steps of ablation procedures into 3 distinct image sets, distinguished by the device used and the anatomy: (1) navigating the RA; (2) conducting transseptal punctures from the RA to the LA; and (3) creating lesions and reaching the key anatomic locations in the LA with different type of ablation devices. Delineating the limitations of current devices and pinpointing the major anatomic challenges should prove to be of great importance for both practicing

physicians and medical device designers.[23]

Navigating the RA

Success in navigating the RA has been limited, given the challenging anatomy of key RA structures combined with the limitations of current device design. Endocardial cardiac ablations of the atria commonly originate via access from the inferior vena cava (IVC). An introducer, at the groin, is inserted into the femoral vein and then advanced into the RA. The IVC serves as a low-pressure return path of deoxygenated blood to the RA. Thus, the IVC is a suitable starting point for endocardial procedures because it eliminates risks associated with device introduction. Key ablation procedure structures in the RA include the fossa ovalis (FO), coronary sinus (CS), and right atrial appendage (RAA).

Fossa Ovalis

The FO serves as the access point for ablation of the LA. As devices enter the RA, the Eustachian valve of the IVC forms a bridge between the IVC and the Eustachian ridge (ER) (Figure 1.1).

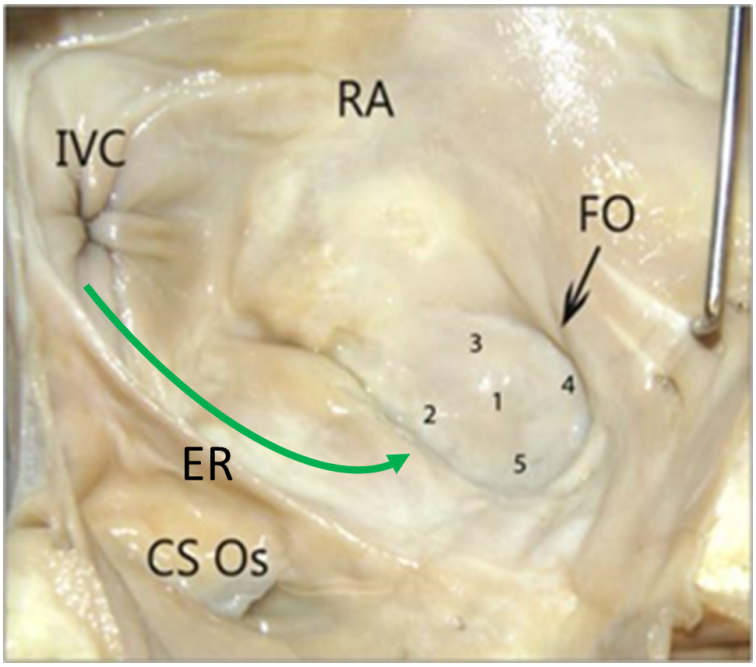

Figure 1.1: In this image of the RA, all of the 5 locations shown on the FO are transseptal puncture possibilities. The green arrow depicts the path of device delivery to the FO. CS Os – coronary sinus ostium, ER – eustachian ridge, FO – fossa ovalis, IVC – inferior vena cava, RA – right atrium.

The FO is also a structure that causes devices to bind or become lodged; device tips can catch on the compliant membrane of the valve. [24, 25, 26] Because the FO and the IVC are located on the superior aspect of the ER, the ER can serve as a guide to facilitate device delivery to the FO, allowing the device to glide along the valve and onto the ER (Figures 1.2B and 1.2C).

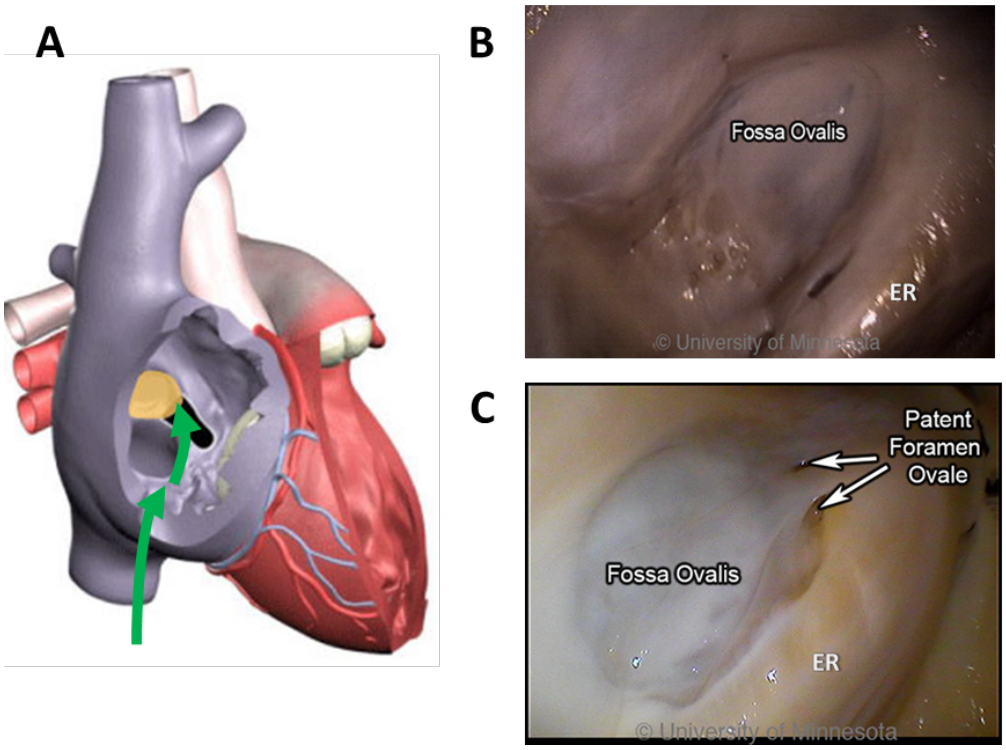

Figure 1.2: In the diagram on the left (A), the green arrows depict the IVC approach to transseptal punctures. The image on the top right (B) shows the FO and ER. The image on the bottom right (C) shows a patent foramen ovale in the FO, with the ER adjacent to the FO. ER – eustachian ridge, FO – fossa ovalis, IVC – inferior vena cava

The ER is a prominent rise between the FO and the CS ostium (Os) [29, 30] The superior and posterior margins of the FO are enfolded to produce the prominent muscular protrusion on the endocardial surface. The FO lies next to the aorta, making transseptal punctures difficult. [31] Bordered by septal tissue and the ER, the FO is typically slightly recessed (Figures 1.2B and 1.2C). These structures can either facilitate or inhibit the operation of a medical device, either directing it in the intended direction or preventing it from being placed in the desired location.

Current catheter delivery systems face challenges in reaching the FO and conducting transseptal punctures. Pectinated muscles adjoin the ER, which itself is pronounced and moves with each contraction. The pectinated muscles adjacent to the FO are composed of undulations that are capable of restraining the tip of a dilator or catheter (Figure 1.3). Dilator tip dimensions are sized to only allow a transseptal needle to pass. This small tip size also increases the chance of binding in these muscles if the tip is placed incorrectly.

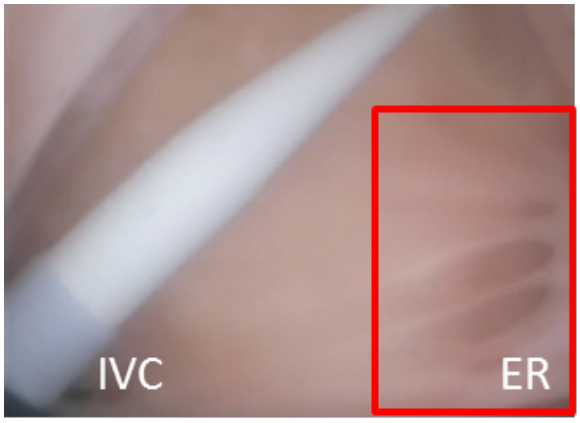

Figure 1.3: This image shows the catheter dilator and sheath in the RA. The red rectangle contains pectinated muscles that border the ER. ER – eustachian ridge, RA – right atrium

During transseptal punctures, the FO is manipulated extensively. Both its size and thickness contribute to changes in the amount of compliance when force is applied (Figure 1.4). A large amount of compliance in the FO, coupled with a lack of compliance in the much thicker septal wall, can result in concentration of the transseptal force on the FO.

Figure 1.4: The image on the left (A) shows deformation of the FO at the point of needle puncture in the LA. The image in the center (B) shows a transseptal puncture at the time of dilator insertion, with deformation of the FO (red oval) and a tight fit between the dilator and the FO. The image on the right (C) shows 3 areas: 1, the septal ridge around the FO; 2, the thin and highly compliant nature of the FO; and 3, the ER. ER – eustachian ridge, FO – fossa ovalis

Dilator tips enable practitioners to confirm anatomic location by tenting the FO. Once tenting is achieved, a transseptal needle can be advanced through the FO (Figures 1.5A and 1.5B). The large amount of tenting that is usually required and the compliance of the membrane draw into question how much force the FO is able to tolerate before the procedure fails. Though necessary to perform transseptal punctures, FO tenting—combined with excess extension of the transseptal needle tip into the LA—can result in a risk of cardiac tamponade.

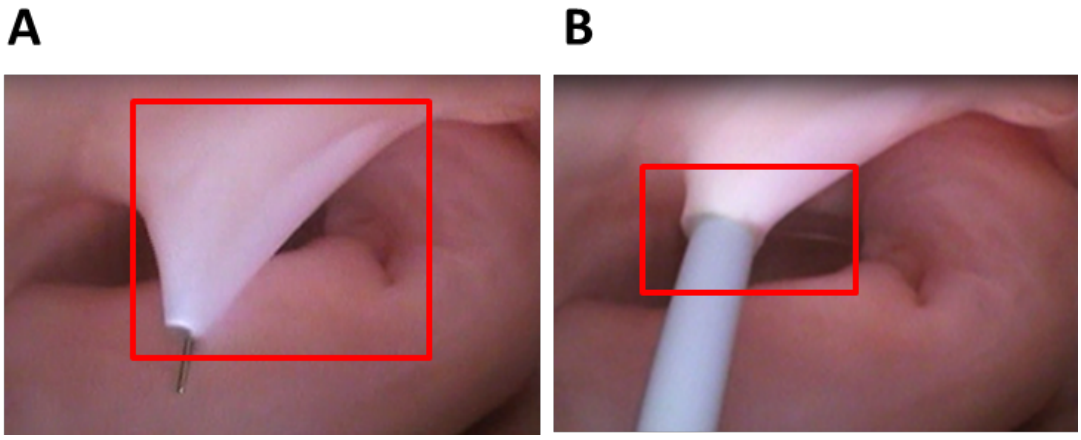

Figure 1.5: The image on the left (A) shows the view from the LA of the FO at the point of needle puncture. The image on the right (B) shows the simultaneous view from the RA at the point of needle puncture. FO – fossa ovalis, LA – left atrium, RA – right atrium

The very close proximity of the FO to both the right superior pulmonary vein (RSPV) and the right inferior pulmonary vein (RIPV) makes it challenging to reorient device tips after transseptal punctures (Figure 1.6).

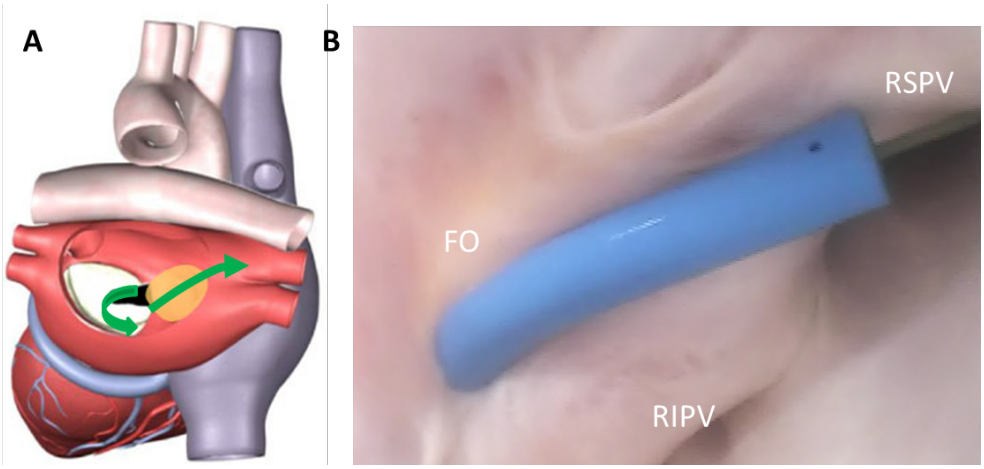

Figure 1.6: In the diagram on the left (A), the green arrows depict the path of device delivery to the PV originating from the FO. The image on the right (B) shows LA sheath placement after a transseptal puncture, with a guidewire introduced into the RSPV. FO – fossa ovalis, LA – left atrium. PV – pulmonary vein

Devices whose total deflection is limited, or whose deflection is located more proximally in the shaft, the resulting tip changes make it impossible to orient the device in a way that facilitates catheter introduction into the right PVs. Consequently, the FO needs to be manipulated more. Moreover, an incorrect puncture site location can increase the difficulty of introducing a catheter into the right PVs.

Once a transseptal puncture is complete, the tissue is stretched over the outside diameter of the dilator and onto the outside diameter of the sheath (Figure 1.5B). This transfer of force, the overall diameter of the sheath, and manipulation of the device in the LA can all contribute to the possibility of tearing the FO. As the sheath is deflected and the device is introduced into the LA, the resulting forces on the sheath push and pull the FO. If these forces become excessive, the FO can tear (Figure 1.7).

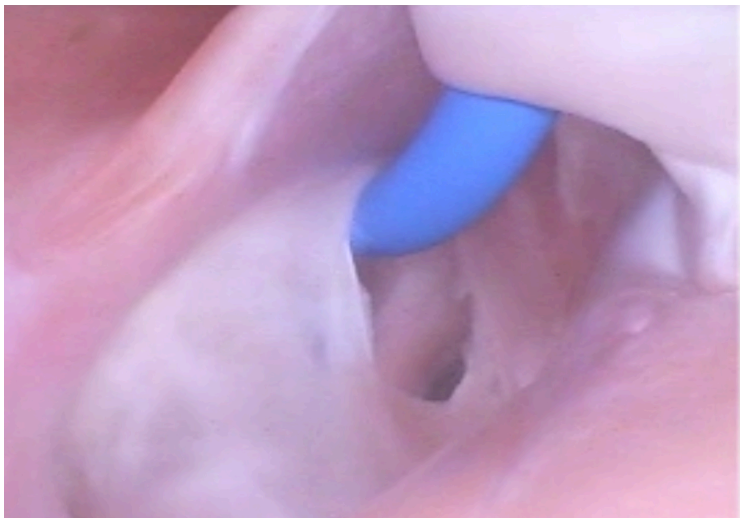

Figure 1.7: Example of potential complication as a result of catheter navigation performed in a swine showing FO tearing due to excessive deflection force from a delivery sheath attempting to navigate into a PV.

This step in the procedure prompts additional consideration of the use of the transseptal needle in the LA. The transseptal needle extends beyond the tip of the dilator. The amount of extension is dictated by the interference fit of the diameter on the needle shaft to the internal diameter reducer in the dilator tip. Given the large amount of needle extension and the relative thickness of the FO, future device designs must improve the needle tip to reduce the risk of cardiac tamponade, while still preserving the ability to achieve successful punctures. Clearly, anatomic variations can have an impact on the ability to conduct transseptal punctures and on possible complications.

Such variability in anatomic structures—combined with current device limitations in sheath size and in needle, length, and deflection capabilities—require continued advancements in order to decrease the risk to patients. Device developers must continue to collaborate with electrophysiologists. A partnership between engineers and health care providers is critical for improving patient outcomes.

Coronary Sinus

Arrhythmia ablation procedures commonly involve the CS. [32] Its ostium is located on the opposing side of the ER. In addition, the thebesian valve is located at the CS ostium (Figure 1.8). Inferior to the CS ostium, anatomic structures can be of various shapes and sizes. [33]

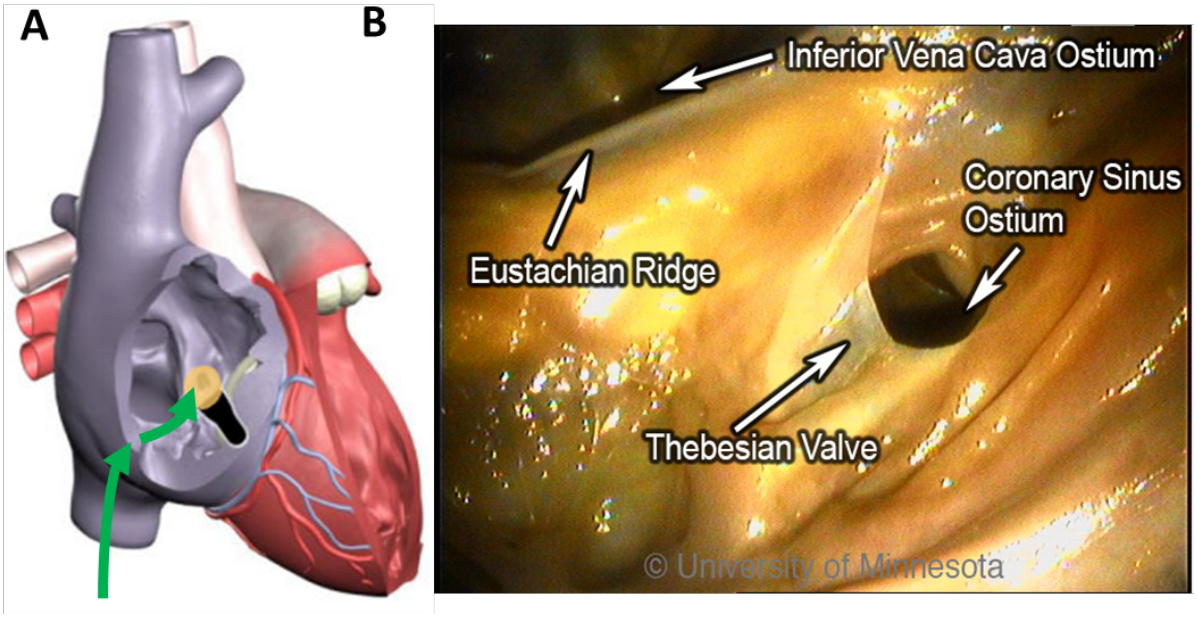

Figure 1.8: In the diagram on the left (A), the green arrows depict the device approach originating from the IVC into the CS ostium. The image on the right (B) shows the regional anatomy in the area of the CS bordered by the thebesian valve, including the IVC catheter introduction point. CS – coronary sinus, IVC - inferior vena cava.

Clearly, anatomic factors can increase the complexity of device delivery. The CS ostium resides in a deep pocket that is bordered by the ER, making catheter tip placement challenging. The location of the CS ostium relative to the IVC, along with the size of the ostium, can also present challenges.

To enter the CS, devices must have a high degree of deflection; furthermore, the region of deflection must have a small radius. With devices whose deflection is located more proximally in a stiff shaft and whose diameter is 8-French or larger, it will be more difficult to orient the tip so that it aligns with the CS ostium (Figure 1.9).

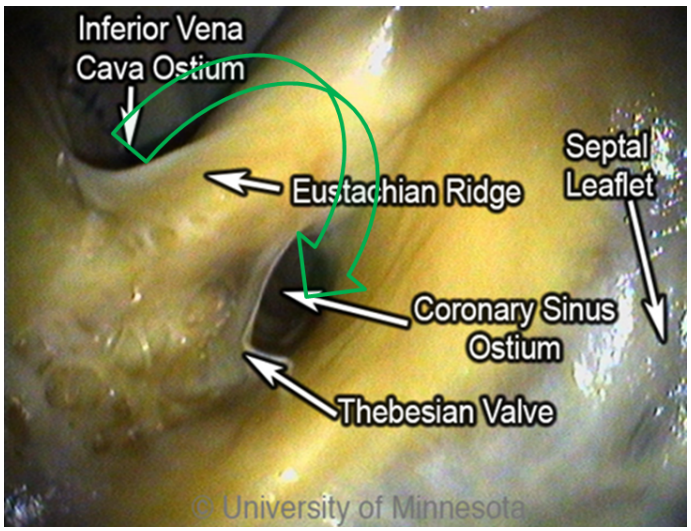

Figure 1.9: In this image, the green arrow depicts the device approach originating from the IVC. IVC = inferior vena cava

Further design work is needed to develop devices that can deflect in a small radius, allowing the catheter tip to be oriented in such a way that it can align with the CS ostium.

Right Atrial Appendage

RA ablation is required in instances of AF in which the cycle length recorded in the RAA is shorter than is the cycle length recorded in the left atrial appendage (LAA). The RAA location near the ostium of the IVC prompts the need to deflect devices (Figure 1.10A). The appendage can be a large structure; it is composed of very thin tissue as well as pectinated muscle and a sagittal band (Figures 1.10B and 1.10C).

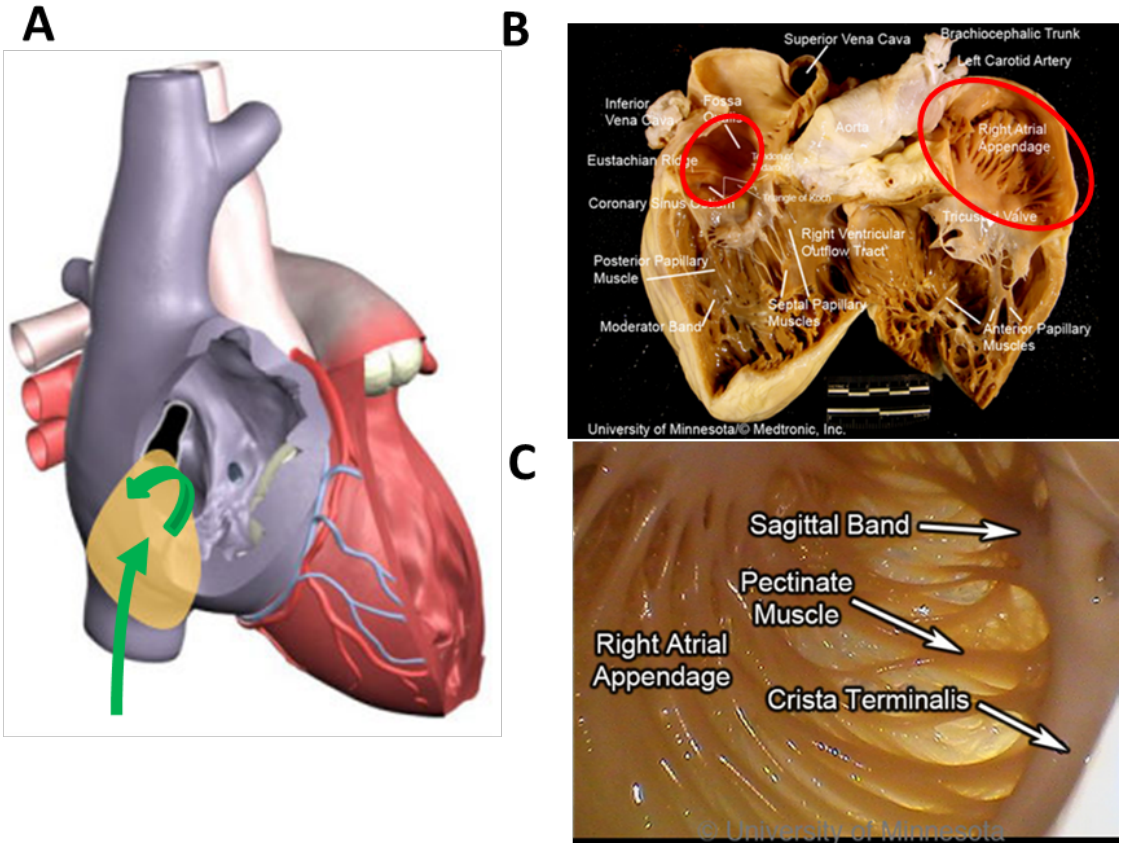

Figure 1.10: The diagram on the left (A) shows the approach to the RAA through the IVC. The image on the top right (B) shows the large size of the RAA and pectinated muscles. The image on the bottom right (C) shows the pectinated muscles and thin tissue.

Given the thin tissue of these anatomic structures, devices need to have very smooth tips that do not focus force into a point. With devices that have a rigid shaft, the risk of perforating the RAA is greater, because of the higher transfer of force. In contrast, with devices that have a compliant tip at the distal end, the tip can bend, thereby lessening the chance of perforating the RAA.

Ablating left atrial structures: PV, MI, and LAA Roofline

The LA has a venous component, along with a vestibule and an appendage. The

additional 4 venous orifices serve as corners to the atrium. The vestibule surrounds the mitral ostium. The LAA is typically a small extension that originates adjacent to the mitral valve annulus and the left PVs.

In the atrial areas, the anterior wall behind the aorta is commonly thin and can be torn during transseptal punctures. [35] The thicker parts of the LA are on the superior wall.[36] The ostium of the right PVs are adjacent to the plane of the atrial septum. The tissue that makes this transition is smooth. The target of PV isolation is a muscular sleeve that extends into each vein and ends inside the sleeve. The role of the sleeve has been reviewed in other studies. [37, 38] The organization of electrical activity from the PV is well known. [39, 40]

The smooth wall of the LA facilitates a uniform drag of the catheter tip against the tissue. The size of the LA is conducive to catheter tip placement against the tissue surface. But the formation of a small gap is possible; complex cardiac navigation systems do provide some guidance as to gap location, yet it might not be sufficient.

LA ablation can occur in a number of different locations and can be prompted by continuous electrical activity, with a minimum duration of 100 ms [41] and either fractionated or fragmented electrical activity. [42]

Left atrial pulmonary veins

PV isolation is a key step in treating patients with all forms of AF. Of note, the muscle sleeves in the ostial opening of all 4 PVs emit ectopic beats. Electrical isolation of each vein is now the standard of care for treating AF, using either cryogenic or radiofrequency

ablation. [29, 30, 31] In electrical isolation procedures, both ablation and diagnostic devices are used around and inside the PVs. The types of devices include guidewires, balloons, diagnostic catheters, and focal ablation catheters.

The ostia of the right PVs are adjacent to the FO. The ostial opening of the PV is a smooth surface. The close proximity of the PV ostia to the FO, and the sharp angle between them make it hard to orient a catheter through the puncture site and into the PV (Figure 1.11).

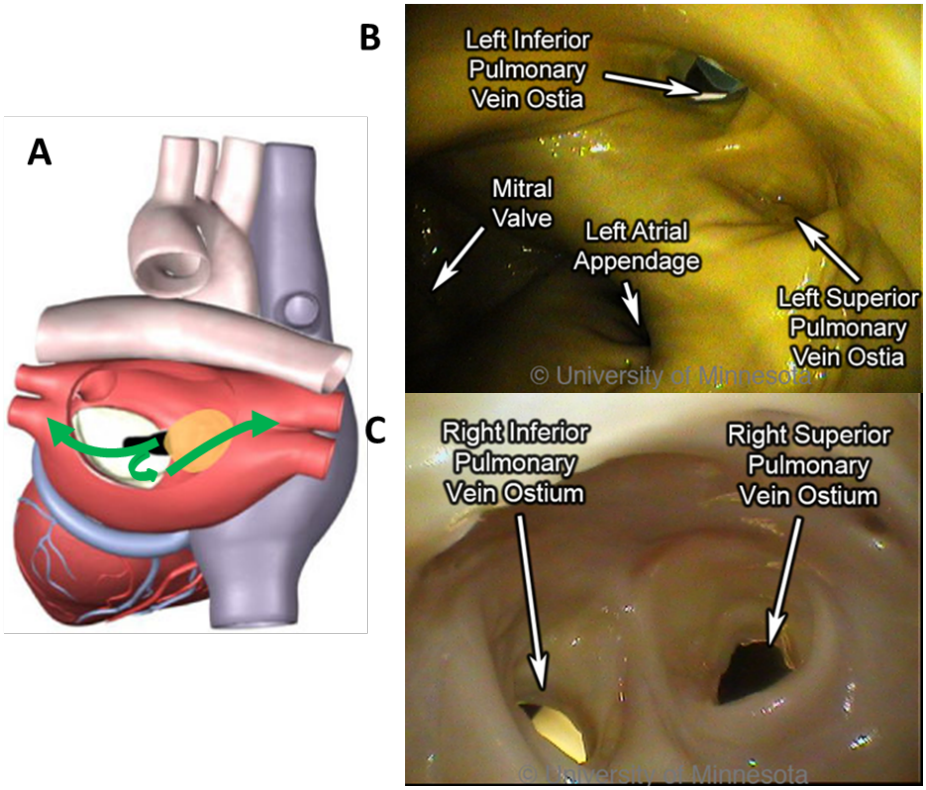

Figure 1.11: In the diagram on the left (A), the green arrows depict the directions of device introduction originating from the FO into the LA pulmonary anatomy. The image on the top right (B) shows the left PV ostium. The image on the bottom right (C) shows the right PV ostium. FO – fossa ovalis, LA – left atrium, PV pulmonary vein

The ostia can comprise ridges and are adjacent to each other on opposing sides of the atrium. The shape and orientation of the PV can vary; other anatomic structures can be atypical. Variations can include differences in ostial size and the existence of a common shared ostium. All of these factors can affect the effectiveness of the devices used to electrically isolate the tissue.

The PVs interface with guidewires, sheaths, balloons, and focal ablation catheters. The location of the transseptal puncture can have a dramatic effect on the ability to place the catheter tip in the ostium of the PV, especially because the distance from the FO to the ostium is short. In addition, the orientation of the opening of the PV is directed in a way that can result in the need to twist the guidewire to allow it to migrate inside the PV (Figure 1.12A). This anatomic orientation of the FO and the PV illustrates the importance of a sheath that has a small radius of deflection at the tip in order to facilitate guidewire insertion.

Catheter placement into the PV is also affected by the contour of the catheter tip. The angle of the catheter's approach might require anatomic guidance to properly position the tip (Figure 1.12B). This device-tissue interface shows the importance of a smooth, contoured tip.

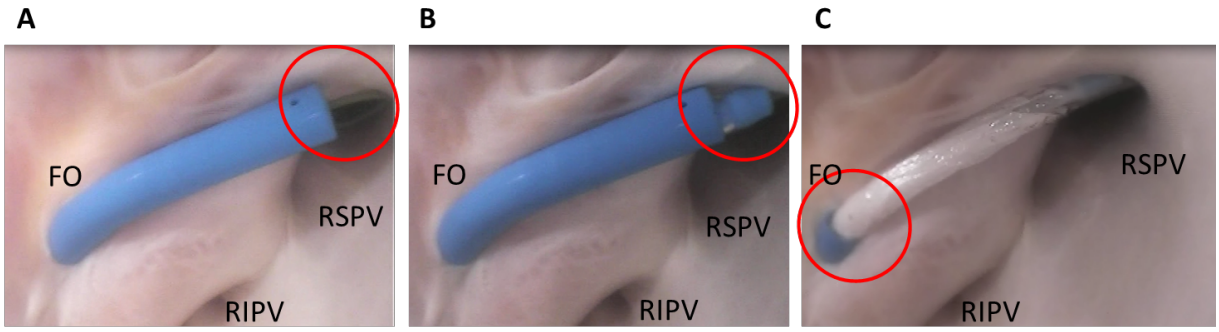

Figure 1.12: The image on the left (A) shows the catheter sheath and the use of a guidewire for placement into the RSPV. The image in the center (B) shows the introduction of the catheter tip at the PV ostium. The image on the right (C) shows the retraction of the catheter sheath to the FO and the introduction of a balloon catheter.FO – fossa ovalis, RSPV – right superior pulmonary vein, PV – pulmonary vein

The complete insertion of the ablation catheter is affected by its size and by the size of the atrium. The proximity of the FO to the PV can limit the ability to have both the sheath and the catheter in the chamber (Figure 1.12C). Limiting the distance of the therapeutic region of the catheter would provide greater latitude for use of the entire system in the atrium. Operation of these devices on the right side of the atrium is one of the more challenging steps of the procedure.

Performing the same steps on the left side of the atrium requires different device performance. The orientation of the FO to the left PV ostia (as compared with the right side of the atrium) is more conducive to device delivery. Guidewire introduction is typically facilitated by the nearly linear orientation of the FO to the PV ostium (Figure 1.13A), which allows the guidewire to be placed and lodged in the PV (Figure 1.13B).

The alignment of the FO and left PVs allows for easy catheter introduction into the LA and sufficient room to operate the device, thereby reducing the stress on the FO and

lessening the demands on the sheath (Figure 1.13C). For balloon-based devices, which require more area to operate than do focal ablation catheters, the alignment of the FO and left PVs is of particular importance.

Figure 1.13: The image on the left (A) shows the catheter sheath and the use of a guidewire for placement into the LSPV. The image in the center (B) shows the placement of the guidewire into the PV ostium. The image on the right (C) shows the introduction of the balloon catheter across the LA. LA – left atrium, LSPV – left superior pulmonary vein, PV – pulmonary vein

Once the catheter is delivered into the PVs, therapy delivery remains challenging. For example, balloon-based therapeutic devices are larger, with only a limited amount of deflection ability, so they require more room to operate. Given the orientation of the transseptal puncture to the ostium of the PV, the balloon is able to fully occlude the vein. However, uniform cooling may not be achieved, because the balloon's orientation is limited by the FO's orientation to the PV's muscular sleeve (Figure 1.14).

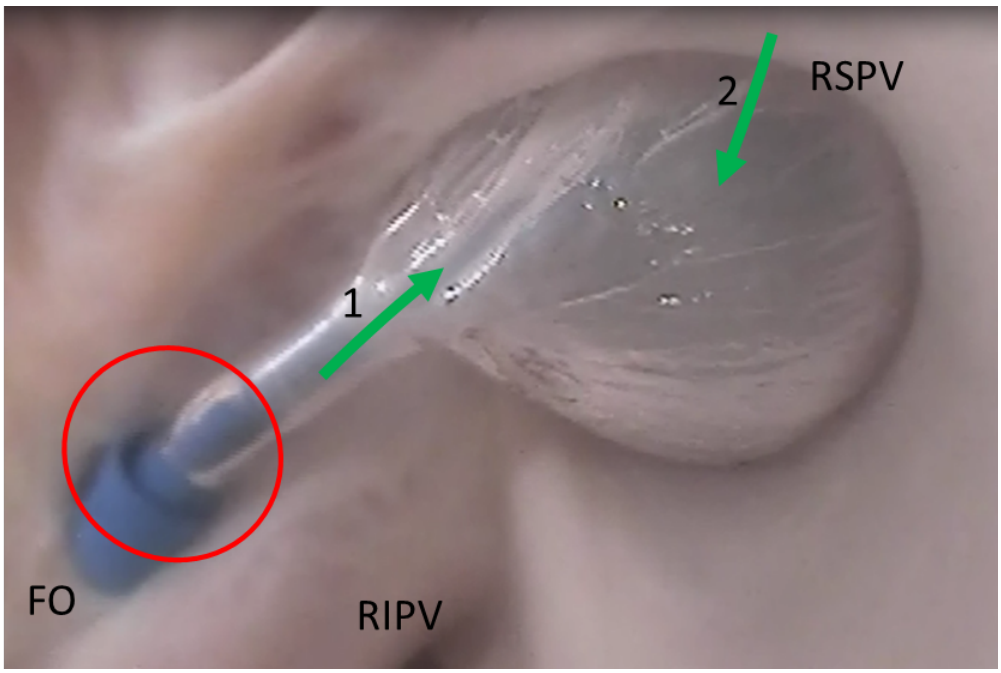

Figure 1.14: In this image of a balloon-based LA RSPV occlusion, the sheath is retracted to accommodate the ablation catheter (red circle). The catheter orientation (green arrow 1) is not aligned with the PV ostium orientation (green arrow 2). LA – left atrium, PV – pulmonary vein , RSPV – right superior pulmonary vein

These anatomic challenges accentuate the importance of having an acute distal deflection segment on the ablation device—in order to improve catheter tip orientation to, and alignment with, the PV ostium. Such challenges also jeopardize the ability of the sheath to maintain its placement in the LA. Decreasing the length of the distance between the distal tip of the sheath and the proximal end of the balloon would allow more sheath to be retained in the LA. The sheath must have a very distal deflection control with an acute radius of deflection. The smooth wall of the atrium facilitates placement of the ablation catheter.

If additional lesions are necessary beyond PV isolation, they can be created in the LA in the form of a linear lesion along the roofline or a mitral isthmus lesion, or via ablation of the LAA.

Left atrial appendage

Many times, the LAA is a site for the deposition of thrombus. A stroke is a possibility if the thrombus is able to dislodge and travel to a part of the vasculature that supplies blood to the brain. The LAA is oriented on the opposing side of the LA from the FO, making device delivery less challenging (Figure 1.15A).

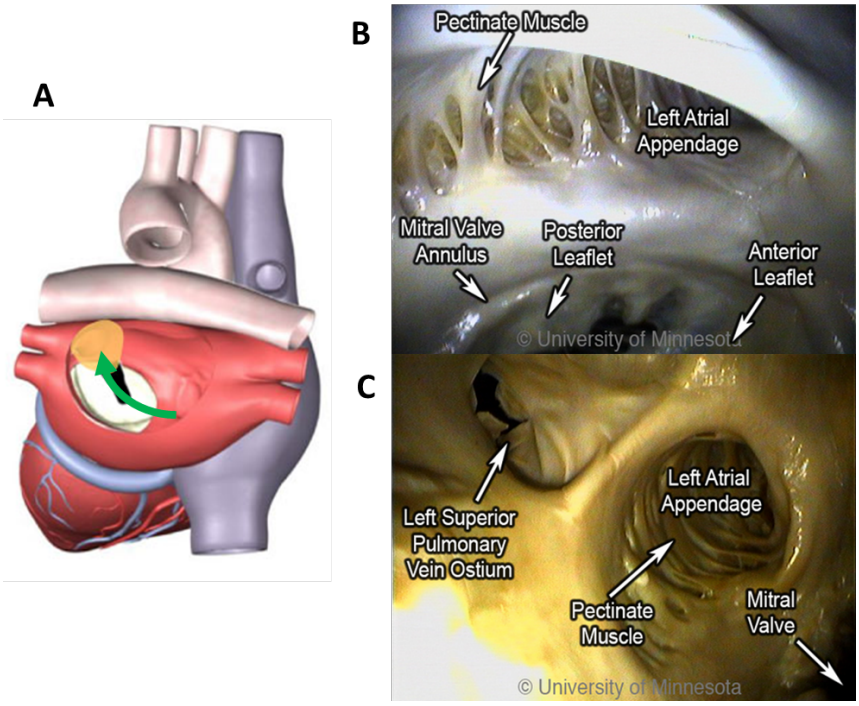

Figure 1.15: In the diagram on the left (A), the green arrow indicates the approach to the LAA from the FO. The image on the top right (B) shows the position of the LAA relative to the MVA and the presence of pectinated muscle. The image on the bottom right (C) shows the position of the LAA relative to both the MV and the LSPV.FO – fossa ovalis, LAA – left atrial appendage, LSPV – left superior pulmonary vein, MV – mitral valve

For achieving and retaining device placement, the opening of the LAA can be challenging. The ability to place a focal ablation device at the ostial opening is complicated by the presence of prominent ridges in the ostial area of the LAA. Focal devices for performing point-by-point ablation around the opening are difficult to operate. Alternatively, devices that encircle the LAA, or that occlude it, preclude the need to create point-by-point lesions and remove the complexity of attempting to place a catheter tip on a ridge structure.

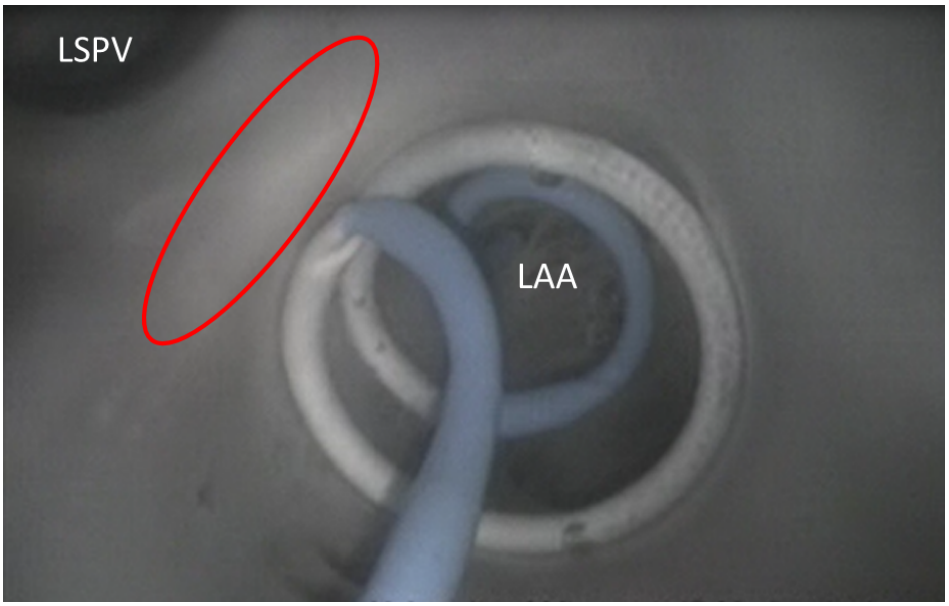

Figure 1.16: This image shows the catheter shaft circulating around the LAA ostium; the red circle depicts the ridge between the LAA and LSPV. LAA – left atrial appendage, LSPV – left superior pulmonary vein

Devices that deploy into the LAA and then place the therapeutic region at the opening are able to encircle the opening (Figure 1.16). Focal ablation devices need the ability to apply sufficient force on the tissue for lesion generation, without slipping into the pectinated muscles of the LAA interior.

Dynamically shaped ablation devices that could occlude the LAA would have an advantage: they might be able to maintain position and sufficient force for lesion generation.

Mitral isthmus and roofline ablation

The mitral isthmus (MI) is a region of tissue that borders the annulus of the mitral valve and borders the LAA, and then rises over the ridge toward the left PV (Figure 1.17A). This is a common area to create a contiguous lesion in, which helps terminate conduction patterns in patients with AF in whom PV isolation is not sufficient. [32, 33, 34]

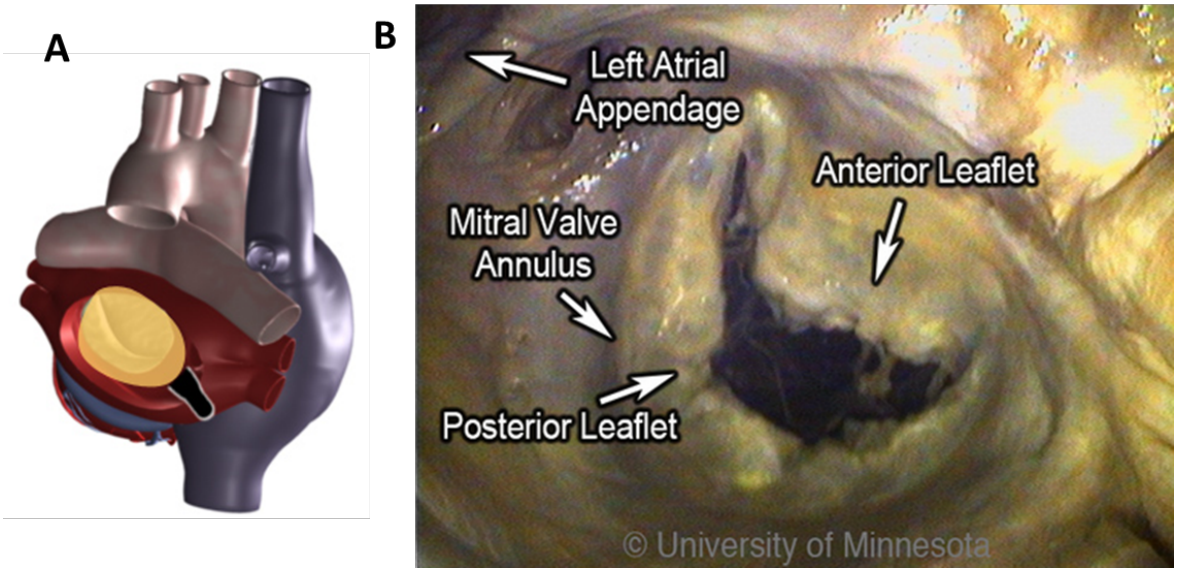

Figure 1.17: The diagram on the left (A) shows the MV in the LA. The image (B) notes various structures, including the MVA, which serves as the starting point for creating a linear lesion in the MI. LA – left atrium, MV – mitral valve, MVA - mitral valve annulus.

The creation of the MI or roofline linear lesion is affected by even a minor amount of anatomic movement of the MI with each contraction, making catheter tip placement on

the ridge difficult. Any anatomic movement changes the force on the catheter tip and can contribute, at times, to a temporary loss of sufficient contact for lesion creation. The ability to maintain tissue contact is a byproduct of the amount of force on the catheter tip. For MI linear lesion creation, given the orientation of the FO in relation to the MVA, the catheter tip must be able to reach to the MVA, and the deflection must be able to place force on the catheter tip (Figure 17B).The presence of a ridge is an additional complicating factor: the shape of the ridge can be pointed, making it difficult for the catheter to be placed on it.

To ensure necessary contact when creating a linear lesion, a focal catheter may be used against a supporting structure, such as another catheter (Figure 18A) or the wall of the atrium (Figure 1.18B).

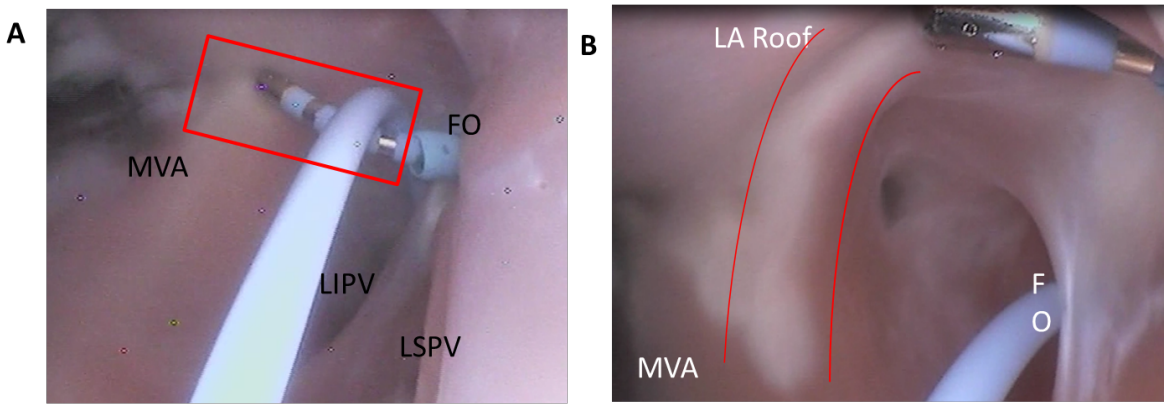

Figure 1.18: The image on the left (A) shows MI lesion creation originating at the MVA. The image on the right (B) shows creation of a roofline linear lesion. MI – mitral isthmus, MVA – mitral valve annulus

A focal ablation catheter has the advantage of adaptability. This device design could be extended to include repositioning of electrodes, softening of the tip, and better deflection

capabilities all of which could widen application across an array of atrial anatomies, resulting in an improvement in energy delivery.

Conclusion

Understanding how ablation devices interface with tissue and anatomic structures can make a crucial difference in their therapeutic application. Anatomic structures vary from person to person. Within each person, the endocardial surface changes shape with each heartbeat and can prompt catheter migration, making it difficult to know exactly where the device was placed and what is happening at the device-tissue interface. By using Visible Heart® methods to directly visualize the device-tissue interface in fresh reanimated human hearts, we assembled and analyzed an array of illuminating images, providing a critical aid to clinicians and medical device designers alike.

The tools that have traditionally been used to treat patients with AF have numerous limitations, all of which lengthen ablation procedure time and increase the likelihood of disease recurrence. Future research in this field needs to focus on reducing the risks of transseptal procedures, increasing catheter mobility, enhancing the anatomic precision of catheter tip placement, , and improving imaging capabilities. Studies must investigate methods for improving transseptal punctures, reaching targeted anatomies with therapeutic devices, and assessing the effectiveness and quality of lesions at the point of their creation.

2. Mechanical properties of the fossa ovalis tissue during transseptal punctures

Stephen A. Howard, PhD [4], Stephen G. Quallich, BS [1,2], Mark A. Benscoter, MS [1,3],

Bryce Cole Holmgren, BS [1,2], Christopher D. Rolfes, PhD [1,2], Paul A. Iaizzo, PhD [1,2]

[1] Department of Biomedical Engineering, University of Minnesota (Minneapolis, MN)
[2] Department of Surgery, University of Minnesota (Minneapolis, MN)
[3] Department of Engineering, Mayo Clinic, (Rochester, MN)
[4] Medtronic, Inc. (Moundsview, MN)

Address for Correspondence:
Paul A. Iaizzo, PhD
University of Minnesota
420 Delaware St. SE
B172 Mayo, MMC 195
Minneapolis, MN 55455 USA
T: 612-624-7912; F: 612-624-2002; Email: iaizz001@umn.edu

Preface:

This study was motivated by the first chapter, in which we observed the transseptal puncture under direct visualization. As commented, the methods lacked the ability to quantify the amount of force required to perform the transseptal puncture. The ability to correlate the performance of medical devices in performing the transseptal puncture between animal to human has been missing as a predictive indicator of human device performance. This study devised a set of methods to quantify the transseptal puncture procedure using clinical devices and then derived a correlation between swine and human. This enables the ability to understand the translation between models and to offer predictions of anticipated performance in a human. The material in this chapter has been published in the Journal of Interventional Cardiology – a peer reviewed journal.

For this study, I was responsible for study design, data analysis, manuscript editing. Stephen Howard contributed to study design, method creation, data collection, data analysis, and manuscript creation. Stephen Quallich also contributed to method development, data collection, data analysis, and manuscript editing. Paul Iaizzo provided editing.

Summary

Background:

Transseptal puncture is a common procedure that gains access to the left atrium, allowing percutaneous mitral valve repair, left atrial appendage closure, and left-sided ablations. The basic approach has not changed in many years, however the frequency of transseptal punctures and the size of devices are increasing with emerging treatments. This study examined the mechanical response of the fossa ovalis as a result from different transseptal device sizes in both swine and human.

Methods and Results:

A broad size range of transseptal devices (4F-18F) were advanced through atrial septa of swine hearts; some devices were inserted in both swine and human hearts using 10F catheters. Greater forces were required to puncture through the septa of human hearts compared to those of swine. Larger catheters used in swine hearts required greater force to advance them through the septa, causing greater dilation of tissue and sometimes tearing the floor of the fossa ovalis; analyses indicated an exponential increase in size of the iatrogenic atrial septal defect. Specific tissue property testing of the septum primum showed that this tissue sheared at a lower exerted force in a superior to inferior direction.

Conclusions:

The results of this study mean that this data can be used in the creation of a swine based model that could be used as a predictive indictor of the human response. In addition, the greater forces required to conduct the transseptal warrant additional work to study if these increased forces place additional risk of anatomical damage related to possible

perforation of the atrial wall. Finally, these results mean that an increased size in the atrial septal defect will require additional study to understand the long term impact on tissue healing at the puncture location.

Introduction

Transseptal punctures (TSP) have been performed since the 1960s for a variety of clinical procedures[43]. The avascular fossa ovalis (FO) in the atrial septum provides a location, as this tissue is thin allowing for deformation (tenting) of the tissue that is visible on fluoroscopy to ensure appropriate anatomical location prior to performing the puncture to the left atrium. It should be noted that other routes (e.g., through the arterial vasculature or transmyocardially) may elicit associated complications or be more difficult relative to a transseptal approach[44]. To perform a TSP, access to the right atrium is obtained through the venous system, then transseptal sheaths are advanced through the vasculature and into the right atrium. The placement of the sheath onto the FO is identified by watching for a characteristic "jump" of the dilator tip following retraction and dragging of the transseptal equipment inferiorly. After the FO has been located, the tenting can be generally visualized through fluoroscopy and, more commonly, echocardiography[45, 46]. A physician will tend to look for the most optimal portion of the septum to puncture based on the type of left atrial procedure that needs to be conducted. Additionally in some patients, more than one puncture may be conducted to simultaneously advance different types of catheters into the left atrium. Nevertheless, the optimal placement of the puncture location is very important, as it will commonly affect the ultimate success or ease of a given clinical procedure[47].

The complication rates associated with transseptal punctures are cited to be as low as 0.74% of procedures intraoperatively[48]. Yet, the post-operative outcomes are considered

separately and incidences of remnant interatrial shunts have been reported. For example, McGinty et al. presented a review indicating prevalence of iatrogenic atrial septal defects (IASDs) to be as high as 87% post procedure and, at an 18-month follow-up, incidences were reported as high as 15%[49]. Although the authors suggest that most of these created holes were resolved over time and the IASDs were not associated with clinical issues such as embolism, cyanosis, or right heart failure, they could still present issues especially if one assesses potential new procedures involving TSPs with larger sheaths[49].

As mentioned above, there are a number of procedures that require a TSP including left-sided cardiac ablations, percutaneous mitral valve repairs, mitral balloon valvulotomies, left atrial appendage closures, and certain ventricular assist device placements[44, 50-59]. These procedures along with some newer and future procedures, including left ventricular endocardial pacing and percutaneous mitral and aortic valve implantation, could potentially bring about a greater prevalence of TSPs and thus higher incidences of potential complications[60-62]. As cardiology procedures have progressed, the range of sizes for transseptal devices has increased. To date, the smallest transseptal devices typically are 4F and range up to the largest reported of 22F[49, 61]. This latter size range has prompted discussions regarding what the FO is capable of tolerating, a topic addressed in previous publications[49, 53, 55, 63]. Yet, we consider here that a detailed study investigating the elastic tissue properties of the FO and the impact of the various sized catheters on IASD formation is necessary to help understand clinical limits.

In addition to the puncture that is created in the FO, manipulation of catheters and tools

across the septum may result in the tissues being stretched and/or torn, resulting in larger IASDs. A previous study relative to this topic was performed by Saitoh et al. with a mitral valve clip procedure under echocardiography[51]. The subsequent holes created and identified were elongated and elliptical (not circular), suggesting that the simple puncture forces were not the only strains being placed on the septum, but rather some radial/shear forces applied by the catheter could potentially cause tears in an axial direction. Since the utilization of swine hearts as a model for TSP studies has been reported previously, we also believe it provides a good anatomical basis for our study. Yet, by additionally utilizing both ex vivo swine and human hearts for a subset of our experiments, multiple variables could be studied and a relation to human cardiac anatomy can be specifically assessed[64-66].

Finally, the biomechanical characterization of the heart, as a whole, is currently underway by numerous laboratories. For instance, interest in tissue engineered heart valves has led to the study of valves to better mimic their behavior[67, 68]. However, studies assessing the tissue properties of the FO and methods to reduce damage during such procedures, to the best of our knowledge, are nonexistent. Such information would be quite useful for improving the understanding of the shear/tear forces and biomechanical properties to attain a complete view of IASD creation. As technology continues to advance, the role of computational modeling in device development and personalized medicine will likely become readily available and important, and the data we describe here will be critical inputs for this development[69].

Methods

Obtaining tissue and preparation

Swine hearts (n=48) were obtained fresh and were transported on ice and then dissected within 8 hrs post excision. The right and left atria were opened to expose the interatrial septum while keeping intact the tissue surrounding and supporting the FO. The isolated cardiac tissues were warmed to 37°C using a circulating water bath. Images of the FO were taken pre- and post- puncture.

Human hearts were received as a donation for research to the University of Minnesota from organ donors whose hearts were deemed not viable for transplantation (via Lifesource, St. Paul, MN, USA). Table 2.1 provides brief medical histories of the donors including these cardiac conditions: one with atrial fibrillation, one with hypertension, and one with an unspecified "heart problem."

Table 2.1. Baseline characteristics of human hearts (n=7)

Demographic	Measurement
Male (%)	57.1
Age (years)	58.4±5.7
Weight (kg)	86.0±30
Height (cm)	168.7±7.7
Heart Weight (g)	428±130

Fossa size:	
Superior/inferior (mm)	20.8±6.2
Anterior/posterior (mm)	15.7±6.2
Thickness (mm)	0.68±0.27

Exclusion criteria for testing included lack of an intact atrial septum and other congenital abnormalities that would disallow the suction device to be implemented. These hearts were warmed with 37°C saline.

Catheter and fossa holder method

A suction device on a positionable arm provided circumferential adhesion surrounding the FO to hold the interatrial septum in a secure manor (Fig. 2.1).

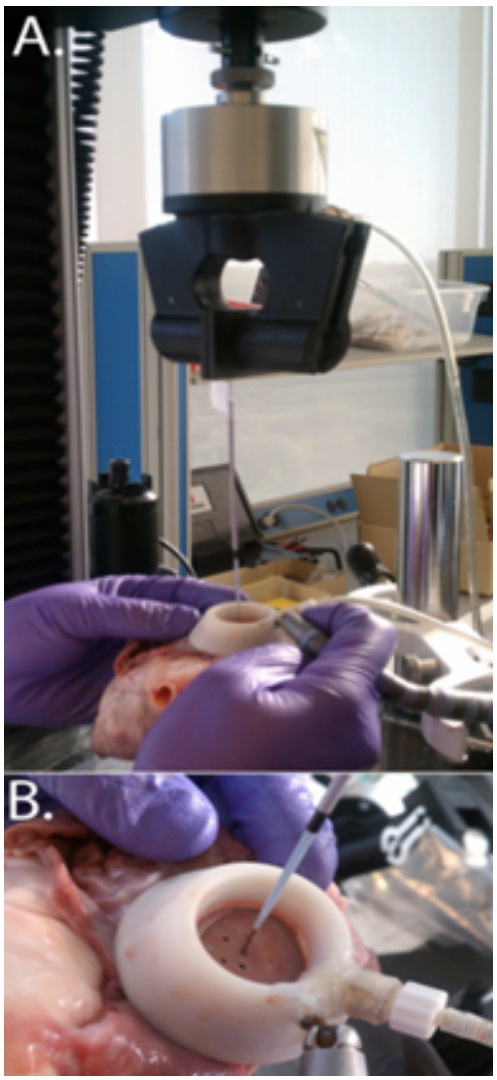

Figure 2.1: Radial adhering suction device for stabilization of the atrial septum for tissue puncturing. (A) Force testing machine with transseptal device attached and puncturing the atrial septum. (B) Close-up view of the atrial septum and stabilization device employed for puncturing.

The devices used in these experiments were composed of a dilator and sheath, and had internal diameters of 4, 8, 10, 12, 16 and 18 French, according to manufactures' specifications. Only the 4F, 8F, 10F and 12F devices were indicated for transseptal applications, while the remaining two devices had specified alternative uses; their

employment in these investigations allowed for testing of larger diameter sheaths. The specific measurements of the outer diameter as they relate to the catheter size are listed in Table 2.2.

Table 2.2. Size and dimensions of catheters

Manufacture Labeled Catheter Size	Dilator OD (mm)	Sheath OD (mm)
4F	1.8	2.2
8F	3.2	3.8
10F	3.6	4.1
12F	3.9	4.8
16F	5.3	6.5
18F	6.0	7.2

*OD=outer diameter

Catheters were trimmed to a length of 15cm and, if curved, they were straightened to keep the structural integrity yet provide a linear direction of force normal to the FO. The dilator and sheath were bonded together with ultraviolet cure adhesive (Loctite, Henkel, Düsseldorf, Germany) at the cut end of the catheter. The internal lumen of the dilator remained unobstructed to allow for a Brockenbrough® (BRK, Medtronic, Inc., Fridley,

MN, USA) transseptal needle, cut 18cm from the tip and straightened to protrude from the dilator tip, as it would in clinical practice. Alternative designs were used for the 4F, 16F and 18F devices, since they would not allow for proper protrusion of the needle tip beyond the dilator tip. The end of a Brockenbrough needle was separated from the main shaft and adhered into the tips of each of the dilators of those catheters with a stiff metal rod through the dilator to provide mechanical support for the needle tip (Fig. 2.2).

Figure 2.2: Schematic of transseptal devices used for testing. The dilator was seated into the sheath and attached at the proximal end via adhesive. The center lumen was kept clear for a needle to be placed through it and protrude from the distal tip.

The catheters were either clamped or inserted into a connector attached to a load cell for obtaining puncture forces.

Tenting and puncture testing

A circumferential suction device was attached to the atrial septa of either swine or human hearts (Fig. 2.1) to allow for continuous and repeatable fixation of the FO, as noted above. The device was locked into place with the FO in the center of the suction ring, and the FO was placed perpendicular to the trajectory of the transseptal catheter.

The forces required to puncture and tent the FO at various locations were obtained by

using mechanical force testing systems (Instron, Norwood, MA, USA; Chatillon TCD225, Largo, FL, USA). The relative locations of tenting and punctures were defined in relation to the superior, inferior, anterior, and posterior orientations (Fig. 2.3).

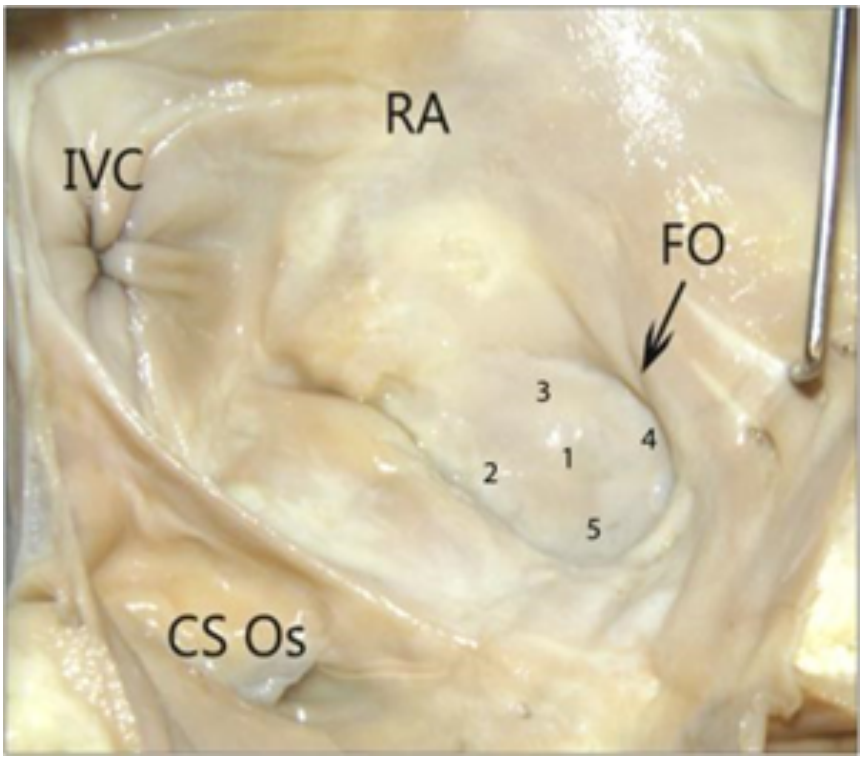

Figure 2.3: Location of the fossa ovalis (FO) in relation to other anatomy within the right atrium (RA): the inferior vena cava (IVC), and the coronary sinus ostium (CS Os). The numbers indicate various puncture locations: (1) center, (2) inferior, (3) posterior, (4) superior, and (5) anterior.

The shortened catheters were affixed to the load cell so that their trajectory was normal to the floor of the FO. Following stabilization of the FO with the suction device, the catheters (without the needle protruding from the dilator) depressed the FO to a depth of 8mm for swine hearts and 12mm for human hearts at a rate of 254mm/min and then retracted to the starting position. The difference in the protocol between human and swine

experiments was related to the identified differences in the tissue compliance between the swine and human tissues based on pilot studies of the tissue (data not shown). The first tenting location was the center of the floor of the FO, followed by the inferior, posterior, superior, and anterior regions. Then the catheters were driven through the FO with a transseptal needle protruding from the dilator at a rate of 254mm/min at various locations on the FO, beginning with the center and followed by subsequent puncturing at alternate locations.

Initial analyses of the force versus distance relationships indicated that the largest forces required for transseptal puncture were when the tips of the needles, tips of the dilators, dilations of the septum, and tips of the sheaths were going through the septum (Fig. 2.4).

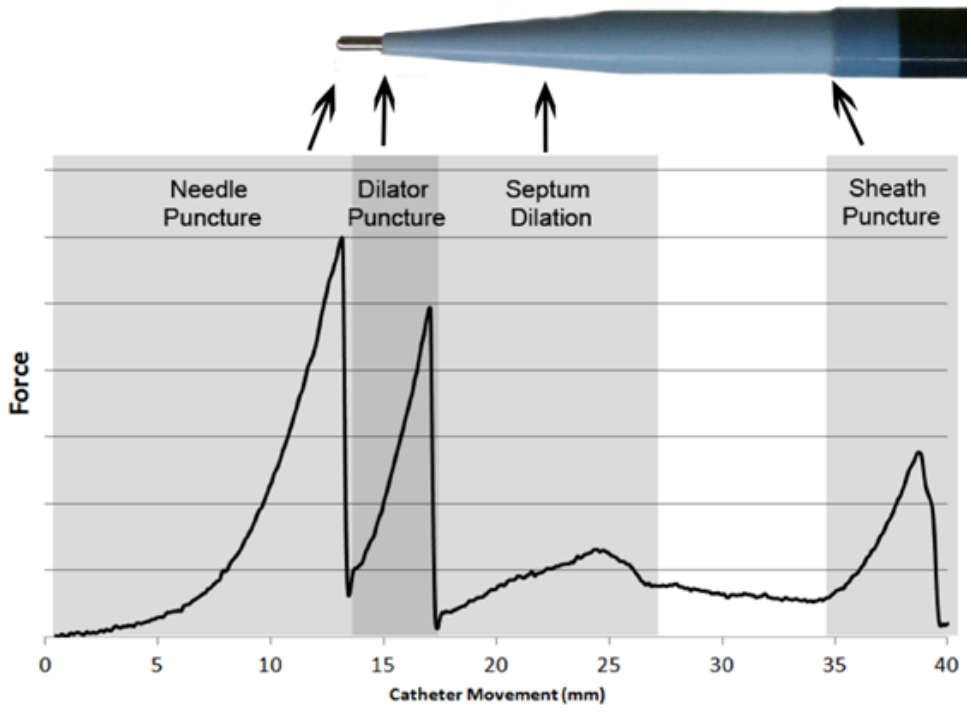

Figure 2.4: Characteristic force verses distance graph during fossa ovalis puncturing. Note the distinctive peaks during each transition of the dilator and sheath; upon reaching a new layer, the force increases due to the need for fossa ovalis expansions.

The forces and distances were recorded by the system for each of these events for the various puncture locations. Following the punctures, the remnant holes were measured.

Fossa shear force analyses

Additional swine hearts were obtained ranging from 400-650g in size (n=70). The atrial septum including approximately 5mm of tissue surrounding the floor of the FO was excised from each heart. Samples were randomized to size and direction groups, and the inferior or posterior portion of the musculature surrounding the FO floor was cut off (Fig. 2.5A). The FO was punctured with a transseptal Brockenbrough® needle and then a 4F, 12F, or 18F sheath was advanced through the septum. In all cases, the sheath and dilator were maintained in a perpendicular position relative to the floor of the FO via a custom fixture (Fig. 2.5B).

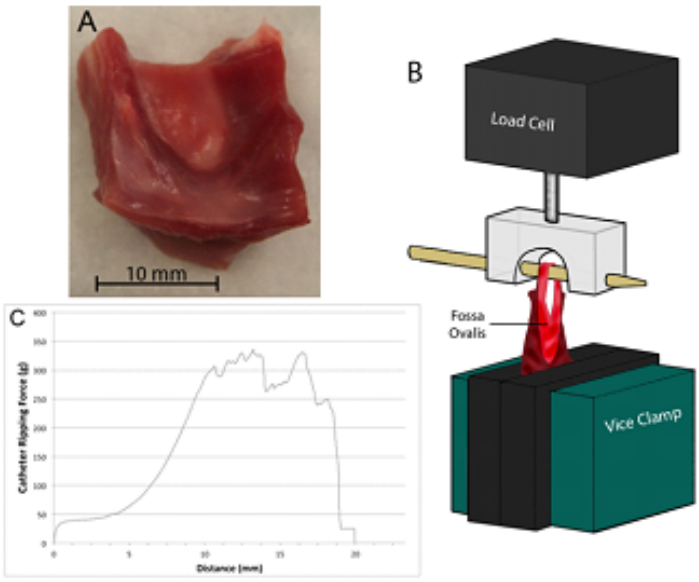

Figure 2.5: Schematic representation of the fossa ripping test setup. The muscular tissue adjacent to the septum primum (posterior rim of the fossa ovalis for posterior pulls and superior rim for inferior pulls) was cut off to allow the sheath to fully disengage from the atrial septum without consequence from the muscular portion of the atrium surrounding the floor of the fossa ovalis (A). The fossa ovalis was ripped by a catheter which was inserted through the floor of the fossa ovalis in the mechanical force tester (B). An example of the resultant force versus extension plot is shown in (C).

While the side of the FO opposite the cut side was anchored, the sheath was pulled away from the base at a rate of 100mm/min causing it to rip through the FO, employing a mechanical force tester (Chatillon). These atrial septa were ripped towards the cut section of the septum in either a superior or posterior direction. The average sheath ripping forces were defined as the average forces while the septum primum was ripping. To illustrate, Figure 5C shows that the 10-19mm extension portion for this sample was defined as the average ripping force, while the peak sheath ripping force was the highest force recorded. Fossa ovalis dimensions, average ripping force, and peak sheath ripping force were also

recorded.

Tensile testing

Swine atrial septa were harvested in the same way as described previously (n=16 animals; n=41 samples). The FO was dissected into several (1-5) strips along either the superior/inferior or anterior/posterior directions. These strips were cut in a dog-bone shape and 2-0 silk sutures were tied to both ends (Fig. 2.6) for mechanical testing; the samples were pulled at a rate of 100mm/min until failure with a mechanical force tester.

Figure 2.6: Example of prepared dog-bone shaped sample used for testing (A) and with 2-0 silk suture attached while mounted in the testing pull tester (B).

The dimensions of each sample were recorded along with the strain at failure and peak force; the Young's modulus was calculated.

Statistical analyses

All data are represented as the mean±SE unless otherwise noted. Student's T-tests were used for one-to-one comparison and ANOVA was employed for multi-group comparisons. Significance was determined with a p-value <0.05.

Results

Tenting studies

The initial tenting experiments showed that the average forces required to tent and extend the septum primum by 8mm were greater for the human hearts compared to swine (199±30gf vs. 135±5gf respectively, $p<0.001$). By breaking down the data to assess the relative effects of location on the tenting forces, only one statistically significant difference was identified in the inferior portion of the FO, where the human tenting was significantly higher (145g±65g, n=40, vs. 292g±213g, n=8; $p<0.01$). The remainder of the species comparisons for each location were not significantly different (Fig. 2.7).

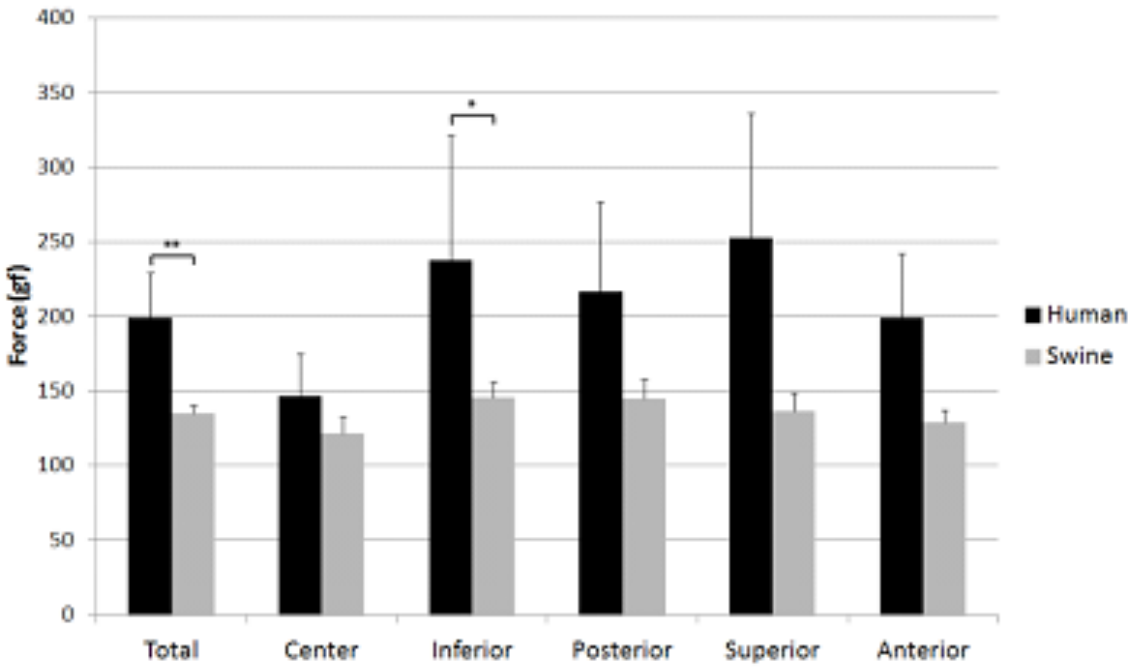

Figure 2.7: Forces required to tent the fossa ovalis by 8mm. Experiments were performed on excised human (n=8) and swine (n=40) hearts. (*=p<0.01, **=p<0.001)

Yet, if one combines all tenting data per species, the swine hearts were shown to require significantly less force to tent the fossa regardless of the location (swine 138±5g n=180 vs. human 199±30g, n=23, p<0.001). In general the lowest tenting forces were observed in the center of a given fossa, however the data were not significant (p>0.05).

Puncture forces: human vs. swine comparisons

Human heart specimens were punctured only with the 10F catheter for comparison to the swine hearts. These punctures produced characteristic force versus distance plots, where the forces for the needle, tips of the dilator, and the sheaths to pass across the septum were easily observable as transient peak forces (Fig. 2.4). The other force recorded of interest was the maximum force seen during the dilation phase of the septum (i.e., when

the tapered portion of the dilator passed through the FO).

When comparing the 10F catheter data between swine and human samples, the results showed a higher force required for each portion of the catheter (Fig. 2.8).

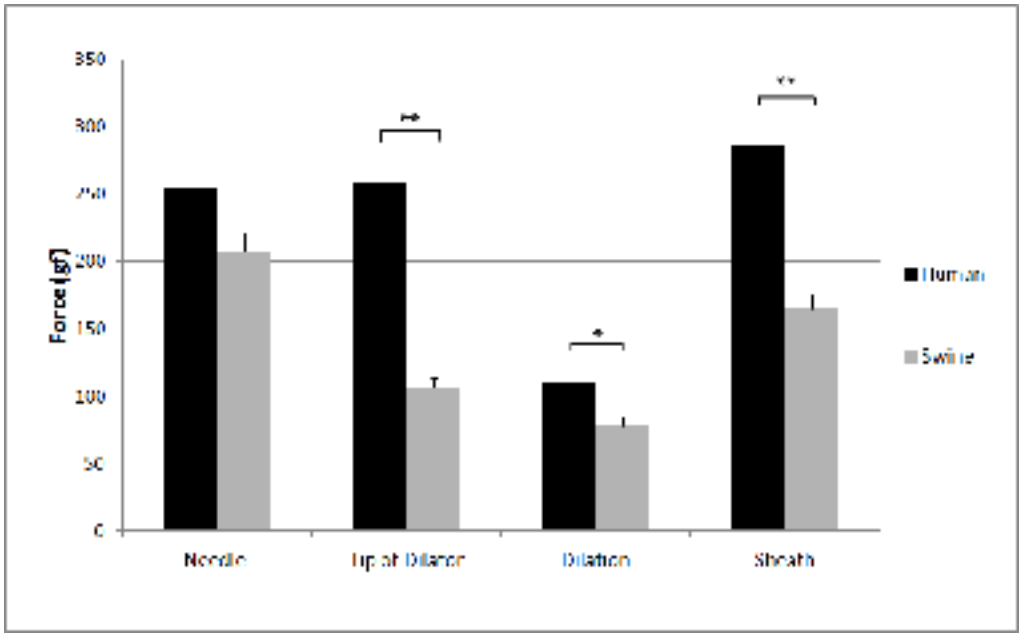

Figure 2.8: Average peak forces required to pass various portions of 10F sheath through the septum primum in isolated septa of human and swine hearts. Significant differences were found between these two species when comparing the tip of the dilator, dilation, and sheath forces (*=$p<0.01$, **=$p<0.001$)

The greatest difference between species was observed for the data between the peak forces of the tip of the dilator, requiring 240% greater forces for the human hearts. It should be noted that significant differences were found when comparing the average forces required to pass the various potions of the catheter through the septum for the tip of the dilator, dilation, and the sheath ($p<0.01$ for each; Fig. 2.8).

While assessing relative distributions of the peak protrusion forces for each portion of the TSP with a given catheter, we obtained a larger range of values for the human tissue studies compared to the swine tissues. The human data displayed a much larger distribution of force for the penetration of each portion of the assembly compared to swine data (Fig. 2.9).

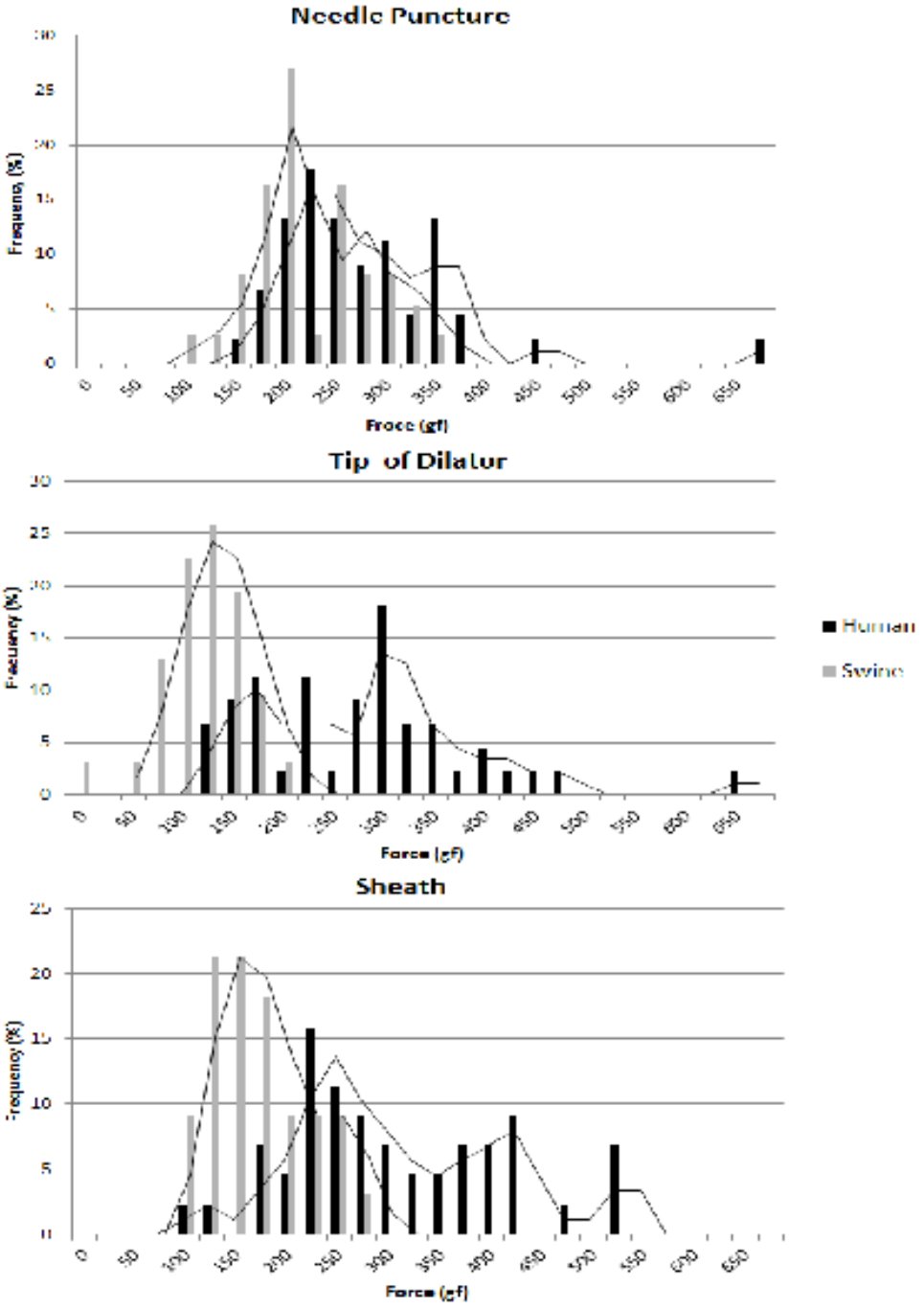

Figure 2.9*:* Histogram of recorded peak forces required to traverse the septum with various portions of a 10F sheath.

Although this trend was seen for the tip of the dilator and sheath, the range for the needle puncturing produced a plot with similar distributions for both the swine and human data.

Puncture forces: sheath size comparisons

The variability in the needle punctures alone resulted in an average puncture force of 201±75gf (±SD) with the 176 punctures that were performed with the Brockenbrough® needle. To account for these variations in tissue performance, the subsequent portions of the sheath were normalized to the needle puncture forces. This was done to help determine the relative relationship between sheath sizes and resultant forces required to traverse the atrial septum. Subsequently, it was found that there was a direct correlation between catheter size and the forces required to pass through the septum. On average, the needle punctures required greater forces than either the passing of the tip of the dilator or the forces of dilating the tissues. ANOVAs were performed for each of the sheath sections and we found significant differences within each group with p-values<0.001 (Fig. 2.10).

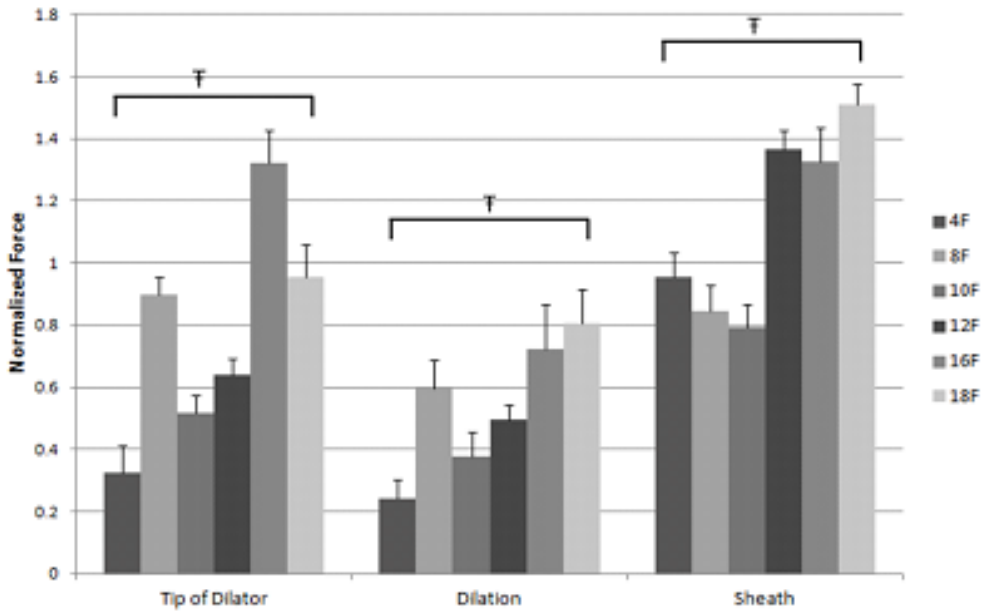

Figure 2.10*:* Relative forces required to traverse the atrial septum with various portions of a transseptal sheath of difference sizes. (Ŧ=$p<0.001$ based on ANOVA)

The other notable trend observed was that the dilation forces were significantly less for each of the sheath sizes compared to both the passing of the tips of the dilator and/or the shaft of each sheath ($p<0.02$ in all instances).

Following the punctures, images were taken of the resultant holes formed in the atrial septa. The minimum and maximum lengths were determined and plotted in relation to the outer diameter of the sheath. There was a positive correlation between the resultant hole sizes and the sheath sizes, as would be predicted. These data identified an exponential increase in resultant hole sizes (Fig. 2.11).

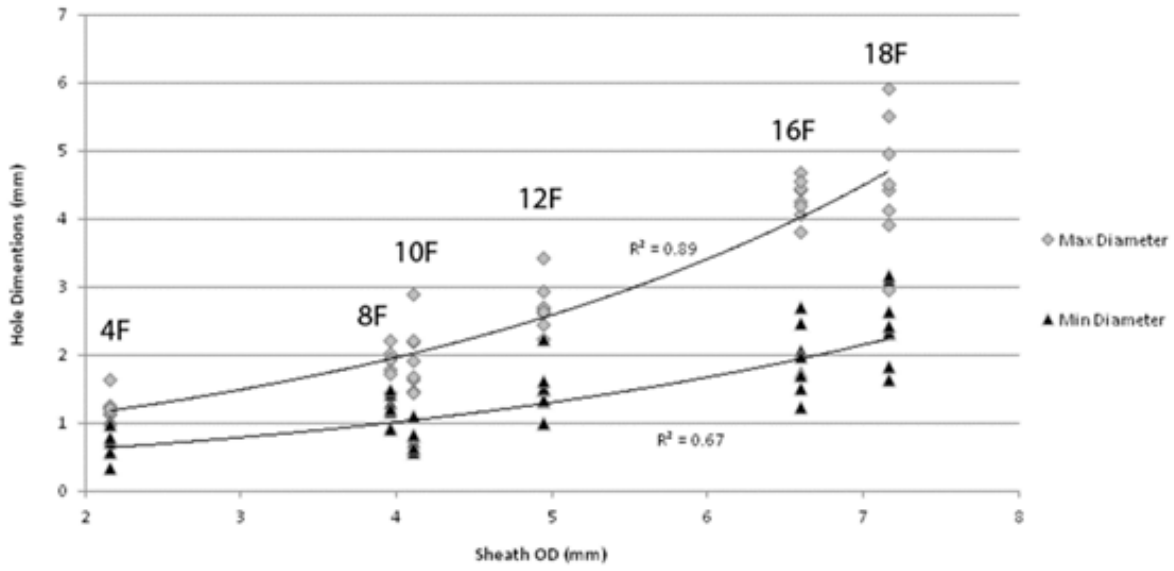

Figure 2.11: Minimum and maximum diameters of induced iatrogenic atrial septal defects, following transseptal punctures employing various sized catheters.

Another important aspect when considering the transseptal crossing of devices relates to the differences in size between the various parts of a catheter system (i.e., the increase in transition diameters going from the dilator to the sheath). Intuitively the increase in the transition gap will require more force to move across the septum (Fig. 2.12).

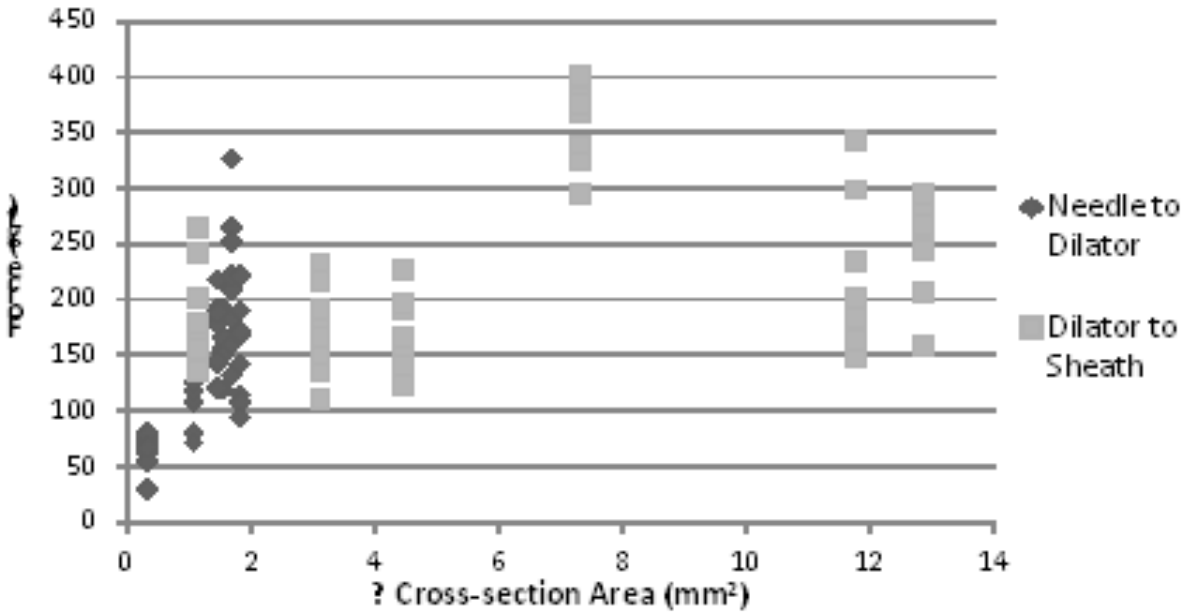

Figure 2.12*:* Relative forces required to transition a catheter system through a septum from one portion of the transseptal puncture sheath to another. An increase in the cross-sectional area of the relative portions of the catheter required more force to pass the catheter through a given septum.

Increasing the diameter discrepancy between the subsequent portions of the TSP sheath requires an increase in force. Our data identified a plateau in forces with the increases in these cross-sectional area differences.

Septal ripping forces

A summary of septum ripping by utilizing different sheath sizes is presented in Table 2.3.

Table 2.3. Summary of fossa ovalis dimensions and sheath tearing forces listed by sheath size

	4 F (n=15)	12 F (n=20)	18 F (n=15)	p-value

Fossa ovalis thickness (mm)	1.1±0.1	1.2±0.1	1.1±0.1	0.727
Superior/inferior width (mm)	16.5±1.1	14.3±0.7	15.7±1.2	0.241
Anterior/posterior width (mm)	10.7±0.9	7.7±0.6	9.2±0.7	0.005
Average tearing force (gf)	258±20	301±26	555±56	p<0.001
Peak tearing force (gf)	344±26	417±37	704±72	p<0.001
Heart weight (g)	487±10	464±13	451±10	0.563

*Values are reported as mean±SE

The chosen direction of induced FO ripping had a significant impact on the resultant average tearing force and peak tearing force ($p<0.05$). Superior-to-inferior induced rips required an average tearing force of 301±26gf, while those elicited in the anterior-to-posterior direction required 363±41gf (Table 2.4).

Table 2.4. Directional differences in septal tearing forces using a 12F sheath

	Superior-to-Inferior (n=20)	Anterior-to-Posterior (n=20)	p-value

Fossa ovalis thickness (mm)	1.2±0.1	1.1±0.1	0.717
Superior/inferior width (mm)	14.3±0.7	14.8±1.1	0.569
Anterior/posterior width (mm)	7.7±0.6	7.9±0.7	0.480
Average tearing force (gf)	301±26	424±41	0.012
Peak tearing force (gf)	417±37	551±60	0.033
Heart weight (g)	464±13	452±18	0.844

*Values are reported as mean±SE

Also, larger forces were required to rip the septa with larger sized sheaths (Fig. 2.13).

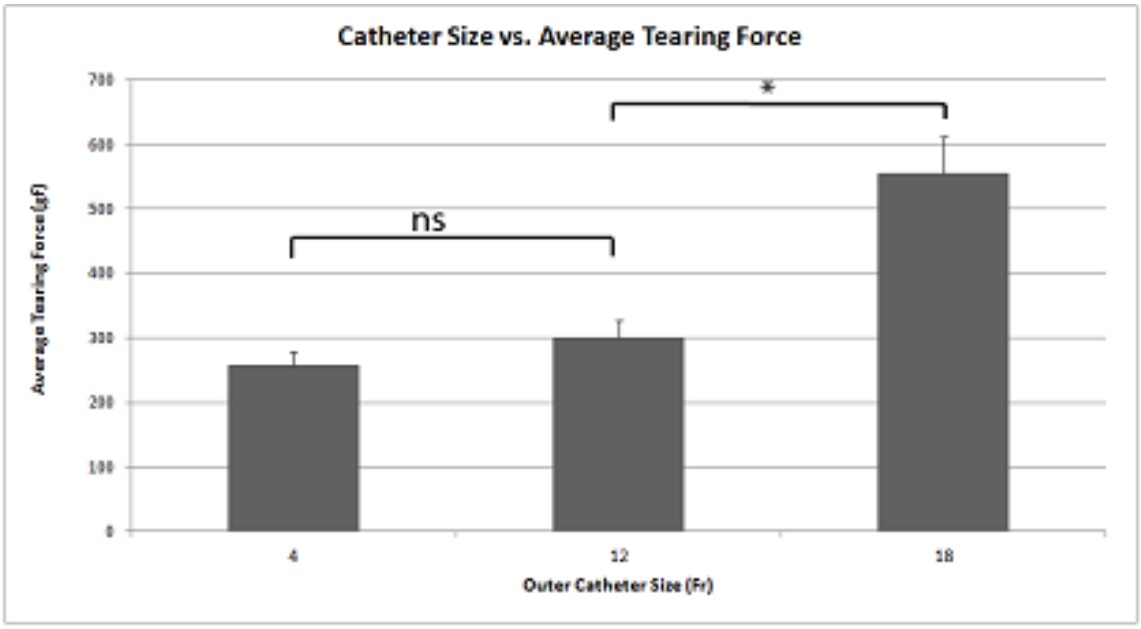

Figure 2.13: Catheter size versus average tearing force. Tearing forces of the fossa ovalis increased with the usage of a larger diameter sheath, but did not significantly differ between the 4F and 12F sheaths ($p>0.05$). Error bars depict mean±SE. *p-value<0.001

The averages of the mean sheath tearing forces were 258±20, 362±25, and 555±56gf for the 4F, 12F, and 18F sheaths respectively; there were significant differences between the sheath sizes and sheath tearing forces between the 18F and 4/12F groups ($p<0.001$). Heart weight, animal weight, FO thickness, and width (superior-to-inferior) did not statistically differ between any of the groups ($p>0.05$).

Tensile testing

We observed no statistical differences in the normalized peak forces, yet the superior-to-inferior pull tests had higher average forces (136±11gf/mm^2) than the associated anterior-to-posterior pulls (116±10gf/mm^2). However, the strain at failure was found to be significantly higher for superior-to-inferior pulls (90±7%) than for anterior-to-posterior pulls (55±7%)($p<0.01$). Interestingly, the determined values for Young's modulus were consistent along both axes with an average value of 32±3kPa (Table 2.5).

Table 2.5. Summary of tensile testing stress, strain, and Young's modulus

	Superior/Inferior (n=22)	Anterior/Posterior (n=19)	p-value
Normalized peak force (gf/mm^2)	136±11	116±10	0.178
Strain at failure (%)	90±7	55±7	0.002
Young's modulus (kPa)	32±2	32±3	0.864

*Values are reported as mean±SE

Heart weight, FO thickness and FO dimensions were not statistically different between the two groups ($p>0.05$, data not shown).

Discussion

There are a number of different procedures requiring TSP including left-sided cardiac ablations, percutaneous mitral valve repairs, mitral balloon valvulotomies, left atrial appendage closures, and certain ventricular assist device placements[44, 50-59]. In many cases, the tissue of the FO is punctured and manipulated with large size devices. This study described a novel series of translational experiments that were performed to better understand the biomedical impacts of procedures that require the transseptal delivery of catheter systems through the atrial septum.

The results of this study showed that a swine model is helpful to determine the forces required for eliciting tenting and punctures, and that the forces measured were less than those seen in humans (121±11gf vs. 146±26gf, $p<0.001$). Further, it is important to note that in both human and swine hearts, with the exception of potentially trying to tent the muscular septum, the relative septal location at which one chose to puncture was not material to the amount of force that may be required to produce tenting. The devices used in this study showed that, on average, the needle tented the septum 9.3±.3mm in humans and 9.8±.14mm in swine hearts ($p=0.2$), prior to ultimately perforating the septum. These outcomes demonstrate the ability of the swine model to serve as a proxy for humans.

In addition, the risk of cardiac tamponade continues to be a concern when conducting the TSP. Using the outcomes from this study, in an a heart ranging from approximately 30mm to 50mm in diameter[70-72], the needle will strain the FO approximately 25% of the distance into the left atrium before perforating and thus protruding into the left atrium. One should also keep in mind that this does not take into consideration that there is a slightly lateral but also superior trajectory on the needle when deployed through most TSP devices. These factors could potentially explain clinical incidents of left atrial perforation and resultant tamponade[54].

Within the puncture data, the relative variability was notably similar between the swine and human tissue groups; the standard deviation was 33% of the mean for human punctures and 37% for swine. Further, these values correlated to 75gf for the swine hearts and 90gf for human specimens, when assessing the Brockenbrough® needle puncture forces alone. Importantly, since the same needle was used, this variation was most likely due to the differences in cardiac anatomy or slight changes in tissue thickness. Another predictor of the force needed to traverse the septum was the difference in the diameter of the catheter system between the various steps of delivery (i.e., between the needle diameter and tip of the dilator diameter). Larger catheters resulted in greater forces required to go across the septum; similarly, it was observed visually that as catheter size increased so did the remnant holes that were created. Additional study of the relationship between remnant holes and catheter size is needed. These remnant holes may contribute to the ability for post-procedure healing. It has been reported that most IASDs close in

patients over time, but in some individuals this can take up to year[49].

An observation was made that subsequent stretching of these tissues required lower forces in swine, especially in the case of the dilator tips and dilation shafts. However, this is not necessarily the case for human tissue. Notably, the dilator tips deployed in the human septum required more than twice the force relative to swine tissue. This can be interpreted to indicate that there are clear distinctive differences between the atrial anatomies of these two species, which could potentially relate to the tissue structure or composition. Yet, it should be noted that another potential source of variability in our data could be associated with varied disease states and cardiac morphologies that were present within the donated human hearts.

While medical device developers are striving to use the smallest types of delivery systems possible, catheter sizes in the realm of overall TSPs are getting larger due to their more complicated nature, e.g., with percutaneous mitral repair systems like the Abbott Mitra Clip being placed through a 22F catheter. Similarly, there is a major industry push to develop transcatheter mitral valve replacement systems that will be delivered via TSP; for comparison, the current transcatheter aortic valve systems utilize delivery catheter sizes ranging from 18F to 24F[31]. Needless to say, new mitral valve delivery catheters would probably be similar in size (if not larger) due to the difference in mitral and aortic valve circumferential areas. Thus when these technologies are deployed in humans, the clinician should have a good understanding of how the septum will react to the TSP[51, 74]. In clinical use, navigating transseptal catheters within the left atrium typically requires

sheath manipulation and risks FO tearing. Although procedures are trending toward larger sheath use, the incidence of FO tearing may be lower due to the larger sheer forces in larger sized catheters (Fig. 2.11). Further studies will need to specifically investigate FO tearing to fully characterize septal damages sustained by various clinical procedures.

The tensile testing of the tissue showed significant differences in the maximal strains upon tissue ruptures. This along with the sheath ripping force differences in the superior-to-inferior and anterior-to-posterior direction seem to indicate that there could be a particular alignment of tissue or fiber orientation that could potentially account for these differences. When a given sheath was being pulled through the floor of the FO in a superior-to-inferior orientation, it caused splitting between the tissue fibers oriented parallel to the direction of pulls, thus accounting for the reduced rip forces in the this orientation as well as the increased strains at failure in the tensile testing. We would predict from the ripping data that the superior-to-inferior direction would be weaker than the anterior-to-posterior direction, but this was not statistically supported by our data. Yet, this suggests that directionality of the rips in the FO is an important factor to consider. The literature reviewed showed that there are currently no histological studies of the FO for any species. We suggest that this may be an important pursuit of future research in order to understand the underlying micro-anatomy and what clinical implications it may have on the structure. Understanding the structural composition of the FO is a topic of ongoing research[75].

Study limitations

The availability of human hearts for such studies is rare as one would expect, thus the majority of described experiments were performed with swine hearts. The use of swine hearts provided a method to test multiple catheter types, and we were able to relate these results to a subset of comparative human tissue trials.

The true mimicking of physiological conditions imposes other issues related to force application on the catheter to puncture the atrial septum while accurately recording the displacement and the load. Using a consistent and repeatable suction device to hold the septum allows for a more controlled study with respect to load and displacement. Along with the consistency, the rate at which the tissue was pulled or punctured was kept consistent as a way to reduce the variables in the experimental setup.

Conclusion

These novel translational in vitro studies of fresh heart specimens, both human and swine, provide a perspective on the challenges of conducting a transseptal procedure and present compelling data for further discussion on the device size constraints as more devices are constructed. In these designed experiments, we specifically observed that swine can serve as a reasonable model to mimic the human condition. In addition, advancements that are tested in the swine model can serve as a more rigorous application due to the more delicate nature of the swine anatomy.

Funding Source: Medtronic, Inc. research contract (Mounds View, MN, USA); Medtronic had no involvement in study design, data collection/analysis/interpretation, or

report writing.

Disclosures: Stephen Howard and Mark Benscoter were graduate students and also employed by Medtronic, Inc.; Paul Iaizzo has a research contract with Medtronic, Inc.

3. Impact of transseptal puncture force on the fossa ovalis: comparison of 12- to 23-French catheter delivery systems and use of traditional and radiofrequency needles

Mark A. Benscoter, [1, 3] Stephen G. Quallich,[1] Megan M. Schmidt,[1] Lars M. Mattison,[1] Paul A. Iaizzo[1, 2]

[1] Department of Biomedical Engineering, University of Minnesota (Minneapolis, MN)

[2] Department of Surgery, University of Minnesota (Minneapolis, MN)

[3] Mayo Clinic, Rochester, MN

Corresponding author:
Dr. Paul Iaizzo
iaizz001@umn.edu
University of Minnesota
B172 Mayo, MMC 195
420 Delaware Street S.E.
Minneapolis, MN 55455
Telephone: (612) 625-9965
Fax: (612) 624-2002

Brief Title: Atrial transseptal crossing using traditional and radiofrequency puncture techniques

Relationship with Industry: Research contract with Medtronic, Inc., Minneapolis, MN.

Preface

The inspiration for this study arose as a result of the previous two chapters. The current method of performing the transseptal puncture has demonstrated a risk of tearing the FO and the current device designs pose a patient safety concern in that the dimensions of the devices along with the procedure technique may puncture unintended thin atrial tissue. In addition, the recent adoption of larger transseptal sheath sizes raise the question of what the limits are for the FO in its ability to resist tearing. The introduction of radio frequency energy applied to the puncture device may promote resistance of the FO to tearing.

Understanding how device size and puncture method interact with the FO are necessary to gain a better understanding of where the limitations may existing in the current device designs. As part of understanding puncture methods, a prototype device is designed, for this study, to examine if the use of RF and a different puncture tool may aid in limiting FO damage in larger size devices.

This chapter is designed to study device design to improve the transseptal puncture as a way to understand limitations that may exist when using different puncture methods for larger sized transseptal devices. The material in this chapter has been submitted for publication to Journal of Interventional Cardiology.

For this study, I was responsible for study design, conducting the data collection, data analysis, and publication creation. Stephen Quallich also contributed to method development, data collection, data analysis, and manuscript editing. Megan Schmidt and Lars Mattison contributed to data collection, data analysis, and manuscript editing. Paul Iaizzo provided editing.

Summary

Background

Left atrial access is required for transcatheter therapeutic approaches, such as mitral valve repair or replacement, left atrial appendage closure or ligation, and left heart endocardial ablation. Advancements in device designs have prompted changes in how catheter delivery systems perform transseptal punctures, including variations in sheath size (12-, 16-, 18-, and 23-French) and the use of radiofrequency (RF) energy instead of mechanical force for device delivery. These changes have raised questions regarding the ability of the fossa ovalis (FO) and associated structures to withstand the biomechanical impact of transseptal puncture force.

Objective

In our study, the primary objective was to quantitatively compare catheter delivery systems of different sizes (12-, 16-, 18-, and 23-French), with and without RF needles, for performing atrial transseptal crossing. Specifically, our focus was on the puncture force required to cross the septum and its impact on anatomic damage (tearing) of the FO. The data will influence device design as well as provide quantitative comparison of transseptal puncture and fossa ovalis compliance to different size devices.

Methods

We analyzed the FO from 167 swine hearts that underwent transseptal punctures using 3 devices: (1) a conventional curved transseptal needle (TN), (2) an RF transseptal needle (RFTN), and (3) a 5-French RF electrode with the tipped with a small segment of a TN

(ETN). We assessed 4 different sized delivery systems (12-, 16-, 18-, and 23-French).

Results

Mean puncture force for the dilator and sheath was significantly different for the 3 methods for the 12-, 18-, and 23-French sizes ($P < 0.05$). Comparing needles, normalized mean puncture force of the TN (100 ± 54.6 grams) was significantly different from the ETN (64.9 ±3 2.9 grams) ($P = 0.01$), but not for the RFTN (76.4 ± 41.2 grams) ($P = 0.11$). Comparing delivery systems, normalized mean puncture force of the 12-French system (100 ± 36.7 grams) was significantly different from the 23-French system (157.6 ± 66.2 grams) ($P = 0.005$), but not the 16-French system (128.8 ± 64.1 grams) ($P = 0.09$) or the 18-French system (86 ± 46.2 grams) ($P = 0.30$). The FO withstood greater peak tearing forces with a 23-French ETN device, as compared with all other sizes ($P = 0.01$).

Conclusions

This study examined the performance of larger delivery systems and the impact of RF when conducting a transseptal puncture to better understand the how larger devices and the use of RF affect puncture and tear performance. Our results are invaluable for clinicians and engineers designing new transseptal medical devices aimed at preventing anatomic damage.

Keywords

Atrial fibrillation, atrial fibrillation ablation, transseptal catheterization, transseptal puncture, left atrial access

Abbreviations

AF = atrial fibrillation, **ETN** = radiofrequency electrode with the tip of a transseptal needle, **FO** = fossa ovalis, **LA** = left atrium, **RF** = radiofrequency, **RFTN** = radiofrequency transseptal needle, **TN** = transseptal needle

Background

Ongoing development of new devices for cardiac therapies continues to rely on performing transseptal punctures to access the left atrium, a technique originally developed by Ross et al. and Cope et al. in 1959. [76, 77] But the increasing size of devices and their subsequent manipulation because of increasing procedural complexity are, more and more, challenging the limits of the fossa ovalis (FO), particularly its ability to stretch without tearing (Figure 3.1).

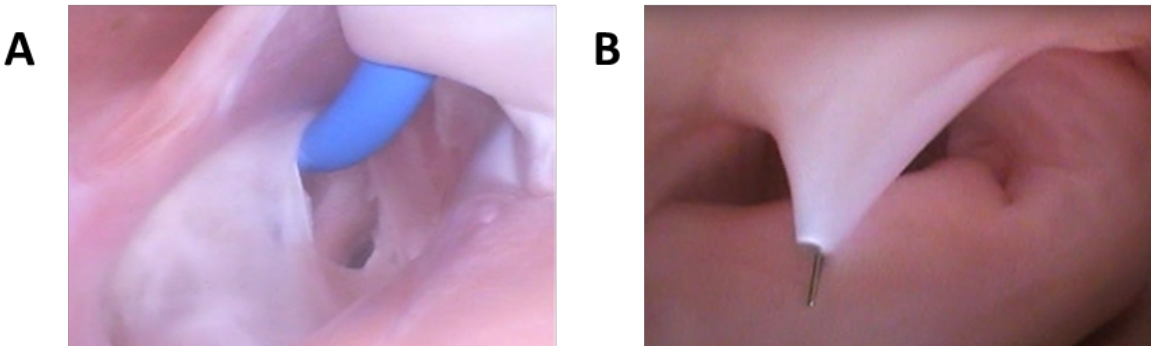

Figure 3.1: The photo on the left (A) shows a swine heart's torn fossa ovalis (FO), with a sheath through the opening made by a transseptal puncture, as viewed from the left atrium. The photo on the right (B) shows a human FO puncture, as viewed from the left atrium.

To successfully treat diseases, it is essential to have access to the anatomy in a way that is least likely to incur injury. Crossing the septum through the FO has a major impact on device delivery into the left heart and on the ability to reach key anatomic locations, such as the mitral isthmus, the mitral valve, and the pulmonary veins. The use of cryogenic balloon ablation therapies, and transcatheter mitral valve repair and replacement devices, requires 12- to 24-French delivery systems. Ideally, systems for accomplishing

transseptal punctures would allow the tissue to dilate and to be manipulated without tearing.

Recent advancements in device designs have prompted changes in how catheter delivery systems perform transseptal punctures, including variations in sheath size (12-, 16-, 18-, and 23-French) and the use of radiofrequency (RF) energy instead of mechanical force. RF-based needles, intended to reduce the risk of cardiac tamponade, use RF energy delivered through the tip of the transseptal needle, typically at 10 watts for a period of 1 to 10 seconds. [78-82]

In our study, the primary objective was to quantitatively compare catheter delivery systems using different sheath sizes (12-, 16-, 18-, and 23-French), with or without RF, for performing atrial transseptal crossing. Specifically, our focus was on the puncture force required to cross the septum and its impact on anatomic damage (tearing) of the FO. We reviewed the puncture force and dilation strain of traditional and RF-based transseptal puncture systems; analyzed the impact of large-diameter delivery systems; and assessed a novel RF device using 4 different delivery system sizes.

Methods

Study population

Fresh swine hearts (n = 167) were obtained (from Glencoe Family Farms, Glencoe, MN, and from the University of Minnesota's Large Animal Veterinary Department, St. Paul, MN, and Visible Heart® Laboratory, Minneapolis, MN). Within 24 hours after the hearts

were excised, we dissected them. We first visualized the FO through the inferior vena cava. Then, we opened the right and left atria to expose the interatrial septum. We removed the septal tissue, taking care to keep intact all tissue surrounding and supporting the FO. Each specimen included at least 5 mm of adjoining atrial septal tissue.

Puncture devices

To perform transseptal punctures of the FO, we used 3 devices: (1) a conventional curved transseptal needle (TN) (Brockenbrough® Medical, Medtronic, Inc., Minneapolis, MN, USA) with a dilator and sheath; (2) an NRG® RF transseptal needle (RFTN) (Baylis Medical Company, Montreal, QC, Canada) with a dilator and sheath; and (3) a 5-French RF electrode with the tip of a TN (ETN) along with a dilator and sheath (Figure 3.2). We used the 5-French ETN to understand whether an initial puncture with a larger RF tool would have an effect on the subsequent force for the dilator and sheath, particularly in the 18- and 23-French sheath sizes.

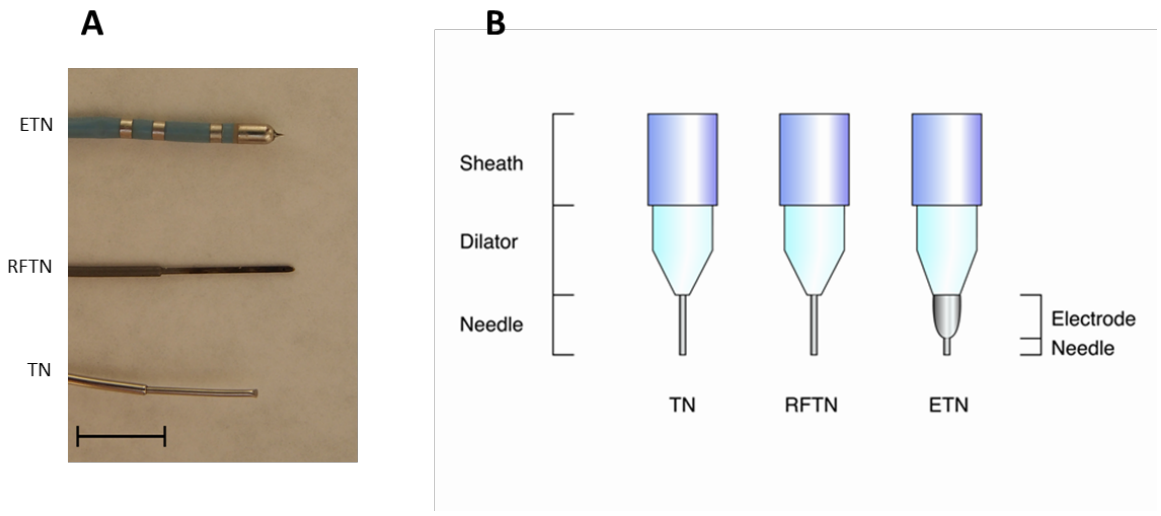

Figure 3.2: The photo on the left (A) shows our study's 3 transseptal puncture devices, from top to bottom (scale bar = 1 cm): a 5-French RF electrode with the tip of a transseptal needle (ETN), a radiofrequency transseptal needle (RFTN), and a conventional curved transseptal needle (TN). The diagram on the right (B) depicts the components of the 3 devices (purple = sheath, green = dilator).

Each delivery system is comprised 3 parts: sheath, dilator, and needle. For dilator dimensions, we defined the *distal diameter* as the diameter of the opening at the tip of the dilator, t*aper length*, as the distance from the tip of the dilator to the end of the tapered section of the dilator on the shaft of the dilator; and *shaft diameter*, as the diameter of the shaft of the dilator at the end of the tapered section. (Table 3.1).

Table 3.1: Dilator dimensions

	12-French TN & RFTN	12-French ETN	16-French TN & RFTN	16-French ETN	18-French TN & RFTN	18-French ETN	23-French TN & RFTN	23-French ETN
Distal diameter (mm)	1.63	2.43	1.57	1.97	1.5	1.95	2.21	2.42
Taper length (mm)	14.02	10.14	65.04	49.5	56.12	59.58	64.15	68.77
Shaft diameter (mm)	3.56	3.5	5.36	5.32	5.82	5.8	7.57	7.59

TN = transseptal needle; RFTN = radiofrequency TN; ETN = 5-French RF electrode with the tip of a TN

For sheath dimensions, the outer diameter was measured (Table 3.2).

Table 3.2: Sheath dimensions

	Sheath size			
	12-French	**16-French**	**18-French**	**23-French**
Outer diameter (mm)	4.84	5.86	6.83	8.60

Force testing

For all force measurements, both the puncture device and the septal tearing method used

the same load cell for force measurements. To measure the puncture and tearing force of the FO, we used the Chatillon TSD110 Digital Force Tester™ (Chatillon, Largo, FL, USA). We mounted the specimens as described by Howard et al. [84] After tissue mounting, we activated the tester with data logging to complete either the FO puncturing or the septal tearing. To determine maximum puncture force, maximum tearing force, and mean tearing force, we used MATLAB (MathWorks, Natick, MA, USA).

FO puncturing

To confirm the puncture location, we directly visualized the FO (Figure 3.3B). The selected needle or electrode was inserted into the dilator until it extended approximately 2 cm past the tip of the dilator, then placed in close proximity against the FO, perpendicular to the center of the FO. The needle or electrode was extended past the tip of the dilator and placed against the FO. Then, the septum was mounted in preparation for puncture (Figure 3.3A). The system was advanced at a rate of 254 mm/min upon the FO until the needle, dilator, and sheath had fully crossed the FO. The remaining pieces of the delivery system were advanced across the FO, with all 3 devices, once the septum was punctured.

The approach was similar with the RFTN. The RFTN was connected to the RF generator (Baylis Medical Company). RF energy was delivered using 10 watts while the entire system was advancing toward the fossa at a rate of 254 mm/min. The rate of movement was set to match the same rate as the conventional curved TN, in an attempt to match current clinical practice. Energy delivery was started before contact with the tissue and terminated after puncture.

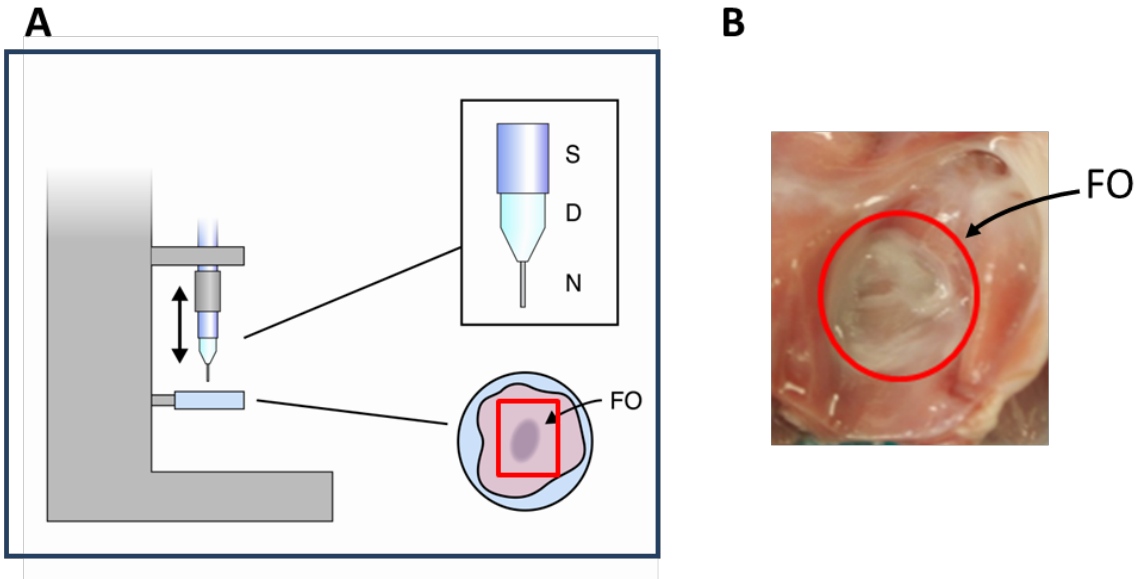

Figure 3.3: The diagram on the left (A) depicts the setup for transseptal punctures, with the device positioned to be inserted through the fossa ovalis (FO) mounted on a plate; all 3 components—sheath (S), dilator (D), and needle (N)—were oriented perpendicular to the specimen. The photo on the right (B) shows septal tissue prepared for puncture (red oval = the FO).

With the ETN, a 5-French electrode using RF energy was delivered using 30 watts with the Medtronic Atakr® (Medtronic, Inc.) generator. The ETN was connected to the RF generator and advanced at a rate of 127 mm/min until puncture was achieved. Note that, with the ETN, the rate was reduced by half, in order to allow time for the RF energy to affect the tissue. The photo and diagram in Figure 3.3 were each derived using a Chatillon TSD110 Digital Force Tester™ (which moved the system and recorded forces). The tissue specimen was bonded to the holding apparatus using Loctite adhesive (Henkel Corporation, Westlake, OH, USA).

Contained within the dilator of the ETN was a 5-French electrode with a TN tip at the distal end, which enabled contact with the tissue. The outer diameter (OD) of the dilator and the inner diameter (ID) of the sheath were similar to prevent the presence of a gap at the interface of each. In addition, the dilator had a tapered tip to allow for easy advancement across the septum, reducing the risks of tearing the FO. The dilator tip of the ETN was placed against the tissue to induce a mild degree of tenting. The device was advanced, while energy was delivered to the tip, to perform the puncture. The internal lumen of the dilator remained unobstructed, to allow for the needle and electrode to pass through the lumen and extend beyond the tip of the dilator. The amount of needle extension beyond the tip of the dilator was predetermined, given a restriction in the internal diameter of the dilator at the tip. The 5-French electrode was placed on the tip of a flexible Pebax® shaft (Arkema, Colombes, France**)** and then inserted through the inner lumen of the dilator. The catheters were attached using a custom fixture to a load cell for obtaining continuous puncture forces.

Septal tearing

For our septal tearing experiments, we used 86 of the swine hearts (range, 175 to 625 grams). For each specimen, we excised the FO and surrounding tissue. Then, we punctured each FO with 1 of our 3 devices (a TN, an RFTN, or an ETN). Next, we advanced the dilator and sheath (12-, 16-, 18-, or 23-French) through the specimen.

Once the puncture was performed, we mounted the specimen on the fixture such that no force was being placed against the specimen as described by Howard et al. [84] The delivery system was maintained in a perpendicular position relative to the FO via a

custom fixture. To remove any excess septal tissue, we made a cut superior to the FO,—thereby ensuring that only FO tissue would tear during each test, while leaving the surrounding septal tissue unaffected. For each test, we used a TSD110 Digital Force Tester™ to pull the sheath away from the base, tearing through the tissue at a rate of 100 mm/min. The atrial septa were ripped in an inferior to superior direction. Once the sheath was no longer in contact with tissue, the test was terminated. We defined *sheath tearing force* as the mean force while the septum primum was tearing. We adapted our FO tearing method from Howard et al. [84] For our study, we recorded all FO dimensions, as well as mean and peak sheath tearing force.

Statistical analysis

Each experiment included randomized specimens of the variables, along with *t* tests and *P* values (set at < 0.05), to determine statistically significant differences between means. To examine the influence of change in variation, we normalized the puncture force data, using a needle type and sheath size as a reference point. To examine the relationship between the anatomy and puncture devices, we used analysis of variance (ANOVA) with a resulting R^2value. For all analysis, we used Minitab version 12 (Minitab Inc., State College, PA, USA).

Results

In our comparison of the needle subgroups, we found that sheath size affected the force to cross the septum and the FO's resistance to tearing. In addition, the use of RF energy changed the force necessary to cross the FO. To the best of our knowledge, our study is

the first to show how a larger puncture device can acutely affect performance of transseptal punctures, sometimes doing so as well as, or even better than, more traditional methods (Figure 3.4).

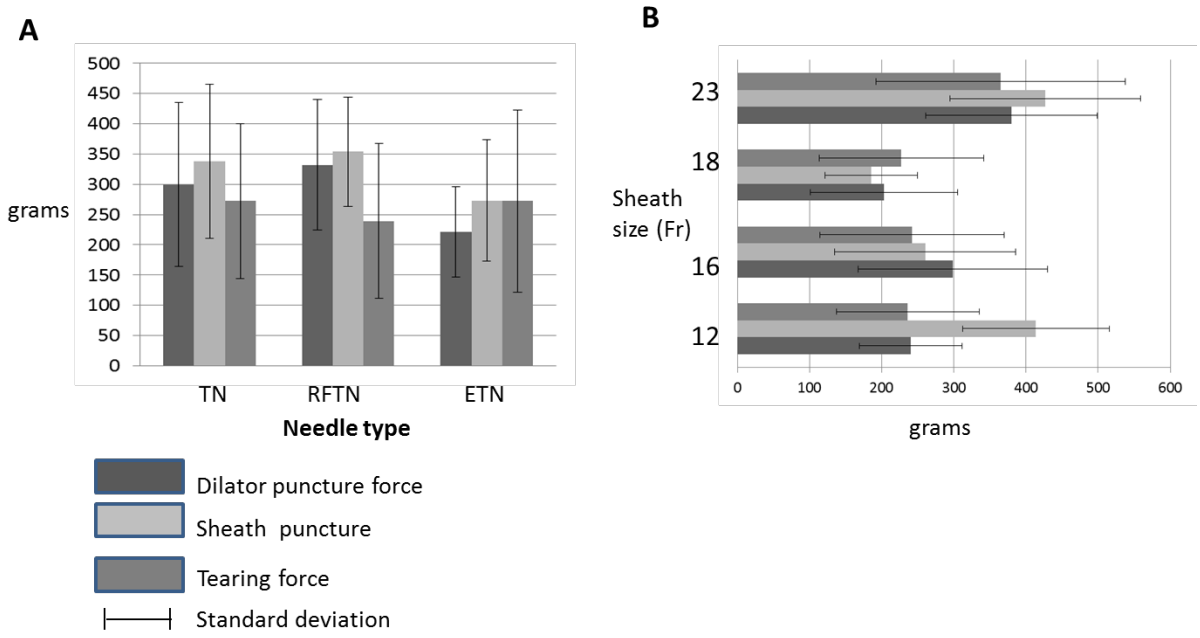

Figure 3.4: The diagram on the left (A) depicts force data (in grams) for all tearing and puncturing, *by needle type*: transseptal needle (TN), radiofrequency TN (RFTN), or 5-French RF electrode with the tip of a TN (ETN). The diagram on the right (B) depicts force data (in grams) for all tearing and puncturing, *by sheath size*: 12-, 16-, 18-, or 23-French.

To analyze our results, we first divided all data points into subgroups by needle type (TN, RFTN, and ETN); for those 3 subgroups, we calculated the mean and standard deviation (SD) for the *dilator* (TN, 299.5 ± 135.3; RFTN, 332.1 ± 107.6; and ETN, 221.1 ± 74.7 grams), *sheath size* (TN, 337.8 ± 126.9; RFTN, 353.9 ± 90.2; and ETN, 272.9 ± 100.4 grams), and *tearing force* (TN, 272 ± 128; RFTN, 239 ± 128; and ETN, 272 ± 151

grams) independent of sheath size (Figure 4A). Then, we divided all data points into subgroups by sheath size (12-, 16-, 18-, and 23-French); for those 4 subgroups, we calculated the mean and SD for the *dilator* (12-French, 240.4 ± 71.3; 16-French, 298.8 ± 131.3; 18-French, 202.7 ± 102.01; and 23-French, 379.8 ± 118.9 grams) *sheath size* (12-French, 413.7 ± 101.4; 16-French, 260.2 ± 125.5; 18-French, 185.4 ± 64.3; and 23-French, 426.9 ± 132.1 grams) and *tearing force* (12-French, 236 ± 9; 16-French, 242 ± 128; 18-French, 227 ± 114; and 23-French, 365 ± 173 grams) independent of needle type (Figure 3.4B).

FO puncturing

Our study produced a total of 81 punctures from 81 specimens collected. We first analyzed puncture force across all sheath sizes by the 3 components (needle, dilator, sheath) of the delivery system (Figure 3.5A).

Then, we calculated the mean and SD of each of our 3 devices across all sheath sizes (TN, 300.7 ± 163.1; RFTN, 207.6 ± 139.4; and ETN, 181.8 ± 93.5) (Figure 5B). The puncture force for the 2 RF-based methods (RFTN, ETN) was significantly less than for the TN (RFTN vs. TN, $P = 0.03$; ETN vs. TN, $P = 0.004$).

Finally, we examined the puncture force of each paired dilator/sheath combination. In our analysis of all 81 specimens, we found no relationship between the dilator and sheath puncture force ($R^2 = 0.29$) (Figure 3.5C).

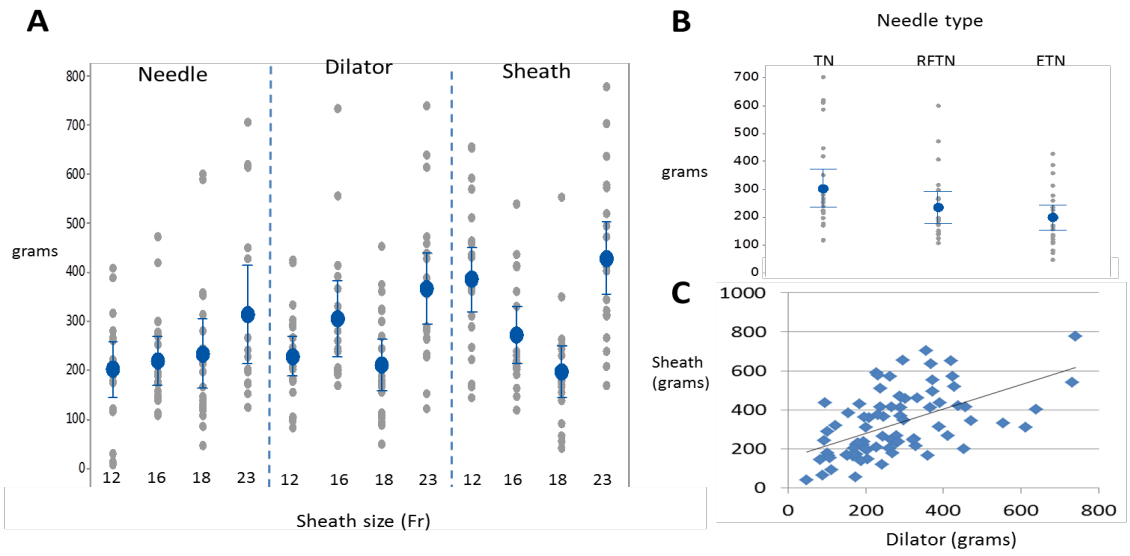

Figure 3.5: The diagram on the left (A) shows, for all specimens, the mean puncture force and standard deviation (SD) (in grams) for the needle, dilator, and sheath *by sheath size*. The diagram on the top right (B) shows, for all specimens, the mean puncture force and SD (in grams) *by needle type*: transseptal needle (TN), radiofrequency TN (RFTN), or 5-French RF electrode with the tip of a TN (ETN). The diagram on the bottom right (C) shows the relationship between dilator and sheath puncture forces with an overall R^2 of 0.29.

Next, we grouped all data points by sheath size (12-, 16-, 18-, and 23-French) and then placed them in subgroups by needle type (TN, RFTN, and ETN) (Figure 3.6). To determine any significant differences in the amount of force to cross the FO, we compared each of our delivery systems against the 12-French system, which is used extensively in transseptal applications. Using the TN, we found significant differences between the 12- and 18-French sheath (P = 0.001) and between the 12- and 23-French dilator (P = 0.003). Using the RFTN, all of the sheath forces were significantly different from the 12-French (16-French, P = 0.003; 18-French, P = 0.001; and 23-French, P = 0.004). Using the ETN, we found significant differences between the 12- and 18-French sheath (P = 0.001) and between the 12- and 23-French dilator (P = 0.05).

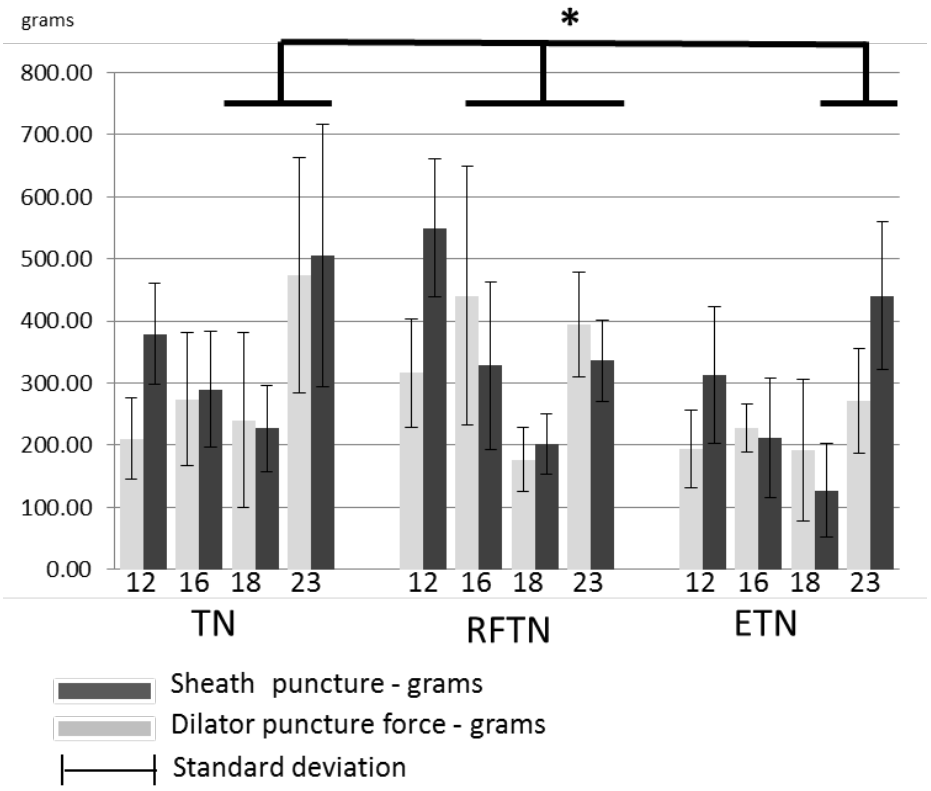

Figure 3.6: This diagram shows the mean puncture force and standard deviation (in grams) *by needle type and sheath size*. * $P \leq 0.05$

Given the specimen variation associated with inherent FO tissue properties, we performed an additional analysis and normalized the data to remove the specimen variation.

First, we normalized the puncture methods, with the TN as the reference. By doing so, the mean force to cross the FO was not significantly different from the TN when using the RFTN ($P = 0.11$), but the mean force *was* significantly different when using the ETN ($P = 0.01$) (Figure 3.7A).

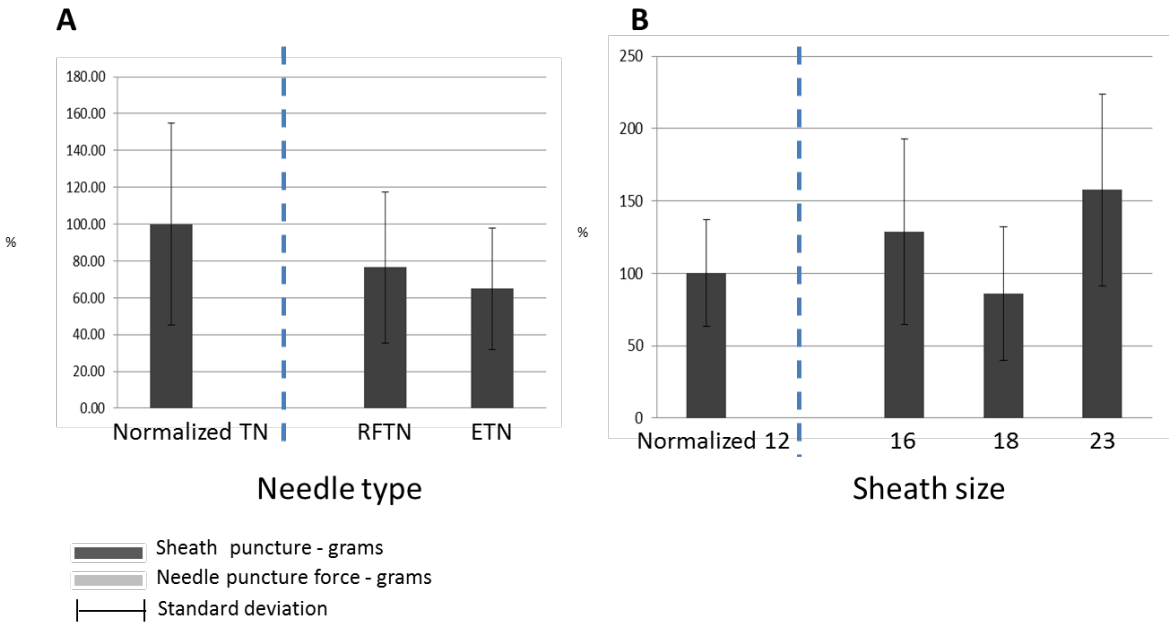

Figure 3.7: The diagram on the left (A) depicts the puncture force (in grams), with data normalized against the transseptal needle (TN) and 12-French size, *by needle type*: TN, radiofrequency TN (RFTN), or 5-French RF electrode with the tip of a TN (ETN). The diagram on the right (B) depicts the transseptal crossing force (in grams) *by sheath size*: 12-, 16-, 18-, or 23-French.

Second, we normalized sheath sizes. Using the 12-French as the reference point, we found that the force to cross the FO when using a 23-French sheath was significantly different ($P = 0.005$). However, we found no significant differences when using either the 16-French ($P = 0.09$) or the 18-French sheath ($P = 0.30$) (Figure 3.7B).

Septal tearing

The baseline septal tearing characteristics by needle type are summarized in Table 3.3; by sheath size, in Table 3.4. The anatomic measurements of the FO, by sheath size and needle type, are presented in Table 3.5. The baseline FO characteristics by needle type are summarized in Table 6; by sheath size, in Table 3.7. We found a statistically significant difference between the tearing force of the 23-French sheath as compared with

the 12-, 16-, or 18-French sheaths (Figure 3.5). However, needle type had no statistically significant impact on tearing initiation distances or on either mean or peak tearing forces ($P > 0.05$).

Table 3.3: Baseline tearing characteristics by needle type

	TN (n = 26)	**RFTN (n = 28)**	**ETN (n = 32)**	***P***
Tearing initiation distance (mm)	7.5 ± 3.2	6.8 ± 3.1	5.8 ± 2.7	0.068
Mean tearing force (gf)	272 ± 128	239 ± 128	272 ± 151	0.55
Peak tearing force (gf)	360 ± 173	306 ± 161	372 ± 208	0.33

TN = transseptal needle; RFTN = radiofrequency TN; ETN = 5-French RF electrode with the tip of a TN

Table 3.4: Baseline tearing characteristics by sheath size

	12-French (n = 23)	**16-French (n = 23)**	**18-French (n = 21)**	**23-French (n = 19)**	***P***
Tearing initiation distance (mm)	6.7 ± 2.7	6.0 ± 2.4	7.0 ± 3.7	6.4 ± 3.1	0.72
Mean tearing force (gf)	236 ± 99	242 ± 128	227 ± 114	365 ± 173	0.002
Peak tearing force (gf)	308 ± 138	312 ± 157	296 ± 139	515 ± 233	< 0.001

TN = transseptal needle; RFTN = radiofrequency TN; ETN = 5-French RF electrode with the tip of a TN

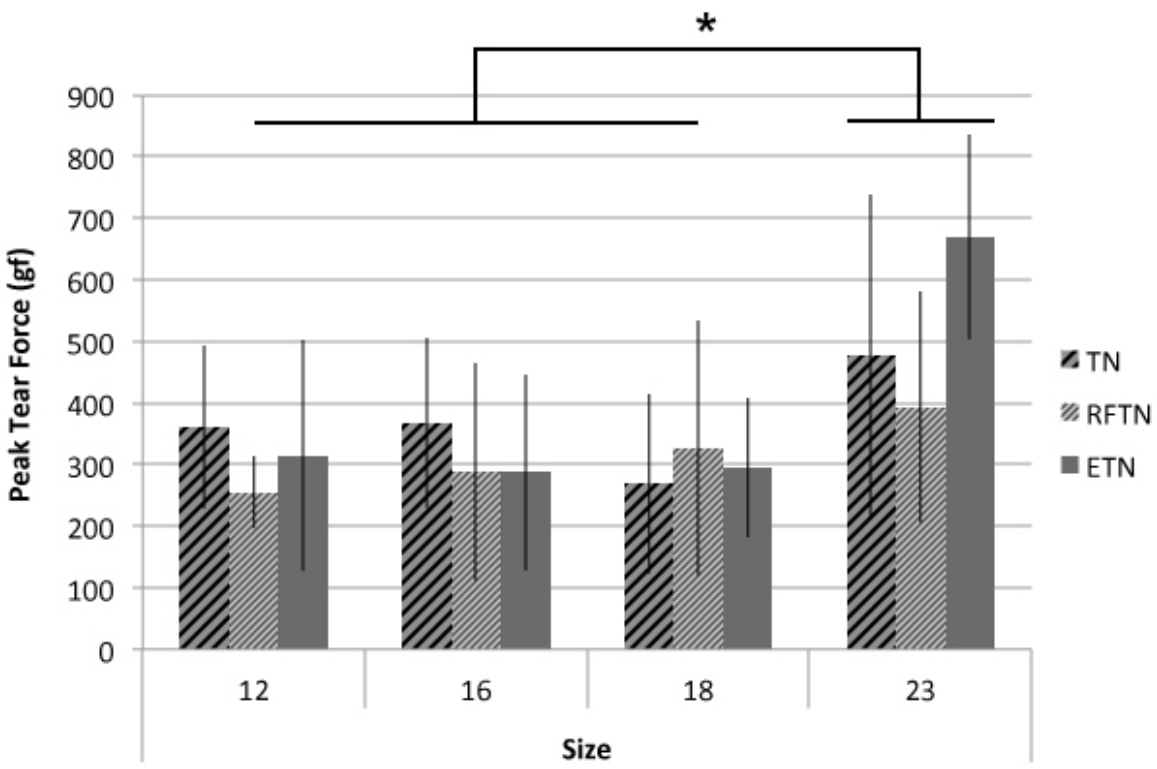

Figure 3.8: This diagram depicts the peak septal tearing forces *by sheath size*: 12-, 16-, 18-, or 23-French. The only significant difference occurred when using the 23-French sheath, as compared with the other 3 sizes. *$P < 0.001$

Anatomic variation

Anatomy for puncture

The variation in anatomy among our specimens affected both the FO puncturing process and the septal tearing forces.

FO puncturing

Overall, we found only a narrow variation in the FO thickness of our specimens (0.46 ± 0.07 mm). We found no statistically significant relationship between FO thickness and the type of device used (R^2 for TN, 0.001; ETN, 0.005; and RFTN, 0.11) (Figure 3.9).

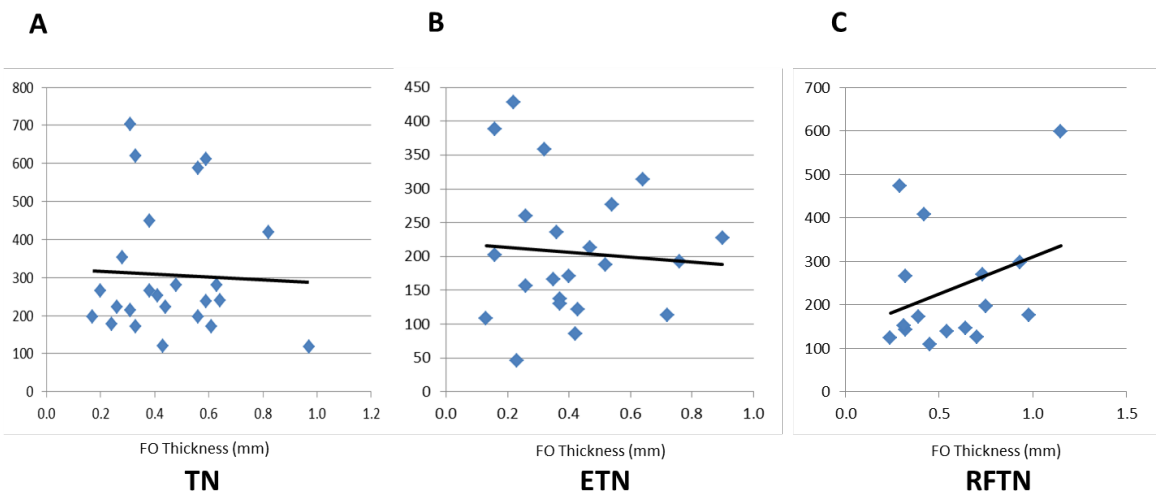

Figure 3.9: This 3-part diagram depicts the relationship between FO thickness (in mm) and puncture force (in grams) using (A) the transseptal needle (TN); (B) the 5-French radiofrequency electrode with the tip of a TN (ETN); and (C) the RFTN.

In addition, we analyzed the relationships between sheath size (12-, 16-, 18-, or 23-French) and FO anatomic measurement by needle type, but found no statistically significant differences (Table 3.5).

Table 3.5: Anatomic measurements of the fossa ovalis

12-French	**TN**	**RFTN**	**ETN**	***P***
SI length (mm)	13.5 ± 2.8	11.6 ± 3.7	15.7 ± 4.1	0.56
AP length (mm)	7.2 ± 2.6	7.8 ± 2.4	7.07 ± 2.05	0.89
Thickness (mm)	0.39 ± 0.3	0.5 ± 0.1	0.32 ± 0.1	0.14
16-French				
SI length (mm)	12.9 ±3.5	15.3 ± 2.9	13.7 ± 4.6	0.47
AP length (mm)	8.6 ±4.9	7.1 ± 5.3	7.7 ± 2.2	0.89
Thickness (mm)	0.5 ±0.1	0.6 ± 0.3	0.5 ± 0.1	0.75
18-French				
SI length (mm)	15.3 ± 3.3	14.5 ± 4.4	13.9 ± 2.1	0.87
AP length (mm)	8.3 ± 3.4	7.9 ± 2.6	8.3 ± 2	0.94
Thickness (mm)	0.4 ± 0.1	0.6 ± 0.3	0.3 ± 0.1	0.11
23-French				
SI width (mm)	12.4 ± 4.5	13.5 ± 1.3	17.0 ± 7.1	0.45
AP width (mm)	6.9 ± 3.3	8.2 ± 1.8	10.1 ± 5.6	0.42

Thickness (mm)	0.4 ± 0.1	0.4 ± 0.1	0.29 ± 0.26	0.25

TN = transseptal needle; RFTN = radiofrequency TN; ETN = 5-French RF electrode with the tip of a TN; SI = superior/inferior length; AP = anterior/posterior length

Septal tearing

We collected anatomic measurements for all of the specimens used for tearing, to determine any relationship between anatomy and tearing resistance, but found none.

Table 3.6: Baseline fossa ovalis characteristics by needle type

	TN (n = 26)	RFTN (n = 28)	ETN (n = 32)	*P*
SI length (mm)	11.8 ± 2.3	14.4 ± 4.5	13.2 ± 2.5	0.01
AP length (mm)	5.8 ± 2.2	8.6 ± 4.5	7.8 ± 2.0	< 0.001
Thickness (mm)	0.8 ± 0.5	0.9 ± 0.7	0.9 ± 0.3	0.58
Heart weight (grams)	387 ± 81	415 ± 110	376 ± 74	0.22

TN = transseptal needle; RFTN = radiofrequency TN; ETN = 5-French RF electrode with the tip of a TN; SI = superior/inferior length; AP = anterior/posterior length

Table 3.7: Baseline fossa ovalis characteristics by sheath size

	12-French (n = 23)	16-French (n = 23)	18-French (n = 21)	23-French (n = 19)	*P*
SI length (mm)	13.3 ± 3.2	12.6 ± 2.7	12.7 ± 3.6	14.2 ± 3.6	0.37
AP length (mm)	7.7 ± 3.6	7.3 ± 3.0	7.3 ± 2.2	7.8 ± 3.0	0.92
Thickness (mm)	0.8 ± 0.4	1.0 ± 0.6	0.9 ± 0.5	0.8 ± 0.5	0.49
Heart weight (grams)	379 ± 109	408 ± 80	391 ± 89	389 ± 79	0.75

TN = transseptal needle; RFTN = radiofrequency TN; ETN = 5-French RF electrode with the tip of a TN; SI = superior/inferior length; AP = anterior/posterior length

We found a statistically significant difference between when each method of puncture was compared against the (SI) length ($P = 0.01$) the (AP) length ($P < 0.001$) (Table 3.6). But we found no other statistically significant differences. Although samples were randomized, there was a significant difference between anterior/poster and superior/inferior width for the needle groups ($P < 0.05$)

Discussion

Our study was the first of its kind to assess the forces required to perform a transseptal puncture through the FO. Our 4 main findings were as follows: (1) In the case of 16- and 23-French sheath systems, the force required to cross the FO is higher than for a 12-French system; (2) When comparing our 3 types of devices, the ETN significantly differed from the TN, but the RFTN did not; (3) With the 23-French sheath size, the FO's tearing resistance was significantly higher than the other sizes; and (4) Between the 12-, 16-, and 18-French sheath sizes, the FO's resistance to tearing did not significantly differ.

FO puncturing

When comparing the TN with the RFTN, the TN resulted in lower transseptal crossing forces of the dilator and sheath with the smaller 12- and 16-French systems, and the RFTN resulted in lower transseptal crossing forces with the 18- and 23-French systems. The use of the larger ETN resulted in lower mean transseptal crossing forces with the 12-, 16-, and 18-French systems. It is possible that the RF lesion created by the ETN enabled the dilator and sheath to cross with greater ease, as we also observed with the RFTN.

The dimensions of the dilators and sheaths might contribute to differences in forces by delivery system size. The variation in forces by delivery system size and by needle type might be due to the unique design of each dilator. Additional work is necessary to optimize dilator tip design. Our data (normalized against the 12-French system) showed no significant differences in mean puncture forces with the 16- and 18-French systems. The lack of differences in normalized mean puncture forces may be due to design elements such as tip contour or tolerance differences between each component of the

delivery system.

Furthermore, when comparing all needle types by sheath size, FO thickness had no significant impact. However, the difference in FO thickness with the ETN subgroup was significantly smaller than with the other 2 devices ($P < 0.05$). Our additional analysis comparing FO thickness and puncture force (grams) revealed, with all 3 needle types, the lack of a strong correlation between FO thickness and puncture force. Thus, the variable of FO thickness might have been a confounding factor. In future studies, a broader selection of same-size devices is warranted, in order to explore the variation from device to device within a particular size.

It is important to note that during transseptal punctures with the 5-French electrode needle (i.e., with the ETN), we observed, in some specimens, steam pops when using a power setting of 30 watts. The use of RF energy might cause the tissue temperature to increase, resulting in dielectric breakdown and vaporization of the fluid, damage to the adjacent tissue, and release of the contents as a steam pop. In our observed cases, the amount of power applied exceeded the amount required to cause rupture and resulted in fluid vaporization near the tip of the catheter. With the optimization of applied power and temperature settings, it might be possible to control the energy delivery and eliminate this phenomenon; the literature suggests that tuning ablation parameters can minimize steam pop occurrences. [83]

These results indicate that additional studies of a larger RF-based device might yield improvements in reducing the amount of force required to perform transseptal punctures.

The lack of a significant difference between the normalized mean puncture force of the TN and RFTN might be associated with the amount of power delivered or with insufficient time exposure of the tissue subject to the RF (given the effects of the mechanical force of the needle against the tissue). Anatomic variation of FO size and thickness might contribute to the variation in the forces for FO puncturing and septal tearing. Using the TN as a baseline, we found that either the ETN or RFTN led to comparable or better results—evidence that all 3 devices perform similarly. A chronic study is required with several months of follow-up to examine the post-procedure recovery of the FO and to investigate the post-procedure healing of punctures performed by both mechanical and RF methods.

Septal tearing

We observed significant differences in septal tearing properties by sheath size; our results correspond with previous investigations. [84] It appears that a critical sheath diameter exists at which tearing forces dramatically increase (Figure 3.8). As new procedures continue the trend toward larger catheter sizes to reduce septal tearing, the initial puncture holes created are still of concern. Yet, the clinical implications of iatrogenic atrial septal defects remain to be clinically determined. It is important to note that some physicians are already using closure devices to treat these defects.

Regardless of the needle type (TN, RFTN, or ETN), we found no statistically significant differences in the tearing forces with the 12-, 16-, and 18-French systems. This finding suggests that, on an acute scale, no single technology has demonstrated a clear reduction in iatrogenic atrial septal defect size. Someday, technologies may facilitate tissue

remodeling resulting in better closure. Future investigations are needed to determine whether or not transseptal punctures aided by RF will generate better natural closure in the long term.

Additional work is needed to better understand the ETN and to account for variations in anatomic differences. Opportunities also abound to further investigate different iterations of the ETN that may perform better than the one we used.

Study limitations

In our analyses of the septal tearing tests, we assumed that the surrounding anatomy of the FO had little impact on the observed forces. Depending on the pertinent anatomy targeted in the procedure, catheter torquing might be amplified, resulting in changes in tearing forces. An in vivo study or a biomechanical model examining this behavior would aid in identifying the importance of other factors relative to septal tearing.

In addition, our study focused on transseptal elements at the time of puncture. Additional work is needed to study the residual hole that is formed, including a safety study to examine FO healing.

Although our study found no statistically significant difference by needle type and FO thickness, additional work is needed to study the interactions between device size and anatomic variation in FO thickness and size.

Finally, the ability to perform similar studies on fresh tissue isolated from human hearts would be ideal; such studies are ongoing in our laboratory, but it will take time to acquire

the necessary specimens.

Conclusion

Ours is the first study to characterize how the currently accepted TN compares with the RFTN and ETN. Using a range of devices and catheter sizes, we successfully showed the relative puncture and tearing forces required to perform transseptal punctures and FO tearing. Normalized mean puncture forces using the TN and RFTN were not different.

Additional studies aimed at reducing septal puncturing and tearing forces are needed, optimizing designs by refining not only the shapes and sizes of delivery systems but also the power used. Solutions must be found to improve the safety of transseptal punctures.

Acknowledgments

This work was done in collaboration with all authors listed, along with the editing support of Dr. Mary Knatterud. We appreciate all of the contributions to this study.

4. Visualization of an innovative approach for mitral isthmus ablation

Mark A. Benscoter, MS[1, 3], Boaz Avitall, MD, PhD FHRS[5], Paul A. Iaizzo, PhD[1, 2, 4]

[1]Department of Biomedical Engineering, University of Minnesota (Minneapolis, MN)

[2]Department of Surgery, University of Minnesota (Minneapolis, MN)

[3]Mayo Clinic (Rochester, MN)

[4]Institute for Engineering in Medicine, University of Minnesota (Minneapolis, MN)

[5]Department of Medicine, Section of Cardiology, University of Illinois at Chicago (Chicago, IL)

Corresponding author:
Dr. Paul Iaizzo
iaizz001@umn.edu
University of Minnesota
B172 Mayo, MMC 195
420 Delaware Street S.E.
Minneapolis, MN 55455
Telephone: (612) 625-9965
Fax: (612) 624-2002

Brief Title: Anatomical challenges associated with mitral isthmus ablation

Keywords: Atrial fibrillation, catheter ablation, mitral isthmus, coronary sinus

Abbreviation List: AF = atrial fibrillation, CS = coronary sinus, LA = left atrium, MI = mitral isthmus

Preface

The inspiration for this study arose as a result of the review chapter. Limitations in the ability to place catheters in specific locations pose a therapeutic and patient safety risk. Insufficient contact and orientation of the therapeutic catheter can result in insufficient lesion depth that could result in extended procedure times or a redo of the ablation at a future date. Devising new techniques based on direct visualization of the device tissue interface provides insights into the procedure to illustrate how to effectively apply ablation devices. The results of this study will be submitted to Heart Rhythm Journal. For this study, I was responsible for study design, conducting the data collection, image analysis, and publication creation. Both Boaz Avitall and Paul Iaizzo provided editorial support. In addition, Boaz Avitall conducted catheter navigation during the procedure to ensure the devices were used in a way to mimic clinical procedure.

Introduction

Post-ablation reoccurrences of atrial fibrillation (AF) continues to be a concern in the treatment of patients. [85, 86] Therefore, several adjuvant procedures have been promoted to improve overall outcomes. One of these, the ablation of the mitral isthmus (MI) has emerged in an attempt to decrease the likelihood of macro-reentrant tachycardia. [87, 88, 89, 90, 91] Nevertheless, the creation of a transmural MI block for the treatment of AF is often quite difficult to achieve as good catheter placement, stability and tissue contact are challenging due to a given patient's anatomy. [87] Incomplete lesion sets may lead to a slow conduction path that could result in left atrial tachycardia. [92, 93, 94, 95]

In this report we have employed direct imaging modalities within a reanimated human heart during the placement of a catheter against the MI as a means to provide novel educational tools for physicians, design engineers, and/or patients: i.e., to better understand the specific limitations of the current procedure and suggested procedural changes that can lead to improve linear lesion generation.

Experimental Setup

A human heart was reanimated in a clear Krebs-henseleit buffer using Visible Heart® methodologies and endoscopic footage during an ablation procedure was obtained. [96, 97] This heart was considered nonviable for transplantation (recovered via LifeSource, St. Paul, MN): we also used numerous reanimated swine heart studies to validate these ablative approaches. The catheters were advanced through the inferior vena cava (IVC), across the fossa ovalis (FO), to the anatomical location of the LA MI. A Contactr 8mm radiofrequency catheter (Medtronic, Inc., Minneapolis, MN, USA) was advanced through

a transseptal sheath to the desired position against the MI. The catheter ablation was conducted per the manufacturer's recommended settings using temperature mode at 65 degrees of a period of a total time of 17 minutes and then removed.

Shown in Figure 4.1, the catheter tip was placed next to annulus of the mitral valve (MV). A second diagnostic catheter is inserted through a sheath and placed such that the interior of the deflection point of the ablation catheter rested on the shaft of the diagnostic catheter. The tip of the diagnostic catheter is logged in the PV to anchor the diagnostic catheter and restrict the movement of the ablation catheter. The ablation energy was turned on and a lesion was created as the catheter was dragged toward the ostium of the pulmonary veins (PV), which are located in the center of the screen below the ablation catheter shaft (Figure 4.1A). As the ablation catheter was pulled along the ridge, the ablated tissue appeared to become dimpled and changed in color (Figure 4.1B).

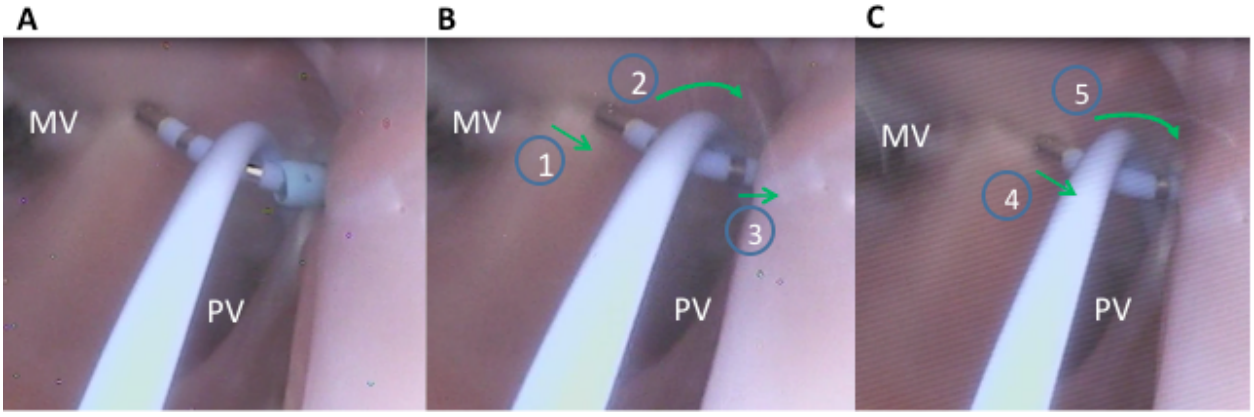

Figure 4.1: Mitral isthmus linear lesion was created in a reanimated human heart: (A) shown in the initiation of linear lesion with support from transseptal sheath and secondary diagnostic catheter; (B) the ablation catheter –1– is pulled along MI with twisting of diagnostic catheter -2- towards FO and retraction of transseptal sheath – 3 – from LA; (C) shown is an increased deflection of ablation catheter – 4 – and increased twisting of diagnostic catheter – 5. The uses of both the transseptal sheath and a support catheter was advantageous to maintain contact on the MI. LA – left atrium, MI – mitral isthmus, MV – Mitral valve, PV – pulmonary vein

The catheter was then advanced over a ridge in the LA. To generate good contact, abundant deflection of the ablation catheter tip was required and the delivery sheath was also utilized for added support. (Video Appendix A) Yet, during the course of the ablation, the delivery sheath was retracted into the RA to better allow for the ablation catheter tip to maintain contact as it was pulled across the MI (Figure 4.1C). Persistent contact between the ablation catheter and diagnostic catheter were required in order to maintain tip orientation and prevent the ablation tip from sliding along the tissue. (Figure 4.1B) Finally, the support of the diagnostic catheter prevented the ablation catheter from changing orientation to its side. During the course of being able to visualize such ablation procedures, we observed that there may often be a procedural need for a high number of deflections of the given ablation catheter; i.e., in some cases a MI ablation may require a 90-120 degree deflection of the delivery sheath at its distal tip, so to achieve placement of the ablation catheter in the desired location (see supplemental video – Appendix A).

Upon completion of the human heart, this procedure was validated in a swine model to examine the effectiveness of the technique using a post procedure lesion assessment. Swine post-procedural evaluations included the use of triphenyl tetrazolium chloride (TTC):

i.e., each sample was placed in a TTC bath for 20 minutes to allow for the creation of color differentiation, health versus dead tissue: ablated tissue appears blanched and non-ablated tissue was deep purple. (Figure 4.2)

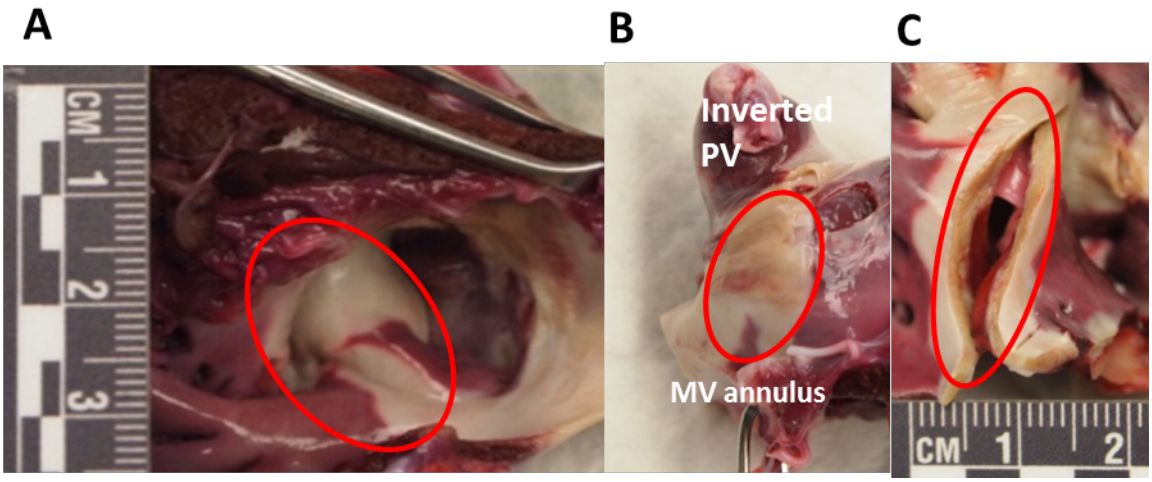

Figure 4.2: Shown are several views of sectioned and TTC stained left atrial samples: (A) the ablated atrial tissue appear as blanched; (B) shown is the PV inverted and the MI line is circled; and (C) cross-section view of linear mitral isthmus lesion, depicting transmurality**.**

Via the staining, the presence of the ablated region became quite visible (Figure 4.2A). The pulmonary vein and atrial tissue was then inverted to further examine the full extent of the linear lesion which extended form the MV annulus to the PV ostium (Figure 4.2B). Finally, the lesion was sliced to examine lesion transmurality (Figure 2C). These results show that the ability to generate a successful lesion in this MI anatomy is influenced by maintaining tip orientation and high tissue contact. In this case, these were influenced

by, the support of a delivery sheath that was retracted into the RA during the ablation, and a secondary support catheter was also used to provide support to the ablation catheter.

Discussion

This clinical approach shown here is an innovative way to utilize currently available ablation tools as a means to increase the success rate of achieving a transmural lesion of the MI. Studies showing that conduction block at the MI can be challenging, reinforce the need for advanced ways to treat such patients.[98] The presence of the ridge that may boarder between the MVA and the PV can be a very challenging anatomy, due to their varied shapes and sizes. The orientation of the sheath and the proximity of the MVA can result in the catheter ablation electrode laying on its side against the tissue. (Figure 4.3B) This orientation limits the amount of force that can be placed on the tissue by the ablation catheter as the catheter will slide along the tissue as more contact force is placed against it. Also, as the catheter tip is moved over the ridge, the tip can lose contact, on the ridge, making it a challenge to ablate all the tissue on both sides of the ridge. (Figure 4.3A)

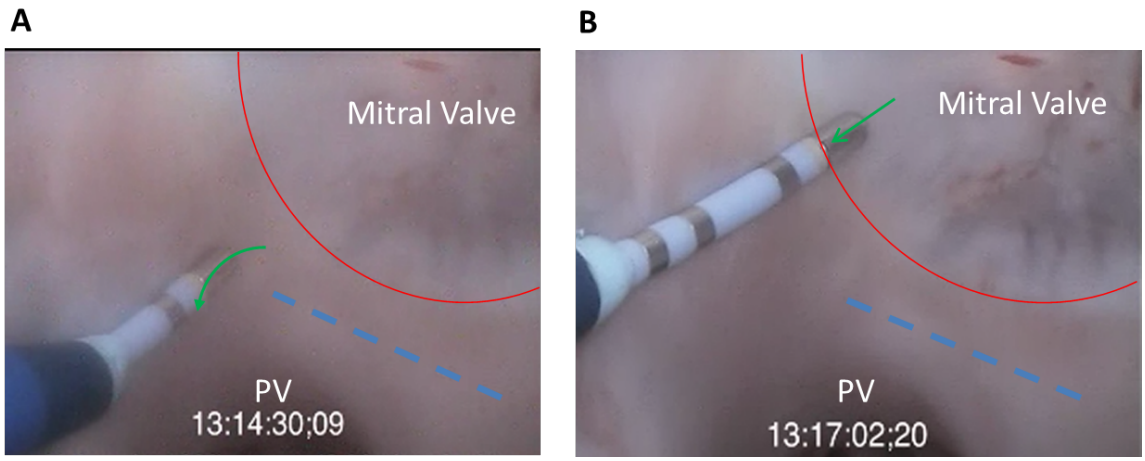

Figure 4.3: Shown is the movement of the catheter using a traditional approach A) catheter tip movement (green arrow) over the ridge (blue dash) B) catheter tip drag (green arrow) starting a MI in the direction of the ridge (blue dash).

This is considered to contribute to an often inability to maintain tissue contact that is sufficient to generate transmural lesions. (see supplemental video – Appendix B) In addition, the relative location of the MI relative to the FO prevents the delivery of a long section of steerable sheaths and/or catheters into the LA: i.e., often reducing the relative amount of contact the catheter shaft can have on the MI. It has been noted that innovative approaches are often needed that allow for better forces to be transferred from the ablation catheter tip along endocardial tissue: such capabilities would in turn allow for greater contact forces resulting in more consistent transmural lesion. This present study utilized Visible Heart methodologies as a novel means to observe the device-tissue interface during the combined approach of catheters and sheaths to augment ablation outcomes, these insights may help clinicians in their desire to enhance clinical outcomes

for transmural MI lesion generations.

Conclusion

The unique in vitro imaging employed here of reanimated hearts, aided to better understand the challenges of catheter navigation as it relates to movement, placement, orientation, and stability within the left atrium during MI ablation procedures. This direct visualizations approach was useful to explore additional variables such as catheter tip angles, power delivery, and ablation durations as a means to modify clinical approaches to achieve appropriate catheter placements for ultimately eliciting proper lesion formations.

Appendix A

Supplementary data

RF - Mitral isthmus - human.wmv

Appendix B

Supplementary data

RF - traditional approach.wmv

Key teaching points

- Support provided by secondary diagnostic catheters may aid to increase the stability of the ablation tip of therapeutic catheter, which in turn will result in improved endocardial contact and a transmural linear lesion of the MI.
- The creation of the linear lesion requires the movement of the various parts of the employed system: including the ablation catheter, support catheters, and/or transseptal sheath.
- In some human anatomies, the therapeutic catheter and/or the delivery sheath may require a degree of retraction into the RA, i.e., in order to maintain contact on the MI as the ablation tip approaches the relative location of the transseptal puncture.

5. Anatomic influences on catheter ablation effectiveness: creation of mitral isthmus linear lesions in human heart specimens from patients with atrial fibrillation

Mark A. Benscoter, MS[1,2]; Julianne H. Spencer, PhD[1,2,3]; Ryan P. Goff, PhD[1,2]; Stephen A. Howard, PhD[3]; Paul A. Iaizzo[2], PhD

[1] Department of Biomedical Engineering, University of Minnesota, Minneapolis, MN

[2] Department of Surgery, University of Minnesota, Minneapolis, MN

[3]Medtronic, Inc., Mounds View, MN

Corresponding author:
Dr. Paul Iaizzo
iaizz001@umn.edu
University of Minnesota
B172 Mayo, MMC 195
420 Delaware Street S.E.
Minneapolis, MN 55455
Telephone: (612) 625-9965
Fax: (612) 624-2002

Brief Title: Variations in mitral isthmus human heart anatomy

Relationship with Industry: Research contract with Medtronic, Inc.

Preface

This chapter is inspired from the learnings of the previous chapter and the first chapter. Atrial fibrillation (AF) is an arrhythmia where the atrial chambers of the heart contract chaotically and inefficiently. One method of treating AF is to ablate areas within the heart that are causing the irregular stimulation. Ablation can be performed with various types of energy. Currently, radio-frequency is the most common energy.

The mitral isthmus is an anatomy of the left atrium that is commonly targeted during ablation therapy. The mitral isthmus is roughly characterized by a line from the left inferior pulmonary vein down to the mitral valve and can be ablated via a catheter in the coronary sinus. Therefore, an understanding of the relative anatomies of the coronary sinus and mitral isthmus is useful for the design of coronary sinus ablation catheters.

The motivation of this study is to characterize the coronary sinus relevant to mitral isthmus ablation. Specifically, we assessed the coronary sinus ostium anatomy, the distance along the coronary sinus from the ostium to the mitral isthmus, and the anatomy of the coronary sinus at the mitral isthmus. We have compared these parameters between specimens with a history of atrial fibrillation and specimens with no history of cardiac disease. We assessed these parameters using magnetic resonance (MR) 101 imaging of 30 perfusion fixed hearts (15 with atrial fibrillation and 12 control). The MR imaging method was consistent with the previous study. The results of this work include intellectual property creation that is owned by Medtronic.

This study was a group effort with myself, Julianne Spencer, Ryan Goff, and Steve

Howard. As a group, we decided on the parameters to be measured that would provide the most useful information in the development of coronary sinus ablation catheters. Julianne was responsible for the imaging of the specimens, the development of the measurement protocol using Mimics reconstruction software, and a portion of the data and statistical analysis. Steve Howard contributed his atrial fibrillation knowledge by assisting us in locating the mitral isthmus and general feedback throughout the project. Ryan Goff also provided helpful feedback throughout the duration of the project. I was responsible for the study design, compilation of the manuscript, and a portion of the data analysis. Cassandra Sundaram and Maria Seewald assisted in the collection of data measurements from the MR scans. This work is part of a completed manuscript submission to a Journal of Arrythmia.

Summary

Background:

Linear ablation of the mitral isthmus (MI) of the left atrium (LA) is a common procedure for patients suffering from atrial fibrillation (AF). Yet, detailed assessments of dimensional anatomic data that might influence the application of ablation therapy are seldom reported. In this study, we assessed variations in cardiac anatomy (the tissue thickness, the presence of fat, and other dimensional data) that might correlate with the effects of catheter ablations.

Methods:

In our laboratory, 30 donated human hearts underwent perfusion fixation and subsequent magnetic resonance imaging (MRI). Through this novel means, we aimed to perform detailed assessments of the coronary sinus (CS) and the MI—both of which are common target sites for catheter ablations in the treatment of AF. We divided the heart specimens into 2 groups: non-AF, from donors *without* AF (mean age, 52 ± 19 years) and AF, from donors *with* AF (mean age, 72 ± 11 years). We focused on CS vasculature anatomy and MI morphology adjacent to the CS.

Results:

On average, the distances along the coronary sinus to the CS mitral isthmus plane were 50.4 ± 14.1 mm in the non-AF group and 66.8 ± 14.6 mm in the AF group ($P < 0.01$). The CS vasculatures were 3.4 ± 1.3 mm away from the LA MI in the non-AF group and 5.6 ± 2.0 mm away in the AF group ($P < 0.01$). The CS ostial circumferences were 31.2 ± 10.7 mm in the non-AF group and 35.2 ± 15.3 mm in the AF group ($P = 0.63$). The CS circumferences at positions of the MI were 21.3 ± 7.8 mm in the non-AF group and 18.1

± 4.1 mm in the AF group ($P = 0.09$).

Conclusions:

Our study of perfusion-fixed human heart specimens helped identify unique anatomic variations that might influence application of radiofrequency (RF) ablation energies for transmural lesions. We found that elicitation of fat adjacent to the CS, reduction in the relative size of the CS, and increased distance from the CS to the LA endocardial surfaces in the MI planes might all contribute to the possibility, after treatment, of incomplete transmural lesions, thereby preventing complete MI conduction block.

Keywords: Atrial fibrillation, catheter ablation, magnetic resonance imaging, mitral isthmus, coronary sinus

Abbreviation List: AF = atrial fibrillation, CS = coronary sinus, LA = left atrium, MI = mitral isthmus, MRI = magnetic resonance imaging

Introduction

The application of ablation therapy within the coronary sinus (CS) and the mitral isthmus (MI) of the left atrium (LA) has been shown to effectively treat persistent atrial fibrillation (AF) [99]. The creation of a linear lesion at the MI is a common practice—and a challenge to complete while attempting to achieve electrical isolation [100,101]. Ineffective ablation applications within this region have been reported to be pro-arrhythmic [102]. When properly performed, ablations of the CS and MI are able to create a linear set of lesions that terminate conduction pathways in patients with persistent AF [103,104,105,106].

In order to carry out effective ablation therapy within the CS and MI, physicians must be able to navigate through a highly variable region of cardiac anatomy [100,107,108]. Wong et al. [102] characterized the regional anatomy (Figure 5.1). The creation of a lesion is based on the catheter tip placement from within the CS and is affected by the distance from the CS to the MI, the CS circumference, the tissue thickness, and the presence of fat in the region of the MI.

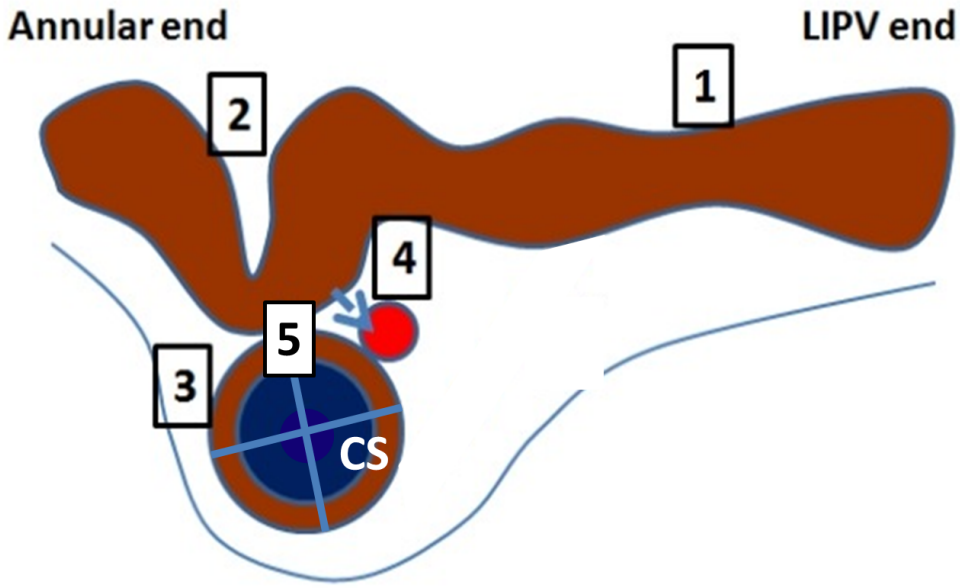

Figure 5.1: Schematic diagram of the cross-section along the mitral isthmus (MI) from the mitral valve annulus to the left inferior pulmonary vein (LIPV). The blue vessel represents the coronary sinus (CS); the red vessel, the left circumflex artery. 1 indicates the long and thick MI; 2, the recess/pouch/crevice; 3, the muscular sleeve around the CS; 4, convective cooling by blood flow in the CS and the artery; 5, the 0° position of the CS circumference.

A detailed understanding of the anatomic structures of the CS and MI, and their relationships to the adjoining anatomy, is critical [100, 101]. Previous studies have used computed tomography (CT) images to characterize the morphology and anatomy in this region during the course of ablation therapy [99,102]. Several of them additionally investigated the endocardial surface shape of the MI; however, they did not characterize the anatomy at the plane of the MI from within the CS to the MI [100, 102]. Some recent studies suggested that older patients (ages 68 to 93 years) might not undergo any age-

based LA size change [103]. The specimens in our study encompassed a broad age range, so we were able to distinguish changes in anatomy based on the presence or absence of AF.

The use of catheters in both the CS and along the MI contributes to the creation of transmural lesions. Previous work has shown that effective catheter orientation can result in lesion depths of 6.3 to 6.5 mm and that lesion depth is negatively affected by poor catheter tip orientation or by low contact force [109, 110]. Therefore, knowing the tissue thickness and composition provides insights that might contribute to the effectiveness of lesion creation.

The purpose of our study was to characterize CS vasculature anatomy, and MI morphology adjacent to the CS, that might affect the ability to effectively use RF ablation catheters when creating transmural lesions. The potential variations in this regional anatomy are clinically important, particularly for patients with persistent AF.

Methods

In our laboratory, 30 donated human hearts underwent perfusion fixation and subsequent magnetic resonance imaging (MRI), with 3-dimensional reconstruction of the MI and CS anatomy to measure the desired anatomy. Through this novel means, we aimed to perform detailed assessments of the CS and the MI—both of which are common target sites for catheter ablations in patients with AF. We divided the heart specimens into 2 groups: the non-AF group (control specimens from donors *without* AF) and the AF group

(specimens from donors *with* AF). We focused on CS vasculature anatomy and MI morphology adjacent to the CS. To determine any significant differences in cardiac anatomy, we conducted a statistical analysis.

MRI with Anatomic Reconstructions and Measurements

The heart specimens were perfusion-fixed with a head pressure of approximately 50 mm Hg with 10% formalin, as previously described [110]. This step allowed the specimens to maintain a pseudo end-diastolic shape and thus remain in a more realistic anatomic form. The specimens were then embedded in a 7% agar solution to decrease MRI artifacts [110]. Scans of the 30 specimens were obtained with a 3T scanner (Magnetom TRIO 3T MRI scanner, Siemens Corp., Munich, Germany), using a magnetization-prepared rapid-acquisition gradient-echo (MP-RAGE) (T1-weighted) protocol with a base resolution of 512. We chose MRI because of its ability to clearly quantify high spatial and temporal resolution measures of cardiovascular structure and to distinguish myocardial tissue from fat [111,112,113].

CS vasculature anatomy

We devised a set of anatomic measurements deemed to affect the ability to use a 7-French ablation catheter. After combining the MRI images to render a 3-dimensional dataset reconstruction, we analyzed it using Mimics Software (Materialise, Leuven, Belgium). The set of CS measurements included CS diameters and circumferences, distances along the CS from its ostium to the MI, and the cross-sectional shape at the MI.

We imported each of the cardiac image sets and combined them into 3-dimensional

reconstructions of the LA and the CS. The LA reconstruction was used to define the CS center line, determined by taking the 2-dimensional cross-section of the CS and finding the center point of the CS (Figure 5.2). The center point was used as an origination reference point to determine degree positions on points of the CS circumference at the MI plane. The MI plane was defined as the shortest distance from the CS center line to the LA endocardial surface

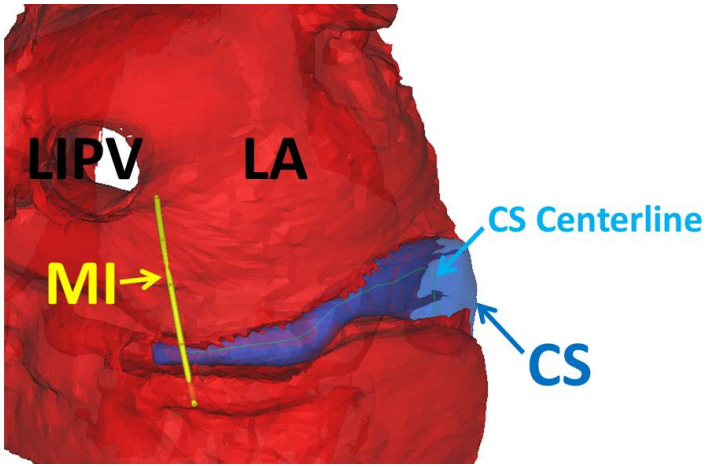

Figure 5.2: Anatomic reconstruction of the left atrium (LA), coronary sinus (CS), and left inferior pulmonary vein (LIPV). The yellow mitral isthmus (MI) plane line intersects the CS center line as measured in the reconstructed 3-dimensional model. The light blue line depicts the CS center line.

inferior to the left inferior pulmonary vein (LIPV) and superior to the mitral valve annulus (Figure 5.2). After determining the MI plane, we re-sliced the scans so that the cross-section of the CS was at the MI plane. In that plane, we assessed the long and short axis diameters, circumferences, and shapes of the CS.

MI morphology

To further analyze MI anatomy affecting catheter usage, we examined the distance to the LA, the presence of fat in the region subject to ablation energy, and the distances at

degree positions on points of the CS circumference. We identified the location of fat by the variation in contrast seen within the MRI images, then verified the location by sectioning the heart into slices (3 to 5 mm thick) after fixation (Figure 5.3). The slices were subjected to MRI, in order to verify

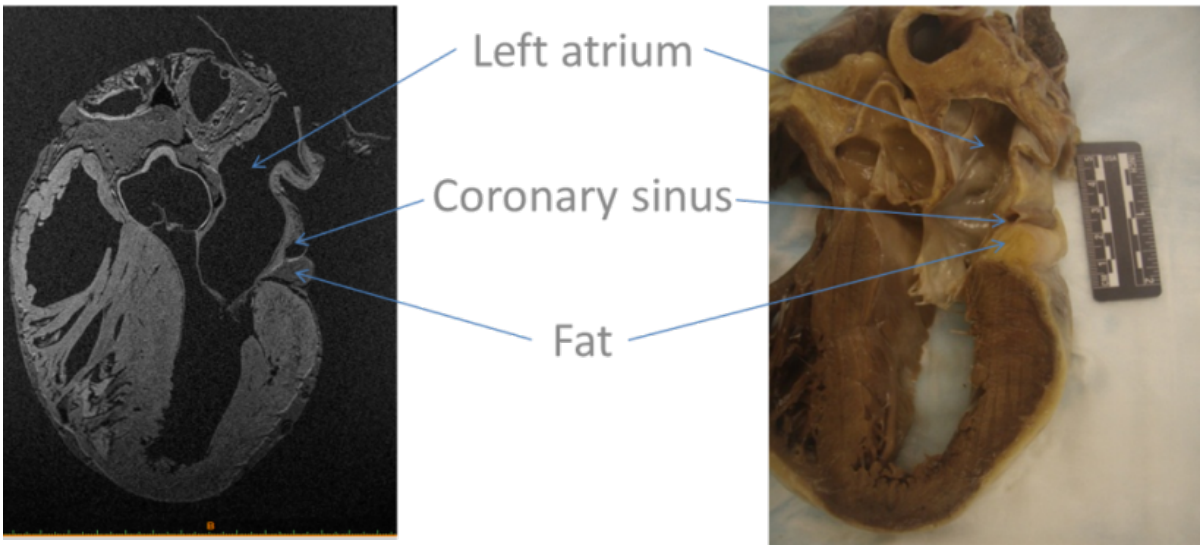

Figure 5.3: A magnetic resonance imaging (MRI) image (left) and a photograph of the same human heart specimen (right). The left atrium (LA) endocardial space is labeled (left atrium). The specimen section includes the coronary sinus (CS); immediately inferior to it is a deposit of fat that is visible on both the MRI image and the photograph.

that the gray scale of the fat around the CS in the initial MRI images correlated to the fat seen on the slices.

Using a 2-dimensional MRI slice at the plane of the intersection of the CS center line and the MI line, we drew a line across the mitral annulus as a reference. Next, we drew a line parallel to the mitral annulus across the center of the CS cross-section and defined that line as 0°. Finally, we created 3 additional lines through the center of the CS cross-

section at 45°, 90°, and 135° to the 0° line (Figure 5.4). We assessed the presence of fat

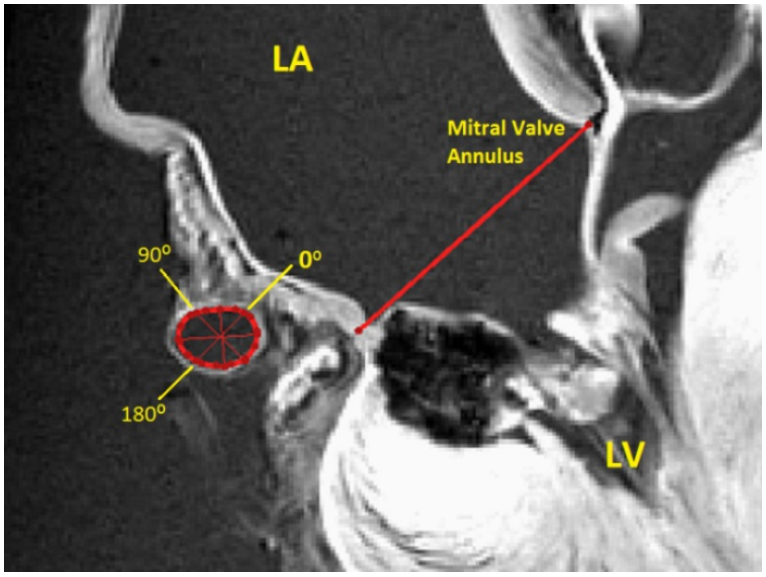

Figure 5.4: Analysis of the coronary sinus (CS) at the mitral isthmus (MI). The 0º to 180º line is parallel to the mitral annulus. Using the CS center line, we created degree positions around the CS (0º, 90º, and 180º), in order to measure distances to the endocardial MI. The left atrium (LA) and left ventricle (LV) are labeled for reference.

between the intersection of those lines with the boundary of the CS and the LA as a binary parameter. Then, we measured the distance from the CS to the LA space at each position around the CS.

Statistical analysis

Data are presented as the mean ± standard deviation. To compare 2 related samples, we used a nonparametric Wilcoxon rank sum test ($\alpha = 0.05$) to determine any statistically significant differences between the AF group and the non-AF group (Table 5.1). The dependent samples are not assumed to be normally distributed, resulting in the use of the Wilcoxon rank sum test. The AF group was older and had a larger male: female ratio, but had similar body weights relative to the non-AF group. We included the non-AF

control group to account for variation introduced by the perfusion fixation process.

Results

Study specimens

The 30 perfusion-fixed human hearts used in our study were considered nonviable for transplantation via both LifeSource (St. Paul, MN) and the bequest donation program at the University of Minnesota (Minneapolis, MN). The AF group included 15 specimens; so did the non-AF control group, which included heart specimens from donors *without* AF or any other clinical cardiac diagnoses (Table 5.1).

Table 5.1: Donor characteristics (n = 30) (mean ± standard deviation)

	Non-AF group (n = 15)	**AF group (n = 15)**	***P* (α = 0.05)**
Age at death (years)	52 ± 19	72 ± 11	0.01*
Gender (male: female)	4:11	9:6	N/A
Weight (kg)	76.8 ± 21.8	81.2 ± 24.8	0.65

* a significant difference ($P < 0.05$)

AF = atrial fibrillation; N/A = not applicable

CS vasculature anatomy

For all 30 heart specimens, we assessed CS anatomy against anatomic dimensions that might affect the ability to deliver and use a focal ablation catheter. CS ostial plane measurements of circumference, long axis, and short axis (35.2+-15.3 mm, 12.3 +-6.9 mm, and 7.3+-3.0 mm) were not significantly different, P>.05 between the 2 groups. Nor were 2 of the CS measurements at the MI plane: CS circumference and CS short axis; however (18.1+-4.1 mm, 4.5+-1.4 mm) were not significantly different (P=.09 and .97) . However, CS long axis (6.4+-1.7 mm) was significantly different (P=.03) when

compared against non-AF hearts. (Table #5.2)

Table 5.2: CS anatomic measurements, mm (n = 30)

	Non-AF group (n = 15)	**AF group (n = 15)**	***P* (α = 0.05)**
CS ostial plane			
CS circumference	31.2 ± 10.7	35.2 ± 15.3	0.63
CS long axis	11.2 ± 4.1	12.3 ± 6.9	0.92
CS short axis	6.8 ± 2.6	7.3 ± 3.0	0.69
CS at MI plane			
CS circumference	21.3 ± 7.8	18.1 ± 4.1	0.09
CS long axis	8.1 ± 3.1	6.4 ± 1.7	0.03*
CS short axis	4.7 ± 2.0	4.5 ± 1.4	0.97

* a significant difference ($P < 0.05$)

AF = atrial fibrillation; CS = coronary sinus; LA = left atrium; MI = mitral isthmus

Per CS measurements at the MI plane, CS circumference decreased by 48.5% in the AF group and by 31.8% in the non-AF group. Note that a traditional ablation catheter has a diameter of 2.33 mm (7-French). In the AF group, the higher reduction in circumference, along with the smaller CS long axis and smaller CS short axis, reduced the ability to apply deflection at the catheter tip. Hence, in the AF group, the ability to achieve contact with the wall of the CS was impaired. In addition, the size of the CS continued to be larger than the catheter, resulting in intermittent contact in the CS at the MI plane.

MI morphology

The distance from the ostium to the MI plane along the CS in AF and non-AF patients (66.88+-14.6 mm, 50.4+-14.1 mm) were significantly different, p=.01. (Table 5.3). So did the distance from the CS to the LA at the MI plane.

Table 5.3: MI anatomic measurements, mm (n = 30)

	Non-AF group (n = 15)	**AF group (n = 15)**	***P* (α = 0.05)**
Distance from ostium to MI plane along CS	50.4 ± 14.1	66.8 ± 14.6	< 0.01*
CS at MI plane			
Distance from CS to LA at MI plane	3.4 ± 1.3	5.6 ±2.0	< 0.01*

* a significant difference ($P < 0.05$)

AF = atrial fibrillation; CS = coronary sinus; LA = left atrium; MI = mitral isthmus

In the AF group, the overall presence of fat was higher at every point of the CS circumference *except* the 270° position; the difference was significant at the 90° position ($P = 0.03$) and the 315° position ($P = 0.01$).

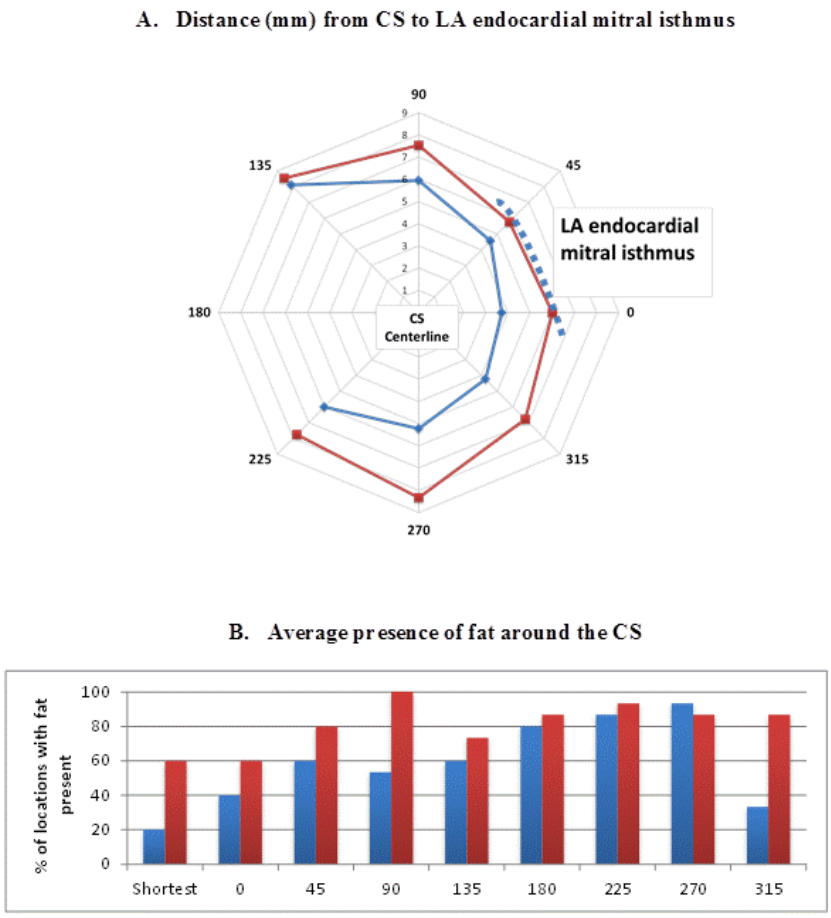

Figure 5.5: Presence of fat and distance to mitral isthmus (MI) at the position of the coronary sinus (CS) at the MI plane, in degrees around the CS: red, atrial fibrillation (AF) group; blue, non-AF group. (A) Distance around the CS at the MI plane to the left atrium (LA) space, in mm. (B) Bar chart comparing the percentage of hearts where fat was present, next to different positions on the CS. The shortest label (–) compares the 0° AF position with the shortest (15°) non-AF position.

The smallest percentage of fat in the AF group was at the 0° position; the shortest

distance to the LA in the AF group was at the 0° and 45° positions (Figure 5.5).

In total, we observed fat in 79 (59%) of 135 positions in the non-AF group and in 109

(81%) of 135 positions in the AF group (data not shown). Moreover, the average distance from the CS to the LA space was greater in the AF group at every position assessed around the CS. The differences between the 2 groups were significant at 2 positions: 0° ($P < 0.01$) and 315° ($P = 0.02$).

Discussion

Major findings

According to our study of 30 heart specimens, CS anatomy, MI morphology, and minor position differences on the circumference of the CS at the MI plane might all influence the effectiveness of catheter ablation therapy—specifically, the ability to achieve good contact with the desired tip placement, resulting in transmural lesions. Given the inherent limitations in the penetration of a lesion, anatomic changes and differences might limit the ability to create transmural lesions.

CS vasculature anatomy

We found that CS circumference at the MI plane exceeded that of a traditional ablation electrode. In addition, CS circumference was not large enough to allow the catheter tip to be placed perpendicular to the tissue. In the region of the MI, the CS short axis diameter (4.7 ± 2.0 mm) in the AF group was larger than the commonly available 7-French (2.3 mm) ablation catheter tip. This constraint resulted in the catheter tip lying against the wall of the CS or in a slight amount of deflection at the tip: in either situation, the amount of contact force that can be placed on the catheter tip was low. Wong et al. [101] found that when CS diameters at the MI were larger than the catheter tip, the catheter tip needed to be manipulated many times in order to achieve tissue contact. The relatively large

average diameter in our study (short axis: 4.7 ± 2.0 mm in the AF group) suggests that, in human patients, placing the catheter tip on the desired tissue and thus achieving successful ablation will be challenging. This inability to achieve sufficient contact might be a primary reason for the low success rates, clinically, in the creation of transmural lesions.

MI morphology

From the perspective of the tip of the ablation catheter, we found that MI morphology, along with adjacent anatomic changes with the onset of AF, complicated the ability to create transmural lesions.

In the AF group, the shortest distance to the MI was at the 45° position (5.8 ± 2.0 mm). However, at the 0° position, we observed the lowest percentage of fat (60%), as well as the second shortest distance (6.0 ± 2.0 mm) to the endocardial MI. Moving 45° in an inferior direction to the 315° position, we saw an increase in the distance to the LA and a higher percentage of fat. Thus, catheter tip placement between the 0° and 45° position might be more desirable than between the 0° and 315° position. Using the anatomical measurements from this study along with additional studies that examine both the 45 and 315 degree position to quantify the amount of fat present would aid in refining the ablation produce to achieve a transmural lesion.

At every degree position around the CS, the distance between the CS and the LA space was longer in the AF group than in the non-AF group.

Previous work by Yokokawa et al. [99] demonstrated that changes in the ablation settings might be required to achieve transmural lesions. They examined characteristics of the

anatomy in this same anatomic region that we did, focusing on the orientation of the circumflex artery, the curvature of the MI, and additional CS measurements at the MI. They, too, found that effective catheter placement was critical in the creation of transmural lesions and pinpointed anatomic elements that can contribute to ineffective catheter usage. Our study further refines their conclusions by suggesting that the preferred anatomic positions for catheter tip placement are at the 45°, 0°, and then 315° position at the plane of the MI within the CS. At the 90° and 270° position, we documented a sharp increase in both the distance to the LA and the presence of fat. In addition, the tissue thickness increased between the CS and the LA in the region of the MI in the AF group (3.4±1.31mm for non-AF hearts versus 5.6 ± 1.97 mm for AF hearts).

Clearly, our findings reinforce the need for modifications to ablation settings.
The changes in anatomy that we observed between non-AF and AF hearts, along with the changes in MI morphology, all support the notion that ablation durations and settings need to be modified, in order to result in transmural lesions. The use of traditional anatomic landmarks around the MI aids in positioning ablation catheter tips within the CS, but might be insufficient for achieving effective lesions necessary for electrical isolation [100].

We also found that defining the CS center line facilitated the ability to find the MI plane within the CS that is the shortest distance. Using the CS center line as a reference, we

were able to obtain measurements that affected creation of transmural lesions. The presence of fat in the region of the MI plane, along with changes in distance from the CS to the MI, might contribute to less than ideal creation of lesions.

Study limitations

Our study was limited by the effects of the perfusion fixation process that can result in an approximate 10% reduction in overall heart size. Our non-AF control group was used to account for changes introduced through the fixation process, but fresh specimens would have removed the need for a control group.

Conclusions

Transmural lesion creation is affected by catheter contact force and lesion depth. CS vasculature anatomy and MI morphology in the region of the LA might contribute to limiting the effectiveness of RF ablation aimed at creation of transmural lesions. The slightly longer CS distances in the AF group suggest that LA volumes are predictably larger [100,102].

In addition, the presence of fat adjacent to the CS might prevent creation of effective linear lesions. The clear differences in the tissue thickness of the MI in the AF group show that variation in the tissue thickness might be beyond the penetration depth of a lesion. An effective path for a transmural lesion might be achieved by orienting a catheter tip that is not in the plane of the mitral annulus away from that plane, at about a 45° angle, from within the CS.

Finally, CS circumferences indicate that the ability to affix a catheter in the distal areas of the CS might require specific manipulations to ensure that the catheter tip is in contact with atrial tissue. The ability to apply greater contact force at the catheter tip allows for more precise tip placement and improved lesion creation. This ability would be an improvement to catheter design, increasing the chance of lesion creation on viable tissue and thus improving the efficacy of linear ablation of the MI.

Conducting these measurements in the CS at the MI plane reveals the shortest path to create a lesion, as well as the anatomic limits of lesion penetration.

6. In vivo catheter contact force and correlation with monophasic action potentials in epicardial and endocardial anatomic locations

Mark A. Benscoter, MS, [1, 3] Megan M. Schmidt, [1] Tinen Iles, [2] Paul A. Iaizzo, PhD[1, 2]

[1] Department of Biomedical Engineering, University of Minnesota (Minneapolis, MN)

[2] Department of Surgery, University of Minnesota (Minneapolis, MN)

[3] Department of Engineering, Mayo Clinic (Rochester, MN)

Corresponding author:
Dr. Paul Iaizzo
iaizz001@umn.edu
University of Minnesota
B172 Mayo, MMC 195
420 Delaware Street S.E.
Minneapolis, MN 55455
Telephone: (612) 625-9965
Fax: (612) 624-2002

Brief Title: Understanding contact force required to collect MAPs

Relationship with Industry: Research contract with Medtronic, Inc.

Preface

The inspiration for this study arose from the development of a catheter device used for the collection of monophasic action potentials and the observed limitations to control catheter placement as observed in chapters 1 and 4. Monophasic action potentials (MAP) have been demonstrated as a method to depict cardiac depolarization that is able to be collected through the use of an intracardiac catheter. These signals can be collected when physical pressure is placed against the tissue causing the waveform to pass underneath the catheter tip as the tissue depolarizes. Recently, research has shown the ability to collect MAPs. However, there have been limitations in that it is unknown what is the appropriate amount of pressure to apply to the tissue the generate MAPs. Insufficient and excessive pressure both result in no MAP signal. Recent studies using contact force in the creation of radiofrequency lesions have demonstrated that insufficient pressure results in a poor lesion and excessive pressure results in risk of cardiac tamponade.

The ability to understand the contact force to generate a MAP would show what the necessary pressure is to collect a MAP and prove the ability to show if the tissue at the tip of a catheter is electrically viable. Future studies in this area could bring together the contact force for both ablation and MAPs as a way to help direct ablation therapy to the areas that are electric ally conductive at the tip of the catheter. The key to be able to accomplish this is to know if there is sufficient pressure at the location of interest that should result in the ability to collect a MAP.

For this study, I was responsible for making the devices, calibration, study design, conducting the data collection, data analysis, and publication creation. A biomedical

engineering student, Megan Schmidt, and staff scientist, Tinen Iles, assisted in the majority of data collection and data analysis. The contents of this chapter were submitted as a manuscript to the Journal of Cardiovascular Electrophysiology.

Summary

Background:

In this study of catheter use in swine hearts, our objective was to examine in vivo contact force (CF) and its possible correlation with epicardial or endocardial cardiac monophasic action potentials (MAPs).

Methods:

MAPs were generated from swine hearts both in situ (after a medial sternotomy) and in vitro from hearts reanimated using Visible Heart® methodologies.

Results:

We collected and analyzed a total of 99 endocardial points and 380 epicardial points. At each site, for all points, we determined the mean CF and the CF standard deviation (SD). The mean CF required to generate MAPs for all 9 pigs was 9.54 ± 2.43 grams. The mean CF widely varied among hearts. Of note, the mean CF for 2 of the hearts (11.47 grams) was significantly higher than for all of the other hearts (5.05 grams) ($P < 0.0001$).

Conclusion:

In this study of catheter use in swine hearts, we successfully showed the relative CF required to generate MAPs in various regional anatomies, both epicardially and endocardially. The mean CF required to generate MAPs was different across locations in/on the heart and varied from heart to heart.

Keywords: Atrial fibrillation, catheter ablation, mitral isthmus, coronary sinus

Abbreviation List

AF = atrial fibrillation, CF = contact force, CS = coronary sinus, ECG = electrocardiography, EOR = end of repolarization, LA = left atrium, LV = left ventricle, MAPs = monophasic action potentials, MI = mitral isthmus, OF = outflow tract, PV = pulmonary vein, RA = right atrium, RF = radiofrequency, RV = right ventricle, SD = standard deviation, TAPs = transmembrane action potentials

Introduction

Clinically, focal signals of monophasic action potentials (MAPs) are collected when localized cardiac excitation repolarizations are desired; a reason is to supplement the data obtained from complex fractionated atrial electrograms. These MAPs can indicate what is occurring electrically in regional anatomies in situations when conventional bipolar or unipolar electrograms are unable to accurately do so. In the past several decades, devices have been developed to collect MAPs in real time, but with varying degrees of success. Furthermore, generating MAPs requires an applied contact force (CF) of the catheter onto the heart to depolarize the tissue. The limited success of these devices might be linked to an inappropriate amount of CF with the tissue. Additionally, anatomic location might affect the amount of CF required to generate MAPs.

Specifically, MAPs are recorded waveforms or signals that focally characterize electrical excitations (depolarizations and repolarizations) of the myocardium. Synchronized to cardiac function, MAPs are able to show localized signals describing activation timing, density, pattern, and velocity. Today, it is common to use gross electrograms that depict electrical potentials across larger regional anatomies; however, electrograms are often convoluted and distorted by far-field signals and double counting.[114,115,116,117] The use of MAPs allows for a more physiological focused study of cardiac substrate by collecting very localized repolarization activity. [118,119] Recording their high-fidelity signals enables clinicians to classify activation of tissue regions and to then use that information for subsequent ablation decisions, instead of relying on broad-based and incomplete

electrogram data. [120]

The use of MAPs to direct the care of human patients and to better understand their cardiac function has been reported in studies exploring transmembrane action potentials (TAPs), atrial flutter, and ablation therapy for patients with atrial flutter. In 1986, Franz and Burkhoff et al. [121] conducted pioneering experimental research on MAP recordings, using novel devices. In perfused rabbit septum preparations, they recorded contact-electrode MAPs simultaneously with TAPs; then, they quantitatively compared those 2 signals for duration and area at 30%, 60%, and 90% repolarization. Their data indicated that using novel devices to collect MAPs helped accurately measure the repolarization time course of TAPs.

In 2009, in a porcine model, Aidonidis and Poyatzi [122] hypothesized that the patterns of local repolarization in the high and low right atrium (RA) would allow determination of the site with pronounced propensity to map disorganization during atrial flutter and atrial fibrillation (AF). They used focal catheters that were capable of continuously generating MAPs. The high atrial MAPs revealed discordant repolarization during atrial flutter or AF, whereas the low atrial MAPs maintained their baseline regular morphology. In their study, the focal catheter was used only in the RA. Subsequently, other investigators began using such catheters within the left atrium (LA) where AF rotors are most often described. [120,121,122,123]

Thus, in human patients, generating MAPs is considered a useful means to precisely depict the localized depolarizations and repolarizations of clusters of myocardial cells

[124,125]. In addition, other investigators have shown the utility of swine studies for observing and better identifying MAPs.[126,127] Clinically, gathering these signals might be the best way to identify the substrates on which AF patterns form or are sustained. [128,129] Early identification and treatment of such sites may aid in understanding the emergence of AF.

The need to apply a degree of physical pressure (i.e., CF) to generate MAPs raises this key question: Just how much CF is required, using a typical catheter, and should it vary relative to the anatomic site in/on the heart? [119,121] Studies similar to ours have looked at CF as it relates to the application of cardiac mapping and ablation. [130,131,132] In our study, in order to address any correlation of CF with MAPs, we employed several methodologies. First, we collected epicardial MAPs in situ from swine hearts after a medial sternotomy and the creation of a pericardial cradle. Second, using previously described Visible Heart® methodologies [133,134] to reanimate swine hearts, we generated both epicardial and endocardial MAPs in vitro in various regional anatomies (e.g., the mitral valve annulus, the right ventricle outflow tract [RVOT], and septum). Third, knowing that radiofrequency (RF) ablation has used CF to aid in creating lesions and that a number of studies have quantified the CF required to generate lesions with a range of results [131,136,137], we quantified the CF to generate a MAP. The dual objectives of our study were to (1) determine the amount of CF required to generate MAPs using a catheter-based approach and (2) investigate how the amount of CF required to generate MAPs varies in different anatomic locations.

Methods

Study population

Nine animals were subject to mapping. These studies were performed using Yorkshire Cross pigs that were initially anesthetized with 500 mg of Telazol and 500 mg of methohexital, and then intubated for general anesthesia (maintenance with ~ 1.5% isoflurane, > 2 minimal alveolar concentration). Each pig was continuously monitored using electrocardiographic (ECG) recordings as well as left and right ventricular pressure measurements. Our study was reviewed and approved in accordance with the University of Minnesota Animal Care and Use Committee.

Mapping procedure

All pigs underwent either epicardial or endocardial mapping. We collected simultaneous CF and MAP epicardial signals from the RV and left ventricle (LV) apex, from 5 locations on the RV septum, and from the RVOT (Figure 6.1). Endocardial locations included the RVOT, RV anterior free wall, RV apex, RV septum, Right atrial appendage (RAA) opening, tricuspid annulus, coronary sinus (CS) ostium, anterior papillary muscle, and RA superior free wall.

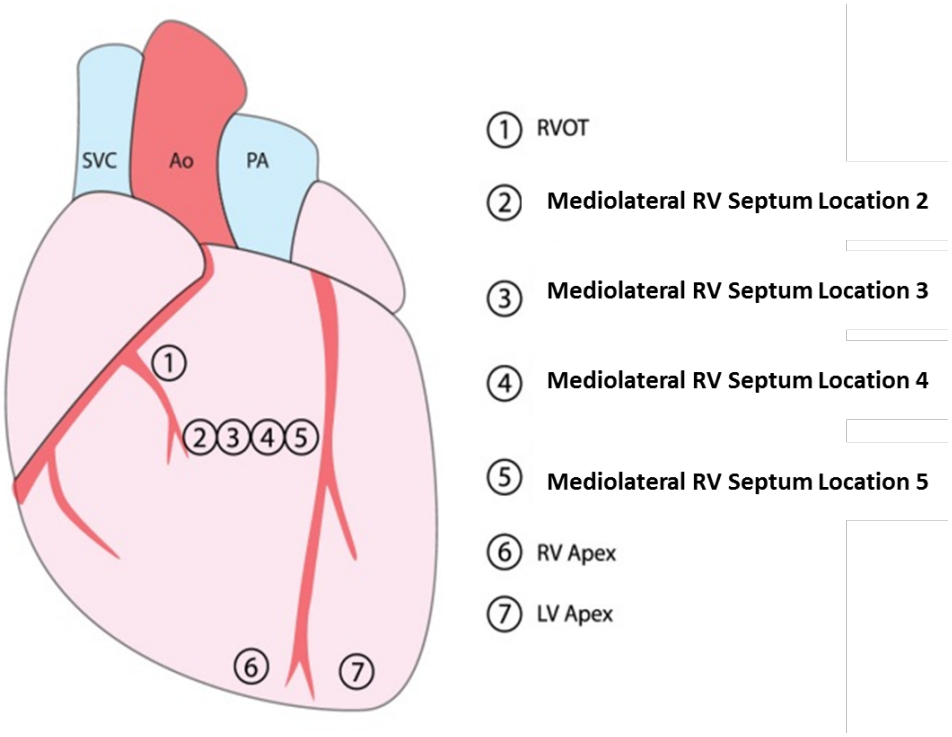

Figure 6.1: Epicardial sites for CF/MAP signals collection. RVOT = right ventricular outflow tract, RV = right ventricle, LV = left ventricle RAA = right atrial appendage, CS = coronary sinus, RA = right atrium

Simultaneously, we collected heart rate from a number of sources, including electrograms, exposed electrodes on the surface of the catheter, and a roving diagnostic ECG catheter.

For epicardial point collection, we performed a medial sternotomy in each pig, and stabilized the heart by forming a pericardial cradle. To collect epicardial MAPs, we placed the catheter (Figure 6.2) in a holding apparatus, thereby allowing for precise control of its tip's placement and orientation against the epicardial surface.

For endocardial point collection, we used a separate set of anatomic locations. After our in situ experiments, we performed a standard cardioplegia procedure, then excised the

heart for our in vitro studies. In the jugular vein of each pig, we placed a 12.5 French introducer to provide endocardial access. To directly visualize the interface between the endocardial device and the tissue, we used Visible Heart® methodologies, as previously described. [133]. We placed the excised porcine heart on the apparatus and reanimated it, using a clear Krebs-Henseleit buffer. Only specimens that elicited normal cardiac function (e.g., a native sinus rhythm) were analyzed.

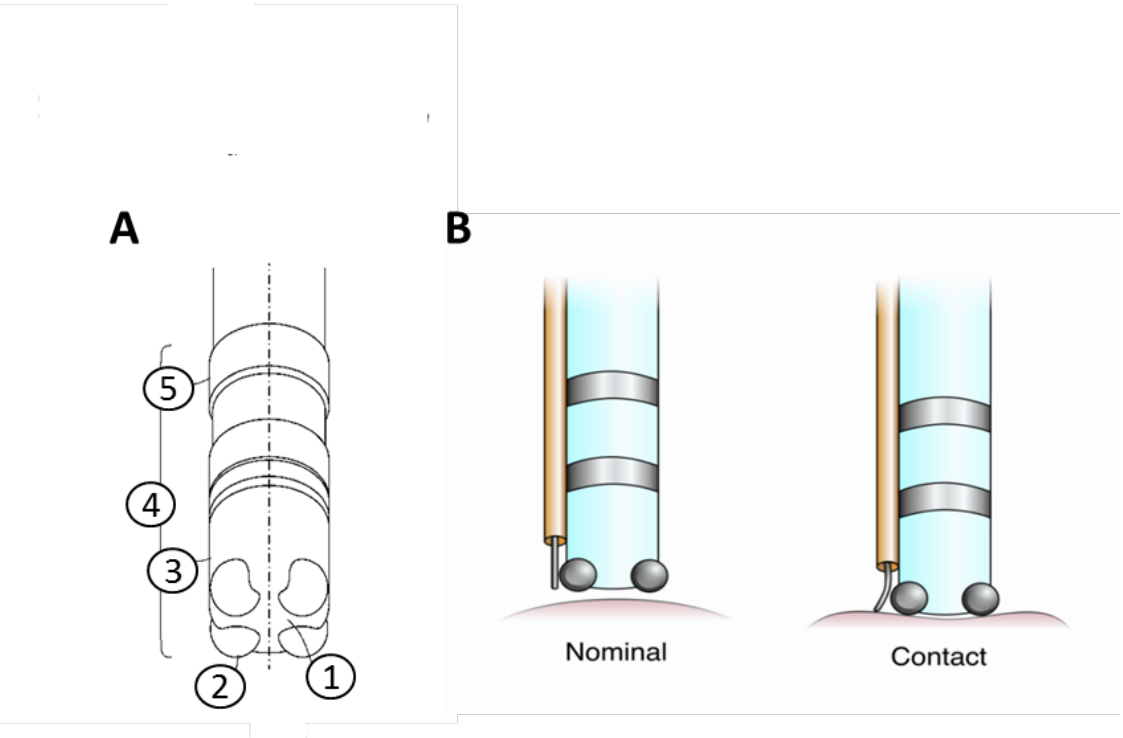

Figure 6.2: (A) Design of the tip of the MAP catheter (4) with 4 distal electrodes (2) and 2 – 2 mm band electrodes (5) that are mounted on the shaft of the catheter. The tip electrodes are isolated from each other using a polymer (1, 3); the catheter is able to collect both unipolar and bipolar signals. (B) Illustrates the catheter tip as it engages the tissue surface. The electrodes and fiber Bragg grating strain sensor (orange tube) come in contact with the tissue at the same time. Contact is denoted by deformation of the fiber grating in the right panel of (B). This deformation is translated into grams of CF. CF = contact force, MAP = monophasic action potential

Depolarization was defined by the maximal slope of the upstroke of the MAP recording. Local end of repolarization (EOR) was defined as the intersection between the baseline and the tangent to the steepest slope on phase 3 of the MAP (Figure 6.3).

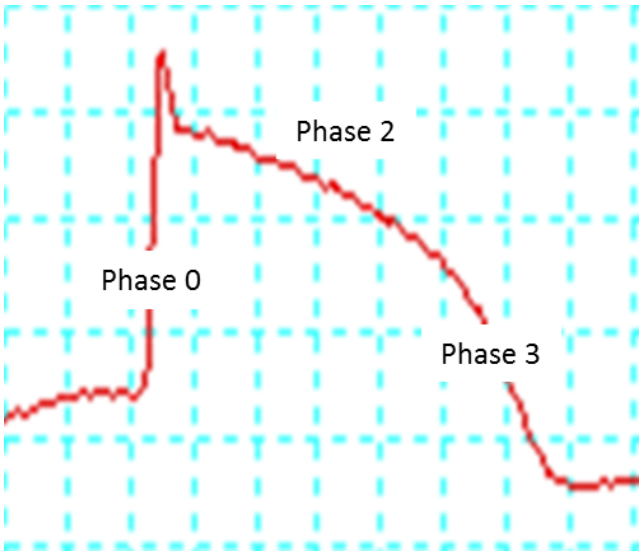

Figure 6.3: MAP depolarization and repolarization. During phase 0 (depolarization), sodium enters the cell; during phase 2, calcium enters the cell and contraction starts; during phase 3 (repolarization), potassium exits the cell. MAP = monophasic action potential

We used comparative beat-to-beat measurements in case of MAP distortions or any disturbance to the baseline due to respiratory or cardiac contractions. Activation time (AT) was defined as the time interval from the earliest recorded ventricular activation to local activation, the; EOR time, as the time interval from the earliest ventricular activation to local EOR; and MAP duration, (MAPDUR) as the time interval from local activation to local EOR. (Figure 6.4A) Values were obtained at each site, taking the peaks of a QRS complexes time references. (Figure 6.4B)To account for affect associated with respiration and cardiac movement, we measured the CF for a MAP after observing a

series of 4 consecutive MAPs.

To amplify and digitally record all MAP signals from each electrode, we used a computer-based laboratory system (PowerLab, ADInstruments, Colorado Springs, CO). Each MAP signal was recorded in a bipolar configuration, i.e., between tip electrodes and a 2-mm ring electrode. We also obtained a unipolar electrogram, with a filter bandwidth of 0.1 to 120 Hz. Increasing force was applied to the location until the first MAP signal was generated. (Figure 6.4C) We used the CF at the time of the last set of 4 consecutive MAP signals to examine any affect associated with tissue deformation due to sustained force from catheter placement. Additionally, for those anatomies that were affected by respiration, we implemented a momentary breath hold for a period of 10 to 30 seconds, in order to reduce the impact of any effects associated with respiration; on completion of a breath hold, the pig was allowed time to recover and to resume natural respiration.

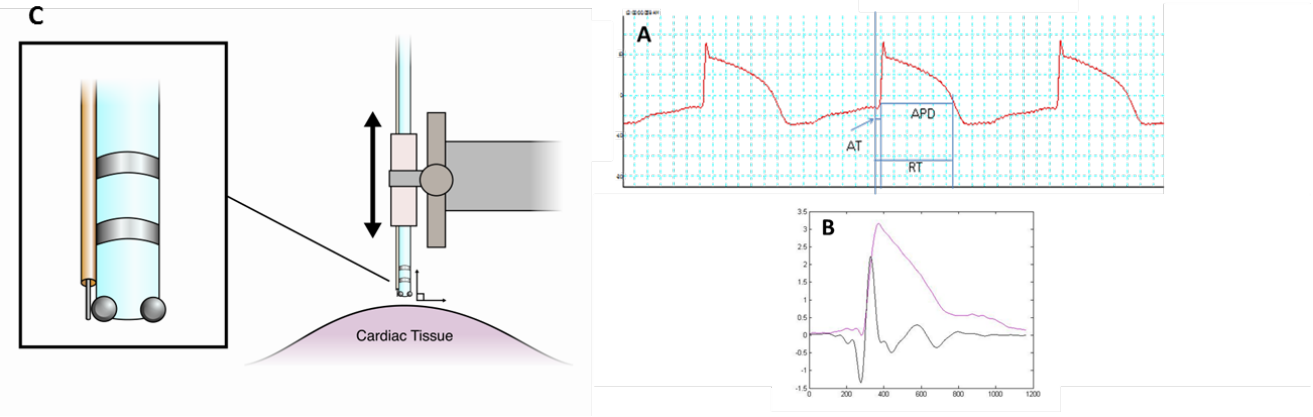

Figure 6.4: (A) Signals that served to define AT, APD, and RT. (B) A single MAP (purple) and ECG (black) signal captured on the RV epicardium. (C)

Catheter orientation, direction of motion, and orientation for epicardial measurements. APD = action potential duration, AT = sum of activation time, ECG = electrocardiography, MAP = monophasic action potential, RT = repolarization time, RV = right ventricle

In addition to collecting MAPs, we placed a 5 French bipolar electrode, either epicardially or endocardially, to simultaneously collect far-field signals.

Contact force measurement

To measure CF, we used a system consisting of a treatment/recording electrode tip with 4 separate conductive mapping electrodes (Figure 6.2A) and an additional lumen that contained a fiber Bragg grating (Figure 6.2B).[135] A diffraction grating, the fiber Bragg grating was built into the optical fiber; it reflected light at a very specific wavelength. The wavelength related to the strain applied to the fiber. An optical interrogator (HBM, Germany) was employed as a "swept wavelength" laser to determine the reflected wavelength, which then represented the relative strain. Each was constructed in short segments of optical fiber with an accuracy of ± 1 nm. Strain was assumed with Bragg displacement in relation to a reference length, and was transformed into a normalized measure of deformation, i.e., the relative amount of strain that was generated was computed as a general deformation. Each fiber Bragg grating strain sensor was calibrated before the start of data collection. The tip of the fiber had a measureable force (grams) placed against it. The force was incrementally increased and at each increment the frequency and force were collected. This resulted in a frequency to force relationship that was used to derive a linear expression that was the calibration curve. This calibration process enabled each unique piece of fiber to be normalized to grams.

Statistical analysis

Each experiment included basic statistical analyses including randomized samplings of the variables along with *t* tests to determine any significant differences between means. Because we took multiple measurements from a single specimen, we used Levene's test to assess the equality of the variation across all specimens. A significance level of 0.05 was used for global test statistics and for Levene's test. To examine the influence of change in variation, we normalized the CF data using the epicardial mediolateral RV as a reference point. For all statistical analyses, we used Minitab version 12. We conducted a power analysis between MAP generation and CF, as compared with the observed CF used for generation of ablation lesions, in order to assess the number of observations that would be required to find a significant difference between those CFs.

Results

Our study's results demonstrate that contact alone is not enough to generate MAPs; rather, a certain threshold of force must first be achieved. Because of that activation threshold, investigators have been unable to discern, at least with current catheter-based methods of collecting data on MAPs, whether or not the contact force from the catheter was sufficient for generating MAPs. But with the device method we used in our study, we were able to demonstrate, for the first time, the amount of force required to repeatedly generate high-quality MAPs. In addition, we showed that our catheter method was capable of collecting data by placing the tip at slight angles that were not perpendicular, in variable positions, without leading to any significant differences in generating MAPs.

Epicardial and endocardial mapping

Mapping of all endocardial and epicardial sites were performed only on hearts contracting in a normal sinus rhythm. Epicardial MAPs were recorded *in situ* while endocardial MAPs were collected *in vitro* from re-animated swine hearts. We collected and analyzed a total of 99 endocardial points and 380 epicardial points. To maintain consistency among all points, we oriented the catheter to be perpendicular to both the endocardial and epicardial surface (Figure 6.5).

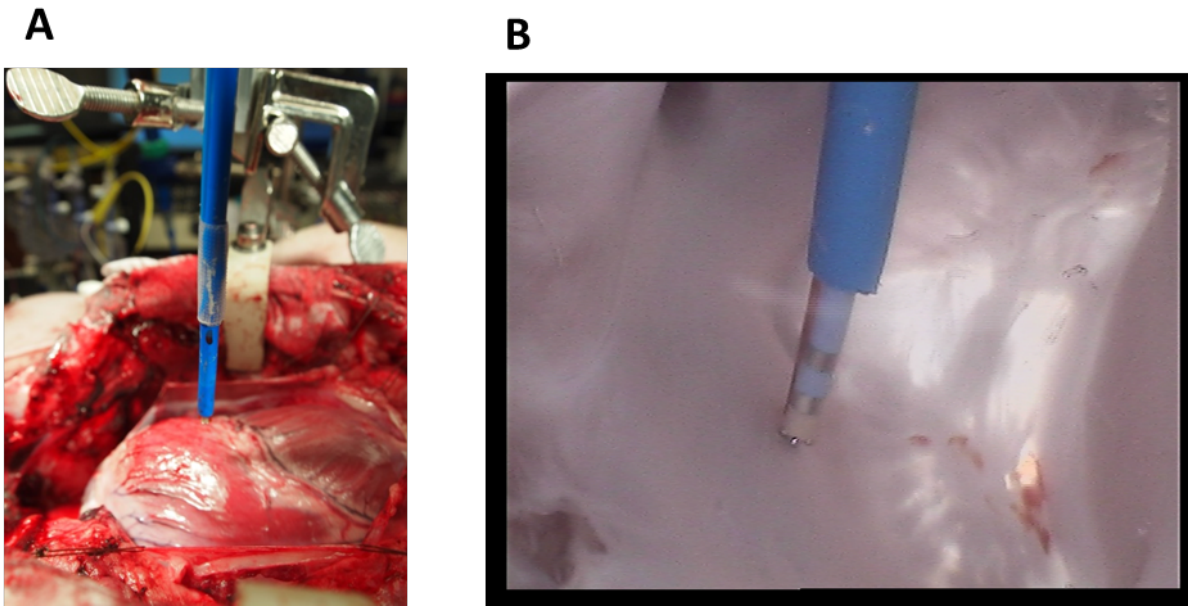

Figure 6.5: (A) The catheter contained within the delivery sheath/fixture was oriented to be perpendicular to the epicardial surface of the right ventricle (RV). (B) The catheter's electrode tip and fiber Bragg grating were near the endocardial surface in the right atrium on the Visible Heart® apparatus.

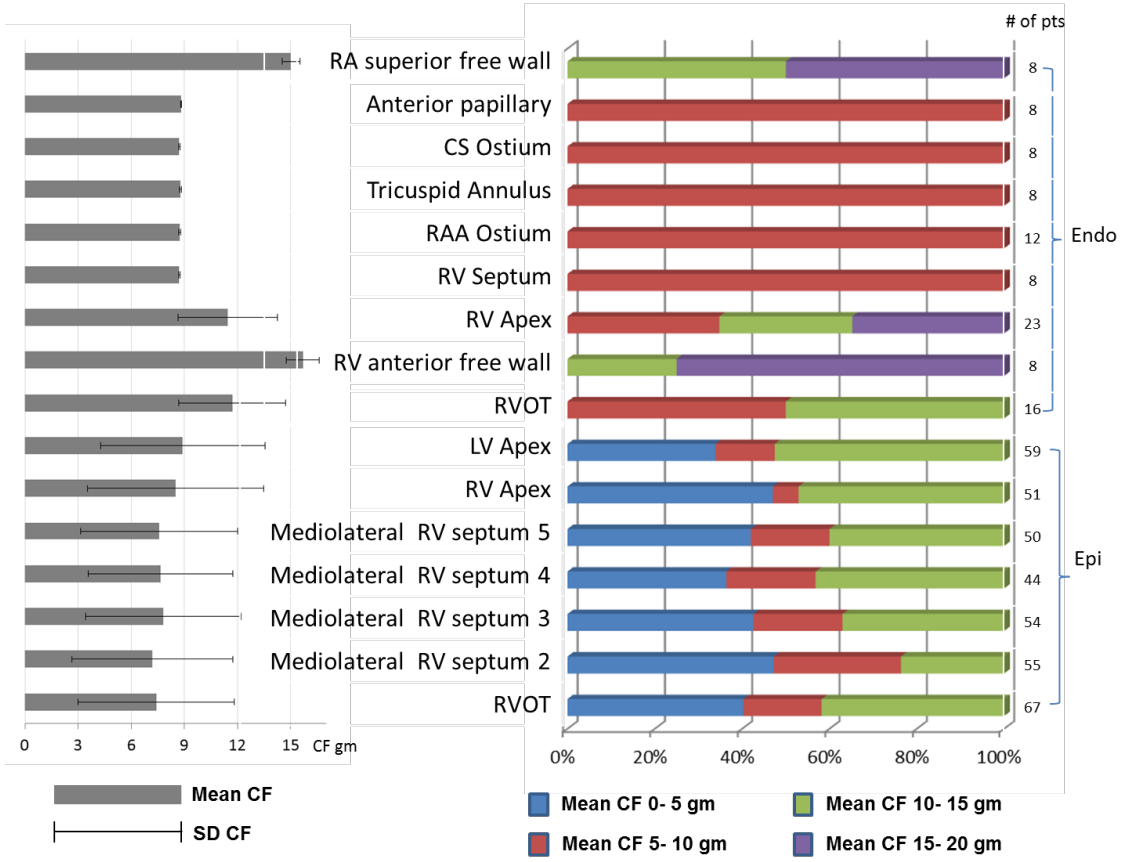

Figure 6.6: Catheter tissue CF (including the mean and SD) is depicted at all endocardial and epicardial mapping points. Color bars indicate 100% of measurements by anatomic location; the percentage breakdowns, bands of CF (grams); gray bars, the mean and SD at each anatomic point. At the far right, the number of points by anatomic location is indicated in either an epicardial (Epi) or endocardial (Endo) grouping. CF = contact force, RVOT = right ventricular outflow tract, RV = right ventricle, LV = left ventricle RAA = right atrial appendage, CS = coronary sinus, RA = right atrium, gm = grams

The mean CF to generate MAPs for all 9 pigs was 9.54 ± 2.43. Given the large variation in CF between anatomic locations, we performed Levene's test, resulting in an overall equal population variation across all hearts ($P = 0.969$). CF was lowest at the mediolateral RV septum locations (7.56 ± 4.36) and highest at the RA free wall (15.68 ±

0.936) (Figures 6.6). The CF required to generate MAPs was significantly higher ($P <$ 0.0001) in the RA in the RA free wall (15.68 ± 0.936) and the superior free wall (15.01 ± 0.505), as compared with the overall mean.

Across all anatomic locations, CF ranged from 1.05 to 22.67 grams. Of the total of 470 points, we observed low CF (1 to 5 grams) at 157 points (32.8%); modest CF (5 to 10 grams) at 128 points (26.81%); moderate CF (10 to 15 grams) at 176 points (36.51%); and high CF (15 to 20 grams) at 18 points (3.7%) (Figure 6.6).

Epicardial RV mapping

We measured 7 anatomic locations in situ, for a total of 380 points from 7 hearts. All data, expressed as the CF required to collect the first 4 consecutive MAP signals, were broadly distributed (Figure 6.7A). The mean CF for the mediolateral RV septum locations (Figure 6.7B) did not differ significantly. But the mean CF for the RV septum locations (7.56 ± 4.36, Figure 6B and for the RV and LV apex (8.7 ± 4.81, Figure 6.7B), *nearly* differed significantly ($P = 0.08$). The mean CF for the RV apex (8.5 ± 4.98) and for the LV apex (8.89 ± 4.63) did not differ significantly ($P = 0.56$).

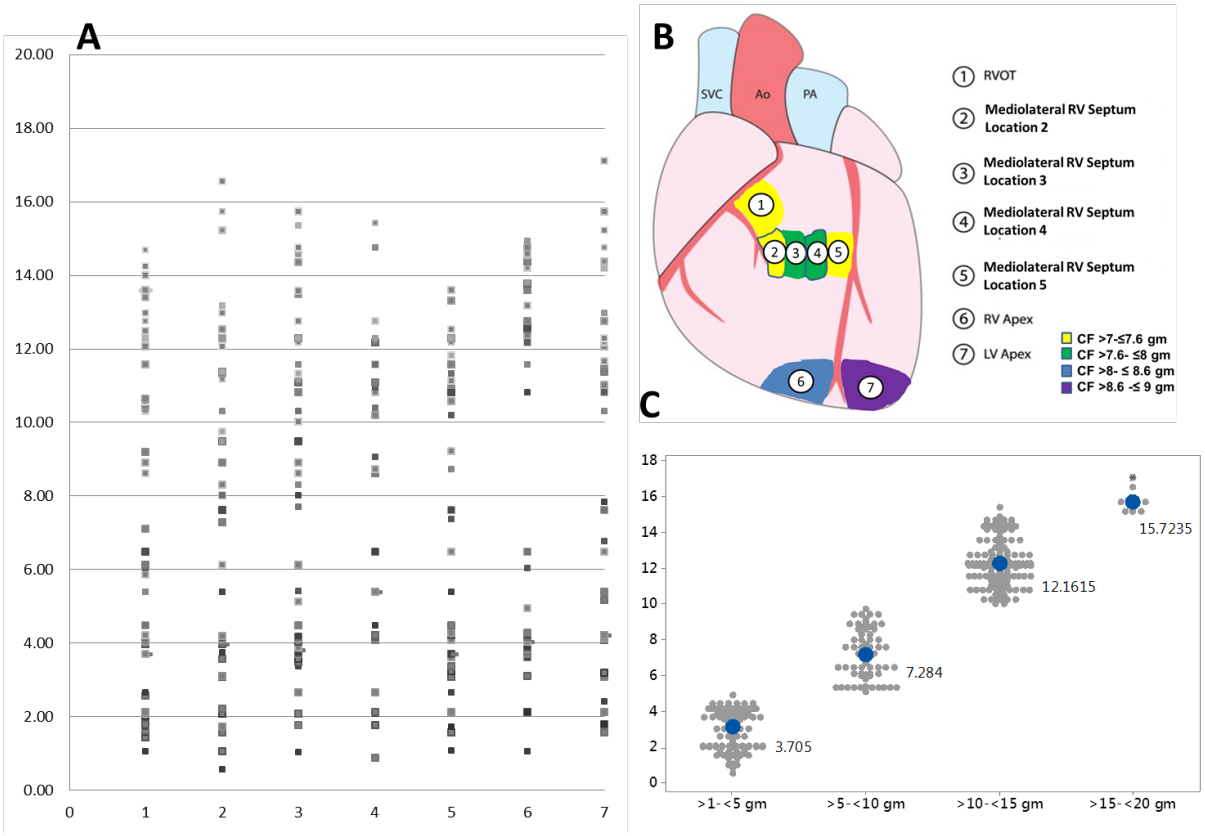

Figure 6.7: (A) We collected all of these points, in 7 anatomic locations. (B) We organized the 7 anatomic locations by CF color bands. (C) The blue dot is the mean CF, the grey dots are each observation. CF = contact force, RV = right ventricle, LV = left ventricle RA = right atrium, gm = grams

We defined the point of first contact as the first set of 4 consecutive MAPs. To refer to the points where all 4 electrodes were in contact with the tissue, we used the phrase "all on." When the catheter was removed from a location, the CF for the last 4 consecutive MAPs was also taken. The mean CF for all epicardial anatomic points from the first 4 consecutive MAPs (7.56 ± 4.36 grams) and for "all on" engagement (10.83 ± 2.29 grams) differed significantly ($P < 0.0001$). However, for those same epicardial anatomic

points, the mean CF from the first 4 consecutive MAPs (again, 7.56 ± 4.36 grams) and for the last 4 consecutive MAPs (8.67 ± 5.32) did not differ significantly ($P = 0.10$) (Figure 6.8).

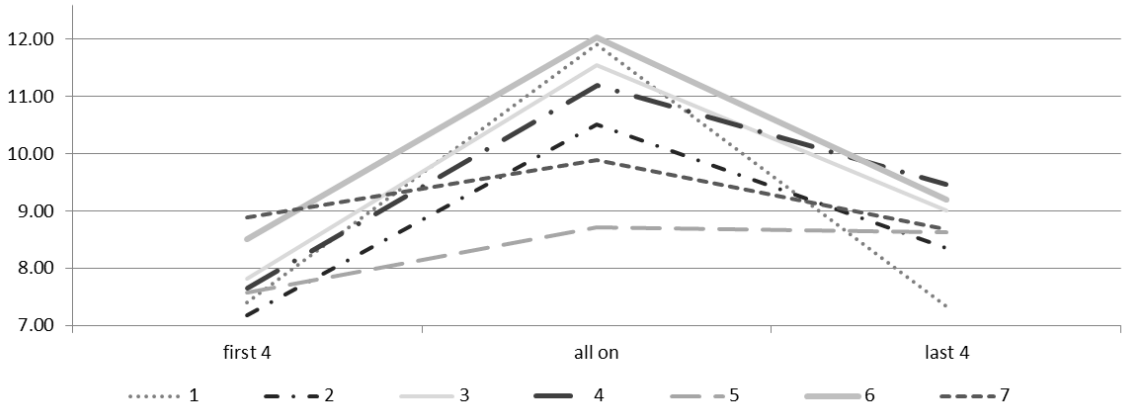

Figure 6.8: Each line represents an individual swine heart (n = 7). The "first 4" point indicates the mean contact force (CF) required to generate 4 consecutive monophasic action potentials (MAPs) across all epicardial anatomic points; the "all on" point, the mean CF when the catheter tip is fully engaged in the tissue; and the "last 4" point, the last 4 consecutive MAPs.

The CF for the first 4 consecutive MAPs was significantly lower than for the entire catheter tip (all on) ($P < 0.0001$). The application of the catheter in a given anatomic location resulted in tissue deformation from the CF of the catheter tip on the tissue. Yet the deformation did not result in a significant difference between the CF required to generate the first 4 and the last 4 consecutive MAPs ($P = 0.111$).

Endocardial mapping

Having successfully obtained MAPs employing the epicardial approach, we collected data at endocardial points, under direct visualization, using Visible Heart®

methodologies. To ensure proper catheter placement, we made slight changes in tip location. Some investigators have speculated that placing the catheter in the same location enables the same set of cells to be in contact with the catheter electrode. Our ability to do so was eased by the absence of respiratory movements and by the large reduction in cardiac contraction based movement.

Placing the catheter in the same location contributed to the smaller SD in 5 endocardial locations (0.037, 0.058, 0.057, 0.041, 0.03) (Figures 6.9A and 6.9B). The highest mean CF required to generate MAPs was for the RA superior free wall (15.68 ± .93) and for the RV anterior free wall (15.01 ± 0.5).

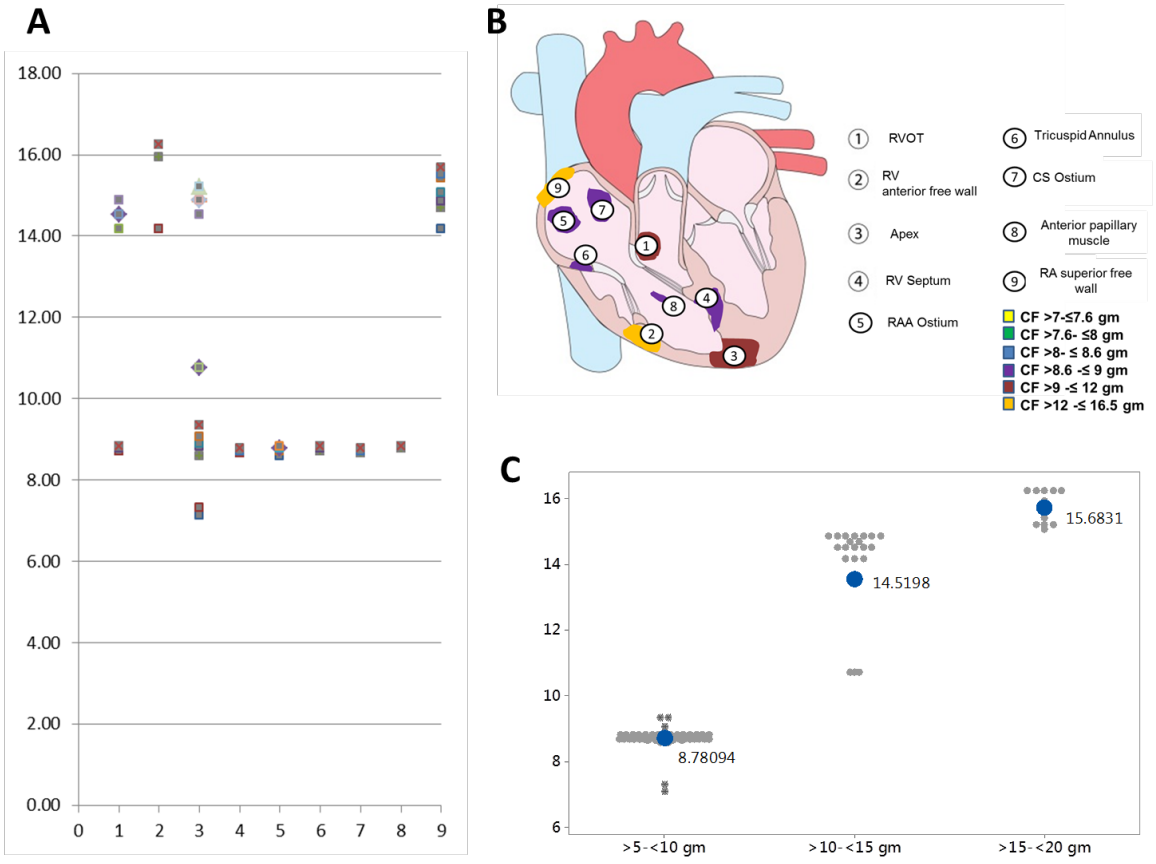

Figure 6.9: (A) a total of 9 anatomic locations showing the distribution of CF at each location. (B) 9 anatomic locations by CF color bands. (C) The mean is shown by blue dot, all observations are grey dots within 3 bands for all points. CF = contact force, RVOT = right ventricular outflow tract, RV = right ventricle, LV = left ventricle RAA = right atrial appendage, CS = coronary sinus, RA = right atrium. gm = grams

According to Levene's test, the variation was equal for all 4 hearts ($P = 1.00$). The equal variation was due, in part, to the absence of any respiratory influences and to the reduction in cardiac movements, since these hearts were functioning in vitro.

Variation from heart to heart

In our study, CF depended not only on the anatomic location but also on the individual heart (Figure 6.10). We observed wide variation in the mean CF from heart to heart. Of note, the mean CF for hearts 6 and 7 (11.47 grams) was significantly different than for hearts 1, 2, 3, 4, and 5 (5.05 grams) ($P < 0.0001$).

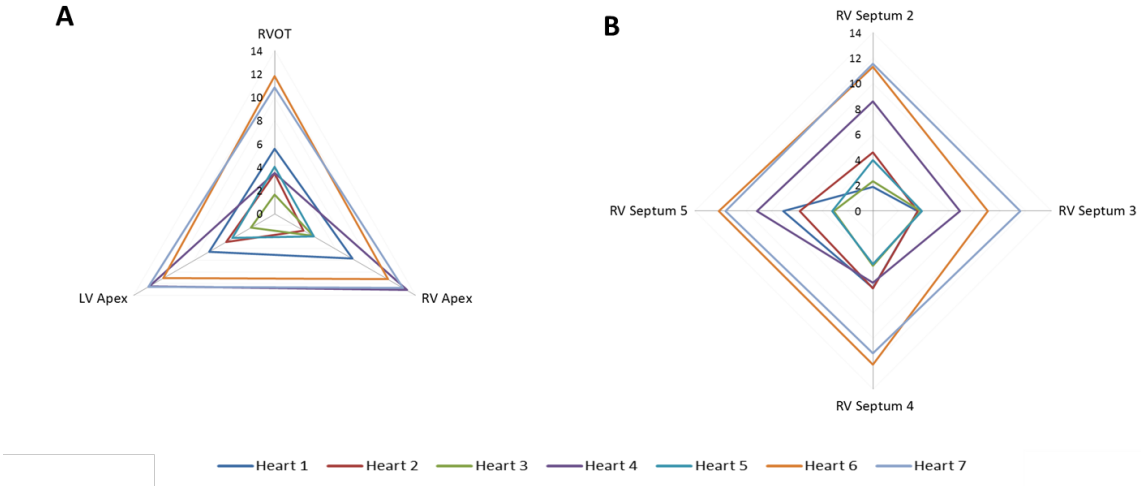

Figure 6.10: CF differences at each epicardial point collection location. (A) CF is shown at the right ventricular outflow tract (RVOT), right ventricular apex (RV apex), and the left ventricular apex (LV Apex) 3 epicardial points. (B) CF is shown at 4 epicardial septum locations of the RV septum. RVOT = right ventricular outflow tract, RV = right ventricle

It is possible that differences related to the makeup of the tissue stiffness may contribute to the heart to heart variation. Additional trials are needed to understand further the extent of variation from heart to heart.

Anatomic point variation

CF exhibited large variation about the mean, so we normalized the data, using an epicardial reference, in order to reduce the variation associated with the specimen. We used in situ measurements of 7 anatomic locations with the mediolateral RV septum 4 as the reference point. The normalized CF did not differ significantly from the CF for the mediolateral RV septum locations (2, $P = 0.139$; 3, $P = 0.227$; 5, $P = 0.815$) and for the 2 inferior locations (6, $P = 0.088$; 7, $P = 0.397$) (Figure 6.11). But the normalized CF differed significantly from the CF for the RVOT ($P = 0.004$).

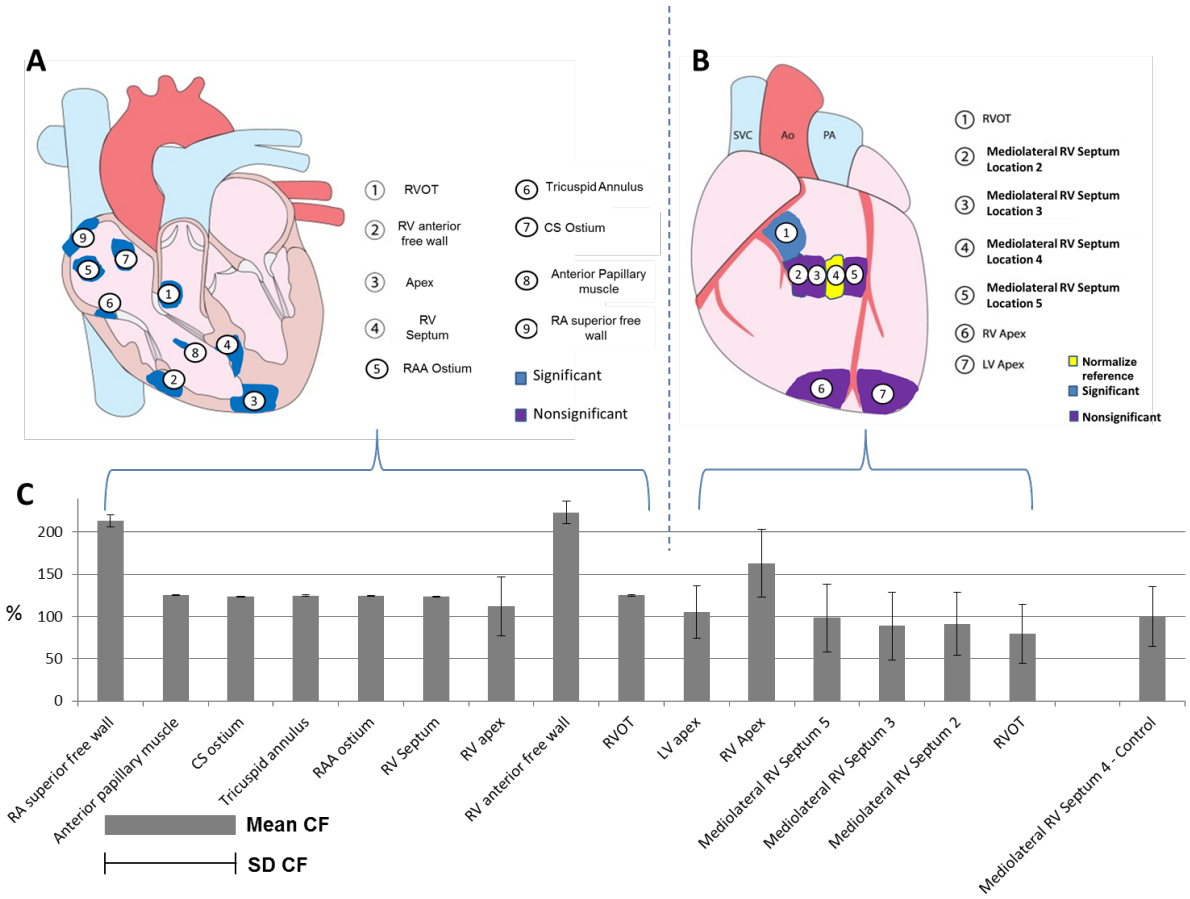

Figure 6.11: (A) 9 endocardial locations by whether CF was significantly (blue) or nonsignificantly (purple) different from the normalized epicardial reference (yellow). (B) 7 epicardial locations by whether CF was significantly (blue) or nonsignificantly (purple) different from the normalized epicardial reference (yellow) CF = contact force, RVOT = right ventricular outflow tract, RV = right ventricle, LV = left ventricle RAA = right atrial appendage, CS = coronary sinus, RA = right atrium

To examine the relationship between the epicardial reference point and the endocardial locations, we performed an additional normalization to a single epicardial location. Using the mediolateral RV septum 4 as the reference point, we measured 9 anatomic locations. The normalized CF was significantly different from the CF for all 9 endocardial locations: RVOT ($P = 0.038$), RV anterior free wall ($P = 0.0001$, apex ($P =$

0.0001), RV septum ($P = 0.048$), RA ostium ($P = 0.0441$), tricuspid annulus ($P = 0.0394$), CS ostium ($P = 0.0489$), anterior papillary muscle, and RA superior free wall ($P = 0.0001$).

Discussion

In our study, we illustrated several key points: (1) the CF required to generate MAPs varied widely; (2) small changes in anatomic location did not result in significant differences in the CF; (3) large changes in epicardial location *did* result in significant differences in the CF; (4) the mean CF across hearts often differed significantly; and (5) the mean CF to generate MAPs differed significantly from the mean (20 grams) commonly used to generate an endocardial RF lesion.

Recently, numerous studies have examined CF as it relates to generating RF lesions in various anatomic locations. According to those studies, the CF required to generate ablation lesions ranges between 9 and 40 grams. [131, 136, 137] In our study, we observed mean CFs to generate a MAP were lower than CFs suggested to generate effective RF lesions.[131, 138, 139] Effective RF lesion creation can be accomplished with a range of CF and these studies suggest that 20 grams of CF may be a very effective amount of force. The differences between suggested CF of these studies compared to the CFs from this study may suggest that the force needed to generate MAPs may be different than those used for ablation. We also used a novel catheter to simultaneously record both CF (grams) and MAPs. Those measurements proved useful in determining any differences in the CF required in different anatomic locations. The ability to combine ablation and

MAP CF may prove to be an effective tool to improve the overall ablation procedure. To the best of our knowledge, ours is the first systematic study to examine in vivo CF as it relates to generating MAPs.

Our novel data indicate that it is possible to describe the CF to record MAPs epicardially or endocardially. During our study, we did not have an instance of perforating the heart as we were applying CF. In addition, we observed a threshold of CF where the signals would change in morphology (Figure 6.12). As the catheter CF decreased, the shape of the signal changed: the tissue did not have the necessary depolarization from the catheter to enable us to measure the changes in boundary current and thus record MAPs.

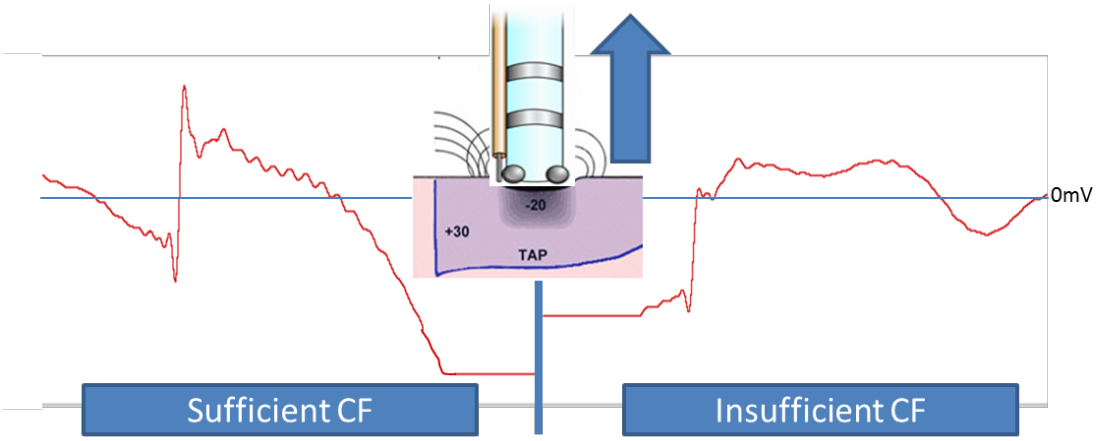

Figure 6.12: The signal on the left had sufficient CF (contact force). The change in the signal as the catheter was removed is depicted on the right: that CF was insufficient to generate monophasic action potentials (MAPs).

Future work is needed to collect additional data from *human* hearts, in order to better understand that these signals change and that they have implications for repolarization.

In our study, we noted that the required CF varied with the anatomic site being

investigated. The sensor method that we used was very effective for a catheter-based approach and provided a nearly instantaneous response to changes in CF. When recording MAPs clinically, one needs to consider the effects of cardiac and respiratory movements along with challenges of catheter placement on the anatomy. In our study, we accounted for such effects by using a series of 4 consecutive MAP signals (first and last) to define successful contact. Doing so prevented the use of premature signals that could have been induced by cardiac or respiratory movements. Yet even greater data fidelity might be achieved by computational models that can eliminate the effects of cardiac and respiratory movements. A future study focusing on developing an adaptive model to compensate for respiratory and cardiac movement to isolate the genesis of the first MAP signal could more precisely describe the CF required. In addition, improving the catheter design to allow it to be used is varying tip orientations may extend the usefulness of the device.

The ability to characterize the amount of CF to properly detect and record MAPs has important clinical applications, e.g., relative to understanding how to ensure that ablation lesions are effective within an anatomic region. It may be possible to use the presence of a MAP as an indicator that the minimum CF needed for RF lesion creation has been satisfied. Therefore, serving as an indicator to determine when to apply ablation therapy. Additional work needs to be done to integrate this technology with an ablative capability, so that MAPs can be measured and ablated in the same location.

Our use of the fiber Bragg grating was a highly effective way to augment the operation of

the catheter and to measure CF in a large number of different anatomic locations. However we did observe that the fiber Bragg grating sometimes broke at the tip. In order to prevent a compromise in operation, we used 8 different fibers across the 9 swine hearts. Each grating was calibrated, and linear expressions derived, in order to convert frequency into grams. Each linear expression between nanometer frequency and grams had an observed R-sq. of between 0.98 and 0.995 over a range of .2 to 20 grams. The fiber Bragg grating was most accurate when it was perpendicular to the tissue surface. For all of our endocardial measurements, we used direct visualization in the Visible Heart® to validate catheter tip orientation before signal collection.

To evaluate the relative importance of an orthogonal catheter orientation, we collected a total of 24 points that focused on catheter orientation (Figure 6.13). First, in the mediolateral RV septum, we tried a perpendicular orientation, resulting in mean CF of 12.21 ± 5.62. Placing a 20-degree inferior tilt on the catheter resulted in a mean CF of 10.07 ± 6.29. A 20-degree superior tilt resulted in a mean CF of 10 ± 6.56. But those differences were not significantly different (P = 0.33).

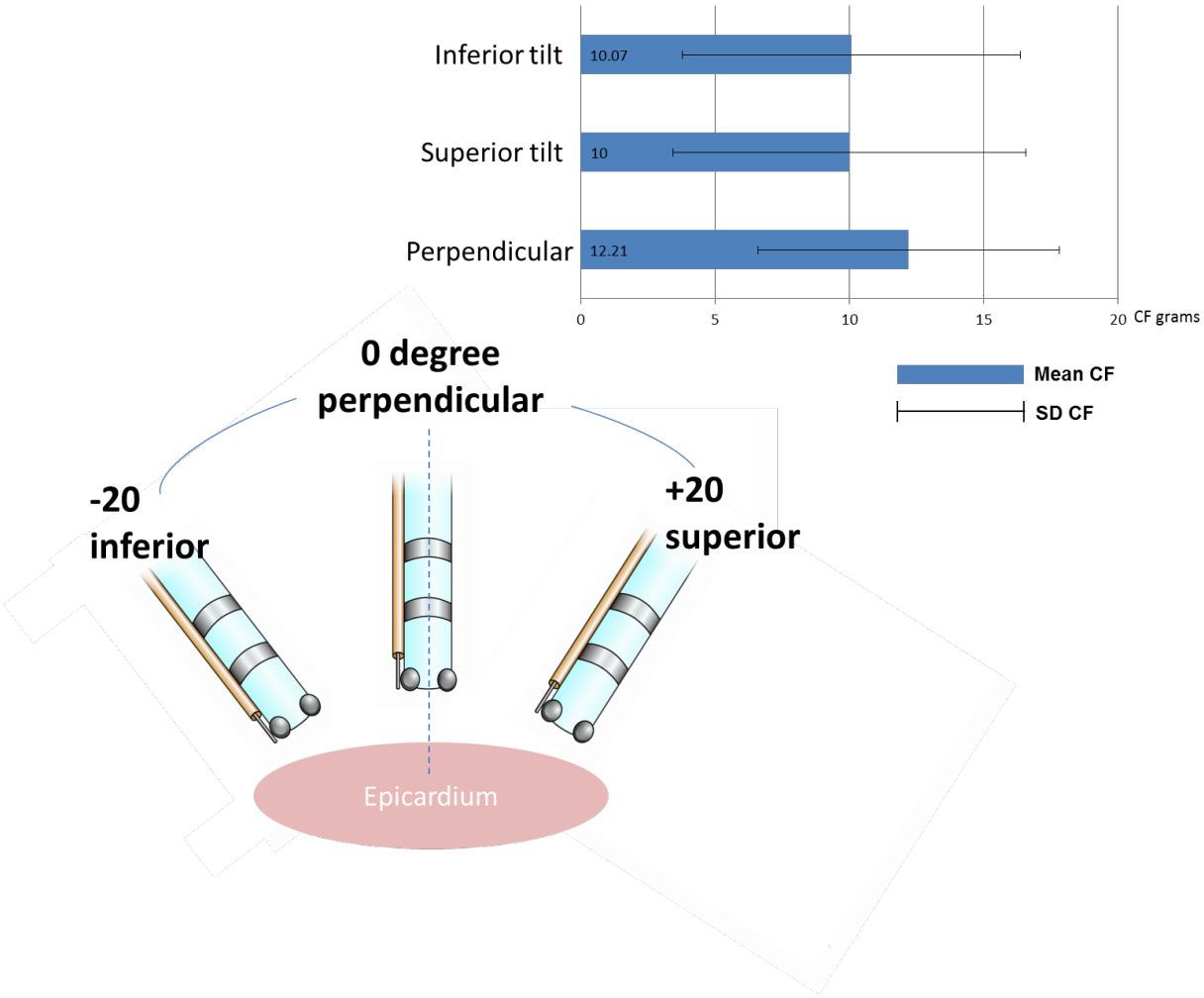

Figure 6.13: Changing the catheter tip orientation and position changed the contact force (CF) at the same anatomic epicardial location.

Thus, if the catheter was not in an orthogonal orientation, the relative variation in the amount of CF required to generate MAPs varied, on average, by 20%.

Study limitations

We need to mention several limitations unique to the methods we used. First, the fiber Bragg grating was mounted to the catheter shaft, resulting in both strong sensitivity and

exposure that, at times, caused the grating to break when placed against anatomic structures. Second, each piece of grating had a unique frequency, resulting in the need to calibrate each grating. A consistent frequency for every grating might have resulted in better data consistency. Third, the adjustment of cardiac and respiratory movements could be improved by considering a device that compensates for anatomic movements, potentially leading to a higher resolution of the CF.

Conclusion

In this study of catheter use in swine hearts, we successfully showed the relative CF required to generate MAPs in various regional anatomies, both epicardially and endocardially. The mean CF required to generate MAPs was different across locations in/on the heart and varied from heart to heart. The mean CF required to generate MAPs was significantly lower than the mean CF required to generate an endocardial RF lesion. Yet, further studies are needed to improve the fidelity and capabilities of force integration with ablation procedures.

These novel insights should help both clinicians and catheter designers who need procedural requirements to generate reproducible MAPs from various locations in either the endocardium or on the epicardial surface of a beating heart. The ability to accurately record these underlying myocardial potentials could provide critical information during ablation procedures. MAPs can provide insight into local heterogeneities to allow targeting of ablative and biologic therapies.

Acknowledgements

This work was done in collaboration with all authors listed along with the support of Dr.

Mary Knatterud. In appreciation of all editorial contributions to this study.

7. Assessing the Integrity of Formed Cardiac Linear Lesions by Recording Focal Monophasic Action potentials and Contact Forces: a Technical Brief

Mark A. Benscoter, MS[1, 3], Paul A. Iaizzo, PhD[1, 2]

[1] Department of Biomedical Engineering, University of Minnesota (Minneapolis, MN)

[2] Department of Surgery, University of Minnesota (Minneapolis, MN)

[3] Department of Engineering, Mayo Clinic, (Rochester, MN)

Corresponding author:
Dr. Paul Iaizzo
iaizz001@umn.edu
University of Minnesota
B172 Mayo, MMC 195
420 Delaware Street S.E.
Minneapolis, MN 55455
Telephone: (612) 625-9965
Fax: (612) 624-2002

Brief Title: A novel technique for an improved understanding of how to locate gaps in the linear ablation lines

Relationship with Industry: Research contract with Medtronic, Inc.

Keywords: Atrial fibrillation, catheter ablation, magnetic resonance imaging, mitral isthmus, coronary sinus

Abbreviation List: AF = atrial fibrillation, LA = left atrium, MI = mitral isthmus

Preface

The inspiration for this study arose from the development of a catheter device used for the collection of monophasic action potentials as part of the previous chapter. Monophasic action potentials (MAP) have been demonstrated as a method to depict cardiac depolarization that is able to be collected through the use of an intracardiac catheter. These signals can be collected when physical pressure is placed against the tissue causing the waveform to pass underneath the catheter tip as the tissue depolarizes. The previous chapter proved a method to collect MAPs and the necessary contact force to generate them in various anatomic locations.

This technical brief is designed to apply this device design to bring together the contact force and MAPs as a way to help direct ablation therapy to the areas that are electrically conductive at the tip of the catheter. If the tissue at the tip of the catheter is electrically conductive, then these locations may be those where additional ablation is needed.

For this study, I was responsible for making the devices, calibration, study design, conducting the data collection, data analysis, and publication creation. A biomedical engineering student, Megan Schmidt, assisted in data collection. The contents of this chapter were submitted as a manuscript to IEEE Engineering in Medicine and Biology.

Summary

The use of therapeutic ablations in patients with atrial fibrillation has become mainstay in the treatment of this disease. Yet, often such individuals require multiple procedures: in other words, successful first time treatments are impacted by challenges in generating linear lesions in specific anatomical regions like the mitral isthmus of the left atrium. Hence, there is a need to find reliable assessment techniques to address the presence of conduction gaps at the time of lesion creation. In this study, we describe a novel approach to examine conduction gaps, i.e., by using a proof of concept device to examine the local activation in the area of the lesion to locate gaps in the lesion set. Both epicardial and endocardial linear ablation lines composed of focal lesions with conduction gaps were created in a porcine model. Investigations of epicardial placed linear lesions applied on the right ventricle, including a conduction gap, were performed while recording monophasic action potentials (MAPs). Endocardial ablations were performed on the left atrial mitral isthmus.

We were able to successfully demonstrate the use of a proof of concept MAPs catheter with the ability to find a conduct gap within a linear lesion set: in those instances where no signals were collected, the device was able to collect the amount of applied force in both epicardial and endocardial locations. This device could be employed clinically with a novel catheter design, so to better assess lesion quality: i.e., importantly identify the existence of a conduction gap.

Introduction

Today, mitral isthmus (MI) ablations are conducted in a given patient in an attempt to decrease the likelihood of reoccurrence of atrial fibrillation. [140,141] Yet, anatomic challenges may often have an unintended consequences in performing these procedures, with even the possibilities of generating proarrhythmic outcomes. [140,141] Additionally, creations of incomplete MI lesions may lead to a slow conduction pathway that could ultimately result in left atrial tachycardia. [142,143,144,145] Yet, the occurrences of post-ablative conduction gaps in such procedures have also been associated with limitations of currently available catheter ablation devices. [146,147,148] In other words, the current limited clinical ability to critically locate a potential conduction gap in a planned lesion, is an opportunity for both innovative tools and techniques aimed at improving such procedures.

The primary objective of this report was to evaluate the relative clinical utility of simultaneously monitoring monophasic action potentials (MAPs) and contact forces as a means to improve one's abilities to locate conduction gaps within elicited linear radiofrequency (RF) lesions.

Methodology

These study protocols were reviewed and approved by the University of Minnesota Animal Care and Use Committee. Two swine hearts were reanimated with a clear Krebs-Henseleit buffer using Visible Heart® methodologies to generate video footage during ablation procedures: endocardial images were obtained using either a 4.0 or 6.0 mm diameter videoscope (Olympus, Center Valley, PA. .[149,150] MAP signals were

characterize by determining relative occurrences and relative waveform properties relative to tip location of a catheter. Thus, these signals enable a more detailed anatomic study of smaller areas of underlying myocardial substrate. [151,152,153,154] MAP generation requires achieving a threshold of activation. (Figure 7.1)

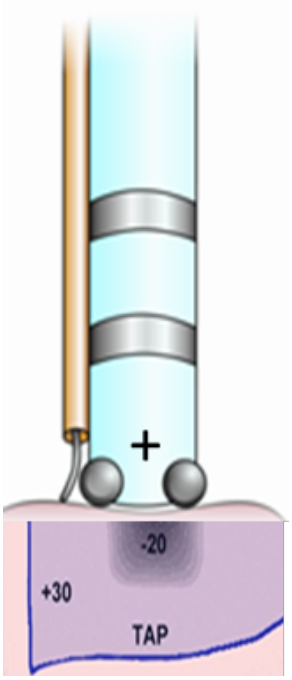

Figure 7.1: Shown is a depiction of the employed MAP catheter applied to the cardiac tissue: with a TAP moving past the type of the catheter with an amplitude of 30 mV. The simultaneous deflections of the fiber Bragg grating provided the simultaneous force information. TAP - transmembrane action potential, MAP – monophasic action potential

A catheter was developed that allowed for both the ability to collect MAP signals and contact forces (CF) (grams): i.e., the forces were obtained utilizing an optical fiber bragg grating. MAP signals were recorded as bipolar signals between tip electrodes to a 2 mm proximal ring electrode, using a filter bandwidth of 0.1 to 120 Hz for waveform collection. MAP collection was initiated with the presence of a signal morphology and a target

amplitude more than 2 mV. CF was collected by placing a calibrated fiber bragg grating against the myocardium and capturing the change in frequency that occurs with physical deformation of the fiber bragg grating. The calibration processes created the ability to derive the CF (grams). Additionally, reference ECG signal collection was performed using a bipolar electrogram and was collected with a filter bandwidth of 0.1 to 120 Hz. All MAP waveform collection and subsequent analyses was performed using the AD Instruments Bioamp system (Dunedin, New Zealand).

The experimental approach employed here included endocardial and epicardial ablations that were comprised of given series of linear lesions created with a focal RF ablation catheter. Direct visualization was used as a means to validate locations and catheter contacts. Here we used the process of determining the presence of a conduction by collecting MAP signals pre-ablation and the required amounts of CFs on the given tissue location. Any tissue that elicited a characteristic MAP was termed "conductive". Post-ablations, all anatomic locations were reassessed to determine if conduction gaps existed. In other words, if the amount of CF applied to a given location exceeded the pre-ablated CF and there was no detectable MAP signal, the location was deemed non-conductive. Furthermore, if MAP signals were present within a given ablated region, it was termed a gap in the linear lesion.

The epicardial lesion patterns that was employed in the present study were fashioned after the work done by Ranjan and Kato et Al. [146] e.g., who devised a method for the creation and assessment of conduction gaps following applied linear lesions for epicardial

applications. Specifically, here we generated lesions using a RF ablation system (Contactr catheter and an Atakr RF generator, Medtronic, Inc., Minneapolis, MN, USA). An initial power settings of 30 watts was used during the primary lesion pattern creation: note, additional applications of RF used (50 W over 10-30 seconds) were sometimes required for regions within the lesion pattern where MAPs persisted.

To determine the conduction properties of the myocardium, electrical stimuli were delivered to the right ventricular (RV) epicardium using constant current with 2-millisecond (ms) pulse durations at twice diastolic thresholds, with a setting of 7-9 milliamps (mA). (Figure 7.2A) Direct visualization also aided to confirm that the catheter electrodes and force sensors were located at the same anatomical locations of the detectable lesions: i.e., to ensure accurate measurements were conducted. (Figure 7.2A, B)

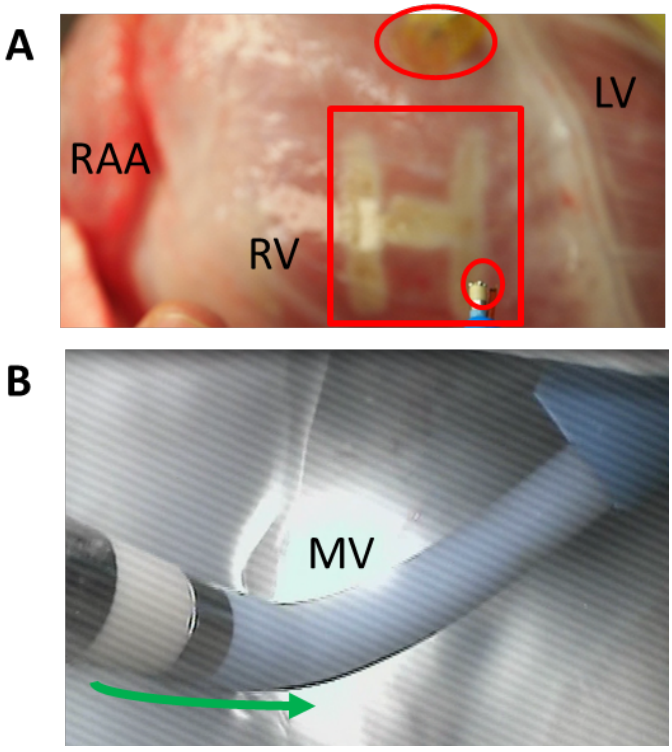

Figure 7.2: Imaged of ablations performed on the reanimated swine heart specimens: (A) epicardial linear lesion on the RV with upper oval as external pacing site and lower oval contains tip of MAP catheter, and (B) LA endocardial image showing mitral isthmus linear lesion creation moving towards mitral valve annulus (green arrow). LV – left ventricle, and MV mitral valve RAA – right atrial appendage, RV – right ventricle.

In addition to epicardial linear lesions, left atrial endocardial MI linear lesions were also created and examined for the presence of a given conduction gaps. CF collections in epicardial and endocardial locations were conducted at each measurement location, once 4 consecutive MAP signals were observed. This was done to compensate for the relative effects of cardiac movements and to prevent premature identifications of depolarization. Note, these effects were more prevalent for the epicardial assessments than for the endocardial ones.

Multiple assessment locations were collected within each generated lesion set. For example, the first pattern (set #1) shown in Figure 7.3A, contained a conduction gap at location B3. After the creation of this epicardial H pattern, 6 CF measurements were obtained from 5 locations within the lesion pattern and 1 outside the pattern with MAP signals appearing at 2 (B3 and D1) locations (green) and a CF of 7.3 and 8.9 grams: note, both of these locations were non-ablated tissue (Figure 7.3B). Further, no MAP signals were elicited within or recorded from the remaining 4 locations in this lesion pattern: A4, B2, C1, and C4 (red). For these same epicardial studies, a second ablation of the pattern was then produced: this time, the only ablation related change was an additional application of RF in location B3.

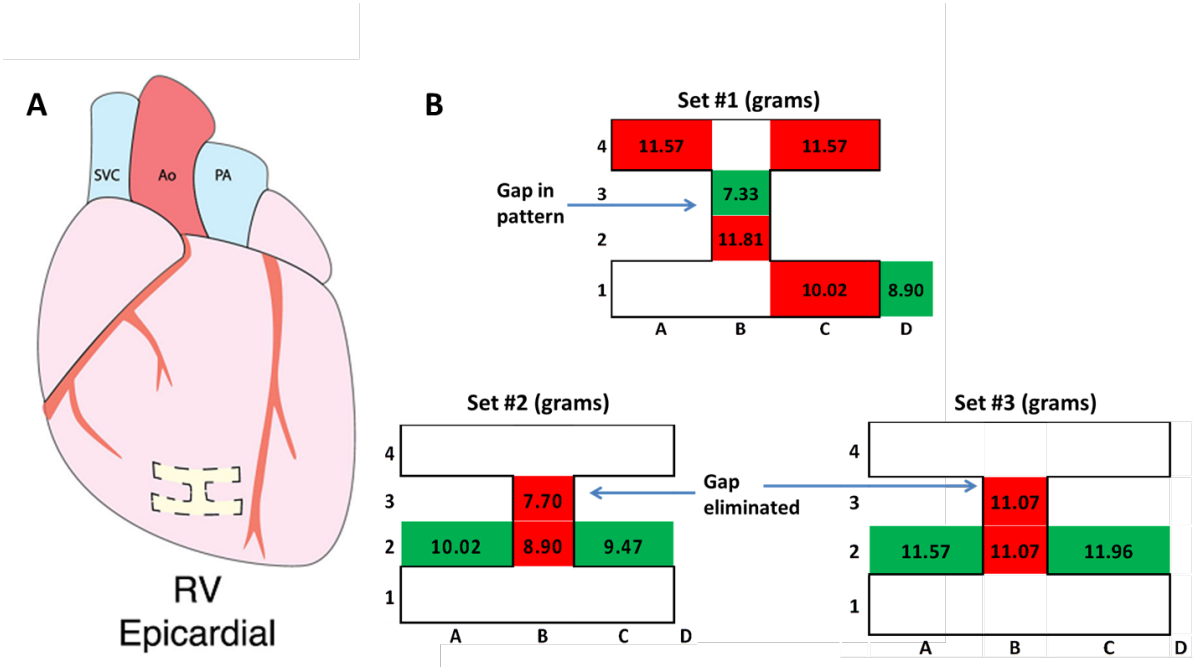

Figure 7.3: Elicited epicardial lesion patterns: (A) location of the linear lesion pattern on RV; (B) CF applied in different anatomic locations on or adjacent to the lesion pattern. CF is indicted for each location with red indicating no MAPs were detected and the green indicates that MAPs were elicited. CF – contact force, MAP – monophasic action potential, RV right ventricle.

MAP signal collections were attempted at locations A1, B2, B3, and C2 with no MAP detectable at location B2 and B3 (red). A further validation of the induced lesion pattern was also conducted by assessing for MAPs at locations A2, B2, C2. A2 and C2: these locations were outside the lesion pattern and MAP signals were collected (green). In this example, site B2 did not elicit a MAP signal with a CF of 8.9 grams (red). The heart was then allowed to stabilize: lesion set 3 was then induced. In this subsequent lesion set, only MAP and CF measurements were taken in the same locations as set #2 without any additional RF. The applied CFs were stepwise increased in all locations to ensure good contact and the lack of any detectable MAP signals. For example, at location B3 the reassessed CF was increased up to 11.1 grams and no MAP generated (red). A2 and C2

were outside the lesion pattern and both generated MAPs with a peak force of 11.6 and 12.0: at location B2 a peak CF of 11.1 grams was applied without the ability to record a MAP (red). In summary, the use of this dual parameter assessment/mapping catheter was able to define the locations of the lesion gap in set #1. Again, after an additional application of RF, at the gap, MAP signal detection was no longer possible. Yet, catheter assessment validations were frequently conducted by measuring a location outside the lesion patterns and each time MAP signals were visible. Finally, increased CF could be applied, so to ensure good tissue contacts.

A similar approach was used in the creation of an endocardial left atrial MI ablation: linear RF lesion were generated. In one example of this procedure, a MAP catheter was placed in 9 sequential locations on the generated linear lesion, in an attempt to record both MAPs and the CFs (Figure 7.4). In this case, from locations 1, 4, 5, 6 it was not possible to record MAPs (red), but from the remaining locations it was (green).

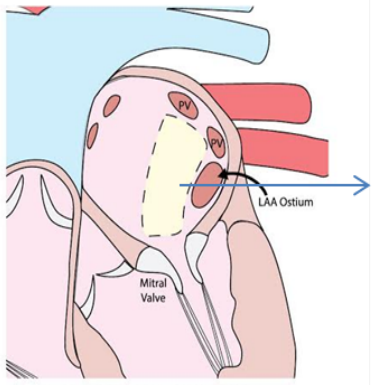

	force (g)
1	13.42
2	5.71
3	9.45
4	13.42
5	10.38
6	10.17
7	9.60
8	9.52
9	9.60

Figure 7.4: Provided here are the noted CFs for the placements of our assessment catheter at 9 anatomical locations on the endocardium of the LA in the region of the MI. Red bars indicates that no MAP was elicited and green indicates that a MAP recordings were obtained. CFs in grams are listed for each of 9 locations on the lesion. CF – contact force, LA – left atrium, MI – mitral isthmus.

In this example, MAPs were recorded at CFs less than 10 grams. Similar CFs were applied in the ablated anatomical locations where MAPs were not observed. Too low of applied CFs and the presence of a MAP could be likely locations to additional RF application to increase the quality of the linear lesion. These results which were reproducible in multiple isolated swine heart studies may provide novel approach to help one clinically identify the needs for additional ablations to minimize symptom recurrences.

Conclusion

The creations of functional linear lesions either applied endocardially and epicardially relies on the effective applications of therapy. Yet, often the resulting lesions can be varied in sizes and depths due to changes in tissue properties or changes in the amount of contact the given therapeutic catheter has with the underlying tissue. Hence, the ability to use an adjuvant method that is able to detect the relative viability of the tissue at the location of the lesion at the time of the clinical application may allow for greater precision in creating a therapeutic linear lesion. Therefore, the use of a focal catheter that has means to simultaneously collect MAPs, contact forces, and create RF lesions may be a methodology to improve the overall clinical ablation procedure: i.e., by providing an innovative way to understand changes in a linear lesion at the time of their generation.

Thesis Summary

The US Department of Health and Human Services reports that the treatment of atrial fibrillation (AF) using radiofrequency ablation is effective at stopping it in 74 out of 100 patients when examined 1 year after the ablations were conducted. This outcome is in part influenced by limitations of current medical device system design and challenging anatomies. Procedure outcomes and safety can be influenced by improving the understanding of how the anatomy interacts with these systems and examining innovative ways to use devices in the procedure. This served as the background for my research with the following objective: **To improve the safety and therapeutic effectiveness of AF catheter ablation through translational research focused on cardiac anatomy, cardiac physiology, and medical device design.**

My research was organized into a series of studies beginning with an overview of the catheter ablation procedure for paroxysmal, persistent, and permanent AF. This portion of the research focused on the impact of the therapeutic device and variations in cardiac anatomy to find opportunities for device improvement. This overview contained insights that shaped the objectives of the subsequent studies. The initial study undertaken was an examination of the interaction between the anatomy and mechanical properties of the fossa ovalis (FO) and the tools and techniques used in a transseptal puncture. Specifically, the puncture and tear forces of the FO were characterized when subjected to different forms of puncture and varying sized delivery systems to identity opportunities

for improved product/procedure safety and system usability. Going beyond the transseptal puncture, additional studies focused on ways to improve ablation-related outcomes. The initial therapeutic ablation lesion studied was the mitral isthmus (MI) linear ablation, used to terminate MI dependent left atrial flutter. Summary of the clinical procedure and technologies and a study of the anatomy of the coronary sinus and MI were performed that shaped a recommendation for future improvements in devices and methods. Next, a study of the generation of cardiac monophasic action potentials (MAP) were studied and correlated to contact force for both epicardial and endocardial anatomic locations. This fundamental research characterized cardiac substrate activity at the point of catheter application providing insight into improvements in ablation therapies and improved specificity in identifying targeted tissues. Lastly, a technical brief was used to introduce an innovative way to use MAPs and contact force as an adjuvant method in the creation of linear lesions. These studies provide unique scientific contributions by describing anatomic changes in AF patients in the coronary sinus and MI anatomy and changes to the AF ablation clinical procedural technic to improve ablation therapy application and served as an input for catheter device design. Also for the first time, this research described the contact force needed to generate MAPs in a number of anatomic locations. Finally, this research utilized an animal-based translational method to predict the behavior of transseptal tools in the human heart. The anatomic limitations of the FO to withstand the forces associated with a transseptal puncture were analyzed with a recommendation made for improved device design related to puncture method and device

size.

This catheter-based overview examined how ablation devices interface with tissue and how anatomic structures influence therapeutic success. Since anatomy and physiology vary from person-to-person and the endocardial surface changes shape with each beat and can prompt catheter placement migration, it is difficult to know exactly where the device has been placed and what is happening at the device-tissue interface. The unique ability of the Visible Heart apparatus to directly visualize the device tissue interface for each step in the procedure, allows an assessment of procedural limitations that contribute to the likelihood of arrhythmia reoccurrence and may increase AF ablation procedure time. The limitations identified in this unique model can serve as inputs into subsequent studies to improve patient safety and radio frequency (RF) ablation success.

The aforementioned study of FO anatomic serves to improve knowledge by proposing a method that can translate to human clinical usage. Limitations of current transseptal puncture tools and methods were discussed in addition to a study of how RF energy may be used as a way to improve the clinical procedure. This experiment included the creation of a new method to determine puncture and tearing force of tissue and applied it through these novel translational in vitro studies, in both human and swine. This work provides a perspective on the challenges of conducting a transseptal procedure and present compelling data for further discussion on device size constraints.

In addition to the opportunities associated with the transseptal puncture, there also exist

opportunities to improve catheter navigation as it relates to movement, placement, orientation, and stability. Ablation lesion formation is affected by catheter contact force and tissue thickness. The vascular anatomy of the coronary sinus and the morphology of the MI, in the region of the left atrium (LA), may contribute to limiting the effectiveness of RF ablation aimed at generation of a transmural lesion. The comparison of CS anatomy between AF and non-AF anatomies relied on the reconstruction of magnetic resonance images (MRI) enabled a detailed assessment of the anatomic differences that affect catheter use. This experiment used reconstructed AF anatomies to create unique insights such that greater contact force can be applied at the catheter tip to enable more precise tip placement in support of improved lesion generation. This study considered ways to influence catheter design that would contribute to improving the efficacy of linear ablation of the MI.

Understanding the interaction of devices with patient anatomy provides insights that can aid in therapeutic application. Currently, the understanding of what is occurring at the specific site of lesion creation is limited by the clinically available imaging methodologies. In this experiment, direct visualization of procedural technique was used to create unique visual insights as a method to report on ways to improving MI ablation outcomes. Combining anatomic and procedural studies can improve the success of ablation. However, if a gap in the linear lesion exists, additional information may be required to quantify the presence of discontinuity at the time of lesion formation.

MAPs offer the ability to describe the physiological properties as well as the viability of tissue that is present at the tip of the catheter. In this study of catheter use, we studied the relationship between MAP signal collection and contact force in a number of regional anatomies, both epicardially and endocardially. The study of the dynamic relationship of the MAP in the presence of arrhythmias can provide unique insight into the underlying mechanisms that enable/sustain AF. These innovative experiments created a way to simultaneously collect MAPs and contact force. Through determination of the contact forces required to reliably generate MAP signals, catheter constructions and methods for manipulation can be developed to improve the reliability with which MAP signals can be generated. These MAP signals can then be used as a way to determine if conduction gaps exist in linear lesion sets. These novel insights should help both clinicians and catheter designers who have procedural requirements to generate reproducible MAPs from various locations in either the endocardium or on the epicardial surface. The ability to accurately record these underlying myocardial potentials could provide critical information during ablation procedures or during attempts to focally deliver biologic therapies.

Finally, the creation of linear lesions relies on the effective application of a focal catheter. The resulting lesion can vary in size and depth due to changes in tissue properties or changes in the amount of contact the catheter has with the tissue. This research used the results of understanding MAP contact force and extended it to devise an adjuvant medical device method that is able to depict the viability of the tissue at the location of the lesion

at the time of lesion creation and shares these results in a technical brief. The use of a focal catheter as a means to collect MAPs and create RF lesions may improve the overall clinical ablation procedure by providing evidence of conduction, or lack thereof, at the location of the lesion.

This research primarily focused on challenges relating to the interaction of devices with the underlying cardiac anatomy. The results suggest catheter design inputs to improve the procedure for patient safety and therapy effectiveness. One important outcome of this work it that it has demonstrated that anatomy changes with the onset of AF and has exposed where limitations exist at the device-anatomy interface. The research has also devised a way to translate tissue puncture from animal to human, derived the forces required to generate MAPs, and has made suggestions to improve the current clinical procedure including an introduction as to how to use contact force and MAPs in linear lesion creation. The implications of this research have the ability to impact how CS/MI anatomic changes affect catheter navigation, providing insight into how to achieve improved catheter positioning to increasing the effectiveness of ablations through better contact and retained position. Understanding contact for MAPs will allow subsequent studies to bring together RF and MAP contact force to be used together to terminate conduction more effectively. Finally, exposing the limits of the transseptal puncture and the limitations of the current technology suggest that new innovation is needed to find less traumatic and safer methods of conducting this step in the procedure.

References

1. Haïssaguerre M, Gencel L, Fischer B, Le Métayer P, Poquet F, Marcus FI, Clémenty J. Successful catheter ablation of atrial fibrillation. J Cardiovasc Electrophysiol. 1994 Dec;5(12):1045-52.

2. Jaïs P, Shah DC, Haïssaguerre M, Takahashi A, Lavergne T, Hocini M, Garrigue S, Barold SS, Le Métayer P, Clémenty J. Efficacy and safety of septal and left-atrial linear ablation for atrial fibrillation. Am J Cardiol. 1999 Nov 4;84(9A):139R-146R.

3. Pappone C, Oreto G, Lamberti F, Vicedomini G, Loricchio ML, Shpun S, Rillo M, Calabrò MP, Conversano A, Ben-Haim SA, Cappato R, Chierchia S. Catheter ablation of paroxysmal atrial fibrillation using a 3D mapping system. Circulation. 1999 Sep 14;100(11):1203-8.

4. Yokokawa M, Sundaram B, Garg A, et al. Impact of mitral isthmus anatomy on the likelihood of achieving linear block in patients undergoing catheter ablation of persistent atrial fibrillation. Heart Rhythm 2011; 8:1404-10.

5. Becker AE. Left atrial isthmus. J Cardiovasc Electrophys 2004; 15: 809-12.

6. Wong KC, Jones M, Sadarmin PP, et al. Larger coronary sinus diameter predicts the need for epicardial delivery during mitral isthmus ablation. Europace 2011; 13:555-61.

7. Aurigemma GP, Gottdiener JS, Arnold AM, Chinali M, Hill JC, Kitzman D. Left atrial volume and geometry in healthy aging: the Cardiovascular Health Study. Circ Cardiovasc Imaging. 2009 Jul;2(4):282-9. doi: 10.1161/CIRCIMAGING.108.826602. Epub 2009 May 11.

8. Schmidt B, Ernst S, Ouyyang F, et al. External and endoluminal analysis of left atrial anatomy and the pulmonary veins in three-dimensional reconstructions of magnetic resonance angiography: the full insight from inside. J Cardiovasc Electrophys 2006; 17: 957-64.

9. Patwardhan A. Intraoperative ablation of atrial fibrillation—replication of Cox's maze III procedure with re-usable radiofrequency and cryoablation devices.

10. Multimed Man Cardiothorac Surg. 2010 Jan 1;2010(702):mmcts.2009.004192. doi: 10.1510/mmcts.2009.004192.

11. Patwardhan AM. Intraoperative ablation of atrial fibrillation using bipolar output of surgical radiofrequency generator (diathermy) and reusable bipolar forceps. J Thorac Cardiovasc Surg. 2007 Jun;133(6):1683; author reply 1683-4.

12. De Greef Y, Buysschaert I, Schwagten B, Stockman D, Tavernier R, Duytschaever M. Duty-cycled multi-electrode radiofrequency vs. conventional irrigated point-by-point radiofrequency ablation for recurrent atrial fibrillation: comparative 3-year data. Europace. 2014 Jan 16.

13. Marijon E, Fazaa S, Narayanan K, Guy-Moyat B, Bouzeman A, Providencia R, Treguer F, Combes N, Bortone A, Boveda S, Combes S, Albenque JP. Real-Time Contact Force Sensing for Pulmonary Vein Isolation in the Setting of Paroxysmal Atrial Fibrillation: Procedural and 1-Year ResultsJ Cardiovasc Electrophysiol. 2013 Oct 8. doi: 10.1111/jce.12303.

14. Haïssaguerre M, Jaïs P, Shah DC, Takahashi A, Hocini M, Quiniou G, Garrigue S, Le Mouroux A, Le Métayer P, Clémenty J. Spontaneous initiation of atrial fibrillation by ectopic beats originating in the pulmonary veins. N Engl J Med. 1998 Sep 3;339(10):659-66

15. Cox JL, Schuessler RB, D'Agostino HJ Jr, Stone CM, Chang BC, Cain ME, Corr PB,
Boineau JP. The surgical treatment of atrial fibrillation. III. Development of a definitive surgical procedure. J Thorac Cardiovasc Surg. 1991 Apr;101(4):569-83.

16. Cox JL, Boineau JP, Schuessler RB, Kater KM, Lappas DG. Five-year experience with the maze procedure for atrial fibrillation. Ann Thorac Surg. 1993 Oct;56(4):814-823; discussion 823-4.

17. Cox JL, Boineau JP, Schuessler RB, Jaquiss RD, Lappas DG. Modification of the maze procedure for atrial flutter and atrial fibrillation. I. Rationale and surgical results. J Thorac Cardiovasc Surg. 1995 Aug;110(2):473-84.

18. Kawaguchi AT, Kosakai Y, Sasako Y, Eishi K, Nakano K, Kawashima Y. Risks and
benefits of combined maze procedure for atrial fibrillation associated with organic heart disease. J Am Coll Cardiol. 1996 Oct;28(4):985-90.

19. Kottkamp H, Hindricks G, Autschbach R, Krauss B, Strasser B, Schirdewahn P, Fabricius A, Schuler G, Mohr FW. Specific linear left atrial lesions in atrial fibrillation: intraoperative radiofrequency ablation using minimally invasive surgical techniques. J Am Coll Cardiol. 2002 Aug 7;40(3):475-80.

20. Ranjan R, Kato R, Zviman MM, Dickfeld TM, Roguin A, Berger RD, Tomaselli GF,
Halperin HR. Gaps in the ablation line as a potential cause of recovery from electrical isolation and their visualization using MRI. Circ Arrhythm Electrophysiol. 2011 Jun;4(3):279-86. doi: 10.1161/CIRCEP.110.960567. Epub 2011 Apr 14.

21. Winkle RA, Mead RH, Engel G, Patrawala RA. The use of a radiofrequency needle
improves the safety and efficacy of transseptal puncture for atrial fibrillation ablation. Heart Rhythm. 2011 Sep;8(9):1411-5. doi: 10.1016/j.hrthm.2011.04.032. Epub 2011 May 6.

22. Tang M, Gerds-Li JH, Nedios S, Roser M, Fleck E, Kriatselis C. Optimal fluoroscopic projections for angiographic imaging of the pulmonary vein ostia: lessons learned from the intraprocedural reconstruction of the left atrium and pulmonary veins. Europace. 2010 Jan;12(1):37-44. doi: 10.1093/europace/eup365.

23. Iaizzo PA, Hill AJ, Laske TG: Cardiac device testing enhanced by simultaneous imaging modalities: the Visible Heart®, fluoroscopy, and echocardiography. *Expert Review of Medical Devices* 5:51-58, 2008.

24. Iaizzo PA, Anderson RH, Hill AJ: The importance of human cardiac anatomy for translational research. Journal of Cardiovascular Translational Research, Special Issue on Cardiac Anatomy 6:23139059, 2013.

25. Earley MJ. How to perform a transseptal puncture. *Heart* 2008;95:85-92.

26. Daoud EG. Transseptal catheterization. *Heart Rhythm* 2005;2:212-214.

27. De Ponti R, Cappato R, Curnis A, Della Bella P, Padeletti L, Raviele A, Santini M, Salerno-Uriarte JA. Trans-septal catheterization in the electrophysiology laboratory: data from a multicenter survey spanning 12 years. *J Am Coll Cardiol* 2006;47:1037-1042.

28. Jaïs P, Hocini M, Hsu LF, Sanders P, Scavee C, Weerasooriya R, Macle L, Raybaud F, Garrigue S, Shah DC, Le Metayer P, Clémenty J, Haïssaguerre M. Technique and results of linear ablation at the mitral isthmus. Circulation. 2004 Nov 9;110(19):2996-3002. Epub 2004 Nov 1.

29. Wong KC, Jones M, Sadarmin PP, et al. Larger coronary sinus diameter predicts the need for epicardial delivery during mitral isthmus ablation. Europace 2011; 13:555-61.

30. Wei W, Ge JB, Zou Y, Lin L, Cai Y, Liu XB, Zhu WQ. Anatomical characteristics of pulmonary veins for the prediction of postoperative recurrence after radiofrequency catheter ablation of atrial fibrillation. PLoS One. 2014 Apr 4;9(4):e93817. doi: 0.1371/journal.pone.0093817. eCollection 2014.

31. Estes NA, Halperin JL, Calkins H, Ezekowitz MD, Gitman P, et al. (2008) CC/AHA/Physician Consortium 2008 clinical performance measures for adults with nonvalvular atrial fibrillation or atrial flutter: a report of the American College of Cardiology/American Heart Association Task Force on Performance Measures and the Physician Consortium for Performance Improvement (Writing Committee to Develop Clinical Performance Measures for Atrial Fibrillation): developed in collaboration with the Heart Rhythm Society. Circulation 117(8): 1101-1120.

32. Berruezo A, Tamborero D, Mont L, Benito B, Tolosana JM, et al. (2007) Pre-procedural predictors of atrial fibrillation recurrence after circumferential pulmonary vein ablation. Eur Heart J 28(7): 836-841.

33. Betts TR, Jones M, Wong KC, Qureshi N, Rajappan K, Bashir Y. Feasibility of mitral isthmus and left atrial roof linear lesions using an 8 mm tip cryoablation catheter. J Cardiovasc Electrophysiol. 2013 Jul;24(7):775-80. doi: 10.1111/jce.12129. Epub 2013 Mar 29.

34. Fassini G, Riva S, Chiodelli R, Trevisi N, Berti M, Carbucicchio C, Maccabelli G, Giraldi F, Bella PD: Left mitral isthmus ablation associated with PV isolation: Long-term results of a prospective randomized study. J Cardiovasc Electrophysiol 2005;16:1150-1156.

35. Jais P, Hocini M, Hsu LF, Sanders P, Scavee C, Weerasooriya R, Macle L, Raybaud F, Garrigue S, Shah DC, Le MP, Clementy J, Haissaguerre M: Technique and results of linear ablation at the mitral isthmus. Circulation 2004;110:2996-3002.

36. Ernst G, Stollberger C, Abzieher F et al. Morphology of theft atrial appendage. Anat Rec 1995; 242:553-561.

37. Ho SY, Sanchez-Quintana D, Cabrera JA, Anderson RH. Anatomy of the left atrium: implications for radiofrequency ablation of atrial fibrillation. J Cardiovasc Electrophysiol 1999;10:1525-1533

38. McAlpine WA. In: Heart and coronary arteries, Berlin: Springer–. Br, 1975, pp. 58-59.

39. Burch GE, Romney RB. Functional anatomy and 'throttle valve' action of the pulmonary veins. Am Heart J 1954;47: 58-66.

40. Brunton TL, Fayrer J. Note on independent pulsation of the pulmonary veins and vena cava. Proc Royal Soc Lond 1876–77;25: 174-176.

41. Zipes DP, Knope RF. Electrical properties of the thoracic veins. Am J Cardiol 1972;29:372-376.

42. Jaïs P, Haïssaguerre M, Shah DC, Chouairi S, Clémenty J. Regional disparities of endocardial atrial activation in paroxysmal atrial fibrillation. Pacing Clin Electrophysiol. 1996 Nov;19(11 Pt 2):1998-2003.

43. Haïssaguerre M, Sanders P, Hocini M, Takahashi Y, Rotter M, Sacher F, Rostock T, Hsu LF, Bordachar P, Reuter S, Roudaut R, Clémenty J, Jaïs P. Catheter ablation of long-lasting persistent atrial fibrillation: critical structures for termination. J Cardiovasc Electrophysiol. 2005 Nov;16(11):1125-37.

44. Braunwald E, Brockenbrough EC, Frahm CJ, Ross J. Left atrial and left ventricular pressures in subjects without cardiovascular disease: observations in eighteen patients studied by transseptal left heart catheterization. *Circulation* 1961;24:267-269.

45. Earley MJ. How to perform a transseptal puncture. *Heart* 2008;95:85-92.

46. Hahn K, Gal R, Sarnoski J, Kubota J, Schmidt DH, Bajwa TK. Transesophageal echocardiographically guided atrial transseptal catheterization in patients with normal-sized atria: incidence of complications. *Clin Cardiol* 1995;18:217-220.

47. Daoud EG. Transseptal catheterization. *Heart Rhythm* 2005;2:212-214.

48. Kautzner J, Peichl P. You get what you inspect, not what you expect: can we make the transseptal puncture safer? *Europace* 2010;12:1353-1355.

49. De Ponti R, Cappato R, Curnis A, Della Bella P, Padeletti L, Raviele A, Santini M, Salerno-Uriarte JA. Trans-septal catheterization in the electrophysiology laboratory: data from a multicenter survey spanning 12 years. *J Am Coll Cardiol* 2006;47:1037-1042.

50. McGinty PM, Smith TW, Rogers JH. Transseptal left heart catheterization and the incidence of persistent iatrogenic atrial septal defects. *J Intervent Cardiol* 2011;24:254-263.

51. Sy RW, Klein GJ, Leong-Sit P, Gula LJ, Yee R, Krahn AD, Skanes AC. Troubleshooting difficult transseptal catheterization. *J Cardiovasc Electrophys* 2011;22:723-727.

52. Saitoh T, Izumo M, Furugen A, Tanaka J, Miyata-Fukuoka Y, Guredevan SV, Tolstrup K, Siegel RJ, Kar S, Shiota T. Echocardiographic evaluation of iatrogenic atrial septal defect after catheter-based mitral valve clip insertion. *Am J Cardiol* 2012;109:1787-1791.

53. Fitchet A, Turkie W, Fitzpatrick AP. Transeptal approach to ablation of left-sided arrhythmias does not lead to persisting interatrial shunt: a transesophageal echocardiographic study. *Pacing Clin Electrophysiol* 1998;21:2070-2072.

54. Hammerstingl C, Lickfett L, Jeong KM, Troatz C, Wedekind JA, Tiemann K, Luderitz B, Lewalter T. Persistence of iatrogenic atrial septal defect after pulmonary vein isolation--an underestimated risk? *Am Heart J* 2006;15:362.e1-5.

55. Fagundes RL, Mantica M, De Luca L, Forleo G, Pappalardo A, Avella A, Fraticelli A, Dello Russo A, Casella M, Pelargonio G, Tondo C. Safety of single transseptal puncture for ablation of atrial fibrillation: retrospective study from a large cohort of patients. *J Cardiovasc Electrophysiol* 2007;18:1277-1281.

56. Rillig A, Meyerfeldt U, Kunze M, Birkemeyer R, Miljak T, Jackle S, Hajredini B, Treusch F, Jung W. Persistent iatrogenic atrial septal defect after a single-puncture, double-transseptal approach for pulmonary vein isolation using a remote robotic navigation system: results from a prospective study. *Europace* 2010;12:331-336.

57. Omran H, Hardung D, Schmidt H, Hammerstingl C, Lüderitz B. Mechanical occlusion of the left atrial appendage. *J Cardiovasc Electrophysiol* 2003;14:S56-59.

58. Casale P, Block PC, O'Shea JP, Palacios IF. Atrial septal defect after percutaneous mitral balloon valvuloplasty: immediate results and follow-up. *J Am Coll Cardiol* 1990;15:1300-1304.

59. Cope C. Newer techniques of transseptal left-heart catheterization. *Circulation* 1963;27:758-761.

60. Sur JP, Pagani FD, Moscucci M. Percutaneous closure of an iatrogenic atrial septal defect. *Catheter Cardiovasc Intervent* 2009;73:267-271.

61. Bordachar P, Grenz N, Jais P, Ritter P, Leclercq C, Morgan JM, Gras D, Yang P. Left ventricular endocardial or triventricular pacing to optimize cardiac resynchronization therapy in a chronic canine model of ischemic heart failure. *Am J Physiol: Heart Circ Physiol* 2012;303:H207-215.

62. Van Gelder BM, Houthuizen P, Bracke F. Transseptal left ventricular endocardial pacing: preliminary experience from a femoral approach with subclavian pull-through. *Europace* 2011;13:1454-1458.

63. Himbert D, Brochet E, Radu C, Iung B, Messika-Zeitoun D, Enguerrand D, Bougoin W, Nataf P, Vahanian A. Transseptal implantation of a transcatheter heart valve in a mitral annuloplasty ring to treat mitral repair failure. *Circ Cardiovasc Interv* 2011;4:396-398.

64. Chan NY, Choy CC, Lau CL, Lo YK, Chu PS, Yuen HC, Mok NS, Tsui PT, Lau ST. Persistent iatrogenic atrial septal defect after pulmonary vein isolation by cryoballoon: an under-recognized complication. *Europace* 2011;13:1406-1410.

65. Thiagalingam A, D'Avila A, Foley L, Fox M, Rothe C, Miller D, Malchano Z, Ruskin JN, Reddy VY. Full-color direct visualization of the atrial septum to guide transseptal puncture. *J Cardiovasc Electrophysiol* 2008;19:1310-1315.

66. Elagha AA, Kim AH, Kocaturk O, Lederman RJ. Blunt atrial transseptal puncture using excimer laser in swine. *Catheter Cardiovasc Interv* 2007;70:585-590.

67. Dondelinger RF, Ghysels MP, Brisbois D, Donkers E, Snaps FR, Saunders J, Deviere J. Relevant radiological anatomy of the pig as a training model in interventional radiology. *Eur Radiol* 1998;8:1254-1273.

68. Stella J, Sacks M. On the biaxial mechanical properties of the layers of the aortic valve leaflet. *J Biomech Eng* 2007;129:757-766.

69. Sacks MS, Schoen FJ, Mayer JE. Bioengineering challenges for heart valve tissue engineering. *Ann Rev Biomed Eng* 2009;11:289-313.

70. Nordsletten DA, Niederer SA, Nash MP, Hunter PJ, Smith NP. Coupling multi-physics models to cardiac mechanics. *Prog Biophys Mol Biol* 2011;104:77-88.

71. Reant P, Lafitte S, Jaïs P, Serri K, Weerasooriya R, Hocini M, Pillois X, Clementy J, Haissaguerre M, Roudaut R. Reverse remodeling of the left cardiac chambers after catheter ablation after 1 year in a series of patients with isolated atrial fibrillation. *Circulation* 2005;112:2896-2903.

72. Nikitin NP, Witte KKA, Thackray SDR, Goodge LJ, Clark AL, Cleland JGF. Effect of age and sex on left atrial morphology and function. *Eur J Echocardiog* 2003;4:36-42.

73. Aurigemma GP, Gottdiener JS, Arnold AM, Chinali M, Hill JC, Kitzman D. Left atrial volume and geometry in healthy aging: The Cardiovascular Health Study. *Circ Cardiovasc Imaging* 2009;2:282-289.

74. Eltchaninoff H, Prat A, Gilard M, Leguerrier A, Blanchard D, Fournial G, Iung B, Donzeau-Gouge P, Tribouilloy C, Debrux JL, Pavie A, Gueret P. Transcatheter aortic valve implantation: early results of the FRANCE (FRench Aortic National CoreValve and Edwards) registry. *Eur Heart J* 2011;32:191-197.

75. Smith T, McGinty P, Bommer W, Low RI, Lim S, Fail P, Rogers JH. Prevalence and echocardiographic features of iatrogenic atrial septal defect after catheter-based mitral valve repair with the MitraClip system. *Catheter Cardiovasc Interv* 2012;80:678-685.

76. Hara H, Virmani R, Ladich E, Mackey-Bojack S, titus J, Reisman M, Gray W, Nakamura M, Mooney M, Poulose A, Schwartz RS. Patent foramen ovale: current pathology, pathophysiology, and clinical status. *J Am Coll Cardiol* 2005;46:1768-1776.

77. Ross J Jr, Braunwald E, Morrow AG. Transseptal left atrial puncture; new technique for the measurement of left atrial pressure in man. Am J Cardiol. 1959 May;3(5):653-5. PubMed PMID: 13649591

78. Cope C. Technique for transseptal catheterization of the left atrium: Preliminary report. J Thorac Surg 1959;37:482-486.

79. Winkle RA, Mead RH, Engel G, Patrawala RA. The use of a radiofrequency needle improves the safety and efficacy of transseptal puncture for atrial fibrillation ablation. Heart Rhythm. 2011 Sep;8(9):1411-5. doi: 10.1016/j.hrthm.2011.04.032.Epub 2011 May 6.

80. Veldtman GR, Wilson GJ, Peirone A, et al. Radiofrequency perforation and conventional needle percutaneous transseptal left heart access: pathological features. Catheter Cardiovasc Interv 2005;65: 556-564.

81. Crystal MA, Mirza MA, Benson LN. A radiofrequency transseptal needle: initial animal studies. Catheter Cardiovasc Interv 2010;76:769-773.

82. Benson LN, Nykanen D, Collison A. Radiofrequency perforation in the treatment of congenital heart disease. Catheter Cardiovasc Interv 2002;56:72-82.

83. Shimko N, Savard P, Shah K. Radiofrequency perforation of cardiac tissue: modeling and experimental results. Med Biol Eng Comput 2000;38:575-58.

84. Quallich S, Goff R, Iaizzo P. High-speed visualization of steam pops during radiofrequency ablation, Journal of Medical Devices 8 (2), 020902.

85. Howard S, Quallich S, Benscoter M, Holmgren B, Rolfes C, Iaizzo P, Tissue properties of the fossa ovalis as they relate to transseptal punctures: A translational approach

86. Weerasooriya R, Khairy P, Litalien J, et al. Catheter ablation for atrial fibrillation: are results maintained at 5 years of follow-up? J Am Coll Cardiol 2011;57:160–166.

87. Tilz RR, Rillig A,Thum AM, et al. Catheter ablation of long-standing persistent atrial fibrillation:5-year outcomes of the Hamburg sequential ablation strategy. J Am Coll Cardiol 2012;60:1921–1929.

88. Jais P, Hocini M, Hsu LF, et al. Technique and results of linear ablation at the mitral isthmus. Circulation 2004;110:2996–3002.

89. Tamborero D, Mont L, Berruezo A, et al. Left atrial posterior wall isolation does not improve the outcome of circumferential pulmonary vein ablation for atrial fibrillation: a prospective randomized study. Circ Arrhythm Electrophysiol 2009;2:35–40.

90. Oral H, Chugh A, Lemola K, Cheung P, Hall B, Good E, Han J, Tamirisa K, Bogun F, Pelosi F Jr, Morady F. Noninducibility of atrial fibrillation as an end point of left atrial circumferential ablation for paroxysmal atrial fibrillation: a randomized study. Circulation. 2004 Nov 2;110(18):2797-801. Epub 2004 Oct 25.

91. Haïssaguerre M, Sanders P, Hocini M, Hsu LF, Shah DC, Scavée C, Takahashi Y, Rotter M, Pasquié JL, Garrigue S, Clémenty J, Jaïs P. Changes in atrial fibrillation cycle length and inducibility during catheter ablation and their relation to outcome. Circulation. 2004 Jun 22;109(24):3007-13. Epub 2004 Jun 7.

92. Jaïs P, Hocini M, Hsu LF, Sanders P, Scavee C, Weerasooriya R, Macle L, Raybaud F, Garrigue S, Shah DC, Le Metayer P, Clémenty J, Haïssaguerre M. Technique and results of linear ablation at the mitral isthmus. Circulation. 2004 Nov 9;110(19):2996-3002. Epub 2004 Nov 1.

93. Deisenhofer I, Estner H, Zrenner B, et al. Left atrial tachycardia after circumferential pulmonary vein ablation for atrial fibrillation: incidence, electrophysiological characteristics, and results of radio frequency ablation. Europace 2006; 8:573–582.

94. Chae S, Oral H, Good E, et al. Atrial tachycardia after circumferential pulmonary vein ablation of atrial fibrillation: mechanistic insights, results of catheter ablation, and risk factors for recurrence. J Am Coll Cardiol 2007;50:1781–1787.

95. Mesas CE, Pappone C, Lang CC, et al. Left atrial tachycardia after circumferential pulmonary vein ablation for atrial fibrillation: electro anatomic characterization and treatment. J Am Coll Cardiol 2004;44:1071–1079.

96. Rostock T, O'Neill MD, Sanders P, et al. Characterization of conduction recovery across left atrial linear lesions in patients with paroxysmal and persistent atrial fibrillation. J Cardiovasc Electrophysiol 2006;17:1106–1111.

97. Hill AJ, Laske TG, Coles JA, Jr, Sigg DC, Skadsberg ND, Vincent SA, et al. In vivo studies of human hearts. Ann Thorac Surg 2005;79:168-177.

98. Chinchoy E, Soule CL, Houlton AJ, Gallagher WJ, Hjelle MA, Laske TG, et al. Isolated four-chamber working swine heart model. Ann Thorac Surg 2000;70: 1607-1614.

99. Yokokawa M, Sundaram B, Garg A, Stojanovska J, Oral H, Morady F, Chugh A. Impact of mitral isthmus anatomy on the likelihood of achieving linear block in patients undergoing catheter ablation of persistent atrial fibrillation. Heart Rhythm. 2011 Sep;8(9):1404-10. doi: 10.1016/j.hrthm.2011.04.030. Epub 2011 May 4.

100. Yokokawa M, Sundaram B, Garg A, et al. Impact of mitral isthmus anatomy on the likelihood of achieving linear block in patients undergoing catheter ablation of persistent atrial fibrillation. Heart Rhythm 2011; 8:1404-10.

101. Becker AE. Left atrial isthmus. J Cardiovasc Electrophys 2004; 15: 809–12.

102. Wong KC, Jones M, Sadarmin PP, et al. Larger coronary sinus diameter predicts the need for epicardial delivery during mitral isthmus ablation. Europace 2011; 13:555-61

103. Wong KC, Betts TR. A review of mitral isthmus ablation. Indian Pacing Electrophysiol J 2012; 12:152-70.

104. Aurigemma GP, Gottdiener JS, Arnold AM, Chinali M, Hill JC, Kitzman D. Left atrial volume and geometry in healthy aging: the Cardiovascular Health Study. Circ Cardiovasc Imaging. 2009 Jul;2(4):282-9. doi: 10.1161/CIRCIMAGING.108.826602. Epub 2009 May 11.

105. Schmidt B, Ernst S, Ouyyang F, et al. External and endoluminal analysis of left atrial anatomy and the pulmonary veins in three-dimensional reconstructions of magnetic resonance angiography: the full insight from inside. J Cardiovasc Electrophys 2006; 17: 957–64.

106. Takatsuki S, Extramiana F, Hayashi M, et al. High take-off left inferior pulmonary vein as an obstacle in creating a conduction block at the lateral mitral isthmus. Europace 2009; 11:910-6.

107. Wongcharoen W, Tsao H-M, Wu M-H, et al. Morphologic characteristics of the left atrial appendage, roof, and septum: implications for the ablation of atrial fibrillation. J Cardiovasc Electrophys 2006; 17:951–6.

108. Chiang S-J, Tsao H-M, Wu M-H, et al. Anatomic characteristics of the left atrial isthmus in patients with atrial fibrillation: lessons from computed tomographic images. J Cardiovasc Electrophys 2006; 17:1274–8.

109. Hall B, Jeevanantham V, Simon R, Filippone J, Vorobiof G, Daubert J. Variation in left atrial transmural wall thickness at sites commonly targeted for ablation of atrial fibrillation. J Interv Card Electrophysiol 2006; 17:127-32.

110. Fleming CP, Wang H, Quan KJ, Rollins AM. Real-time monitoring of cardiac radio-frequency ablation lesion formation using an optical coherence tomography forward-imaging catheter. Journal of Biomedical Optics 2010;15(3):030516. doi:10.1117/1.3459134.

111. Chik WW, Barry MA, Thavapalachandran S, Midekin C, Pouliopoulos J, Lim TW, Sivagangabalan G, Thomas SP, Ross DL, McEwan AL, Kovoor P, Thiagalingam A. High spatial resolution thermal mapping of radiofrequency ablation lesions using a novel thermochromic liquid crystal myocardial phantom. J Cardiovasc Electrophysiol. 2013 Nov;24(11):1278-86. doi: 10.1111/jce.12209. Epub 2013 Jul 11.

112. Eggen MD, Bateman MG, Iaizzo PA. Methods to prepare perfusion fixed cardiac specimens for multimodal imaging: the use of formalin and agar gels. J Med Devices 2011; 5:027539.

113. Sandra Fussen1, Bart W.L. De Boeck, Michael J. Zellweger, Jens Bremerich, Kaatje Goetschalckx, Michel Zuber, and Peter T. Buser Cardiovascular magnetic resonance imaging for diagnosis and clinical management of suspected cardiac masses and tumors 1University Hospital Basel, Basel, Switzerland; 2Kantonsspital Luzern, Herzzentrum, 6000 Luzern 16, Switzerland; and 3Gasthuisberg University Hospital, Leuven, Belgium , 15 April 2011

114. Hundley WG, Bluemke DA, Finn JP, Flamm SD, Fogel MA, Friedrich MG, Ho VB, Jerosch-Herold M, Kramer CM, Manning WJ, Patel M, Pohost GM, Stillman AE, White RD, Woodard PK. ACCF/ACR/AHA/NASCI/SCMR 2010 expert consensus document on cardiovascular magnetic resonance: a report of the American College of Cardiology Foundation Task Force on Expert Consensus Documents. J Am Coll Cardiol 2010;55:2614–2662.

115. Narayan SM, Wright M, Derval N, Jadidi A, Forclaz A, Nault I, Miyazaki S,Sacher F, Bordachar P, Clémenty J, Jaïs P, Haïssaguerre M, Hocini M. Classifying fractionated electrograms in human atrial fibrillation using monophasic action potentials and activation mapping: evidence for localized drivers, rate acceleration, and nonlocal signal etiologies. Heart Rhythm. 2011 Feb;8(2):244-53. doi: 10.1016/j.hrthm.2010.10.020. Epub 2010 Oct 16.

116. Gerstenfeld EP, Marchlinski FE. Mapping and ablation of left atrial tachycardias occurring after atrial fibrillation ablation. Heart Rhythm. 2007 Mar;4(3 Suppl):S65-72. Epub 2007 Jan 25.

117. Wood MA. Exposing gaps in linear radiofrequency lesions: form before function. Circ Arrhythm Electrophysiol. 2011 Jun;4(3):257-9. doi: 10.1161/CIRCEP.111.963033.

118. Kobayashi T, Ishikawa T, Sumita S, Yamakawa Y, Ohkusu Y, Matsusita K, Matsumoto K, Nakagawa T, Nakazawa I, Mochida Y, Ebina T, Uchino K, Kimura K, Umemura S. Double-counting of intracardiac electrogram during biatrial pacing. Circ J. 2004 Feb;68(2):131-4.

119. Monophasic action potential mapping in swine and humans using modified-tip ablation catheter and electroanatomic mapping system. Liu S, Yuan S, Hertervig E, Kongstad O, Holm M, Grins E, Olsson SB. Scand Cardiovasc J. 2002 May;36(3):161-6.

120. Franz MR, Burkhoff D, Spurgeon H, Weisfeldt ML, Lakatta EG. In vitro validation of a new cardiac catheter technique for recording monophasic action potentials. Eur Heart J. 1986 Jan;7(1):34-41.

121. Franz MR. Bridging the gap between basic and clinical electrophysiology: what can be learned from monophasic action potential recordings? J Cardiovasc Electrophysiol. 1994 Aug;5(8):699-710.

122. Franz MR, Burkhoff D, Spurgeon H, Weisfeldt ML, Lakatta EG. In vitro validation of a new cardiac catheter technique for recording monophasic action potentials. Eur Heart J. 1986 Jan;7(1):34-41.

123. Aidonidis I, Poyatzi A, Stamatiou G, Lymberi M, Molyvdas PA. Assessment of local atrial repolarization in a porcine acetylcholine model of atrial flutter and fibrillation. Acta Cardiol. 2009 Feb;64(1):59-64.

124. Miller JM, Kowal RC, Swarup V, Daubert JP, Daoud EG, Day JD, Ellenbogen KA, Hummel JD, Baykaner T, Krummen DE, Narayan SM, Reddy VY, Shivkumar K, Steinberg JS, Wheelan KR. Initial independent outcomes from focal impulse and rotor modulation ablation for atrial fibrillation: multicenter FIRM registry. J Cardiovasc Electrophysiol. 2014 Sep;25(9):921-9. doi: 10.1111/jce.12474. Epub 2014 Jul 23.

125. Knollmann BC, Tranquillo J, Sirenko SG, Henriquez C, Franz MR. Microelectrode study of the genesis of the monophasic action potential by contact electrode technique. J Cardiovasc Electrophysiol. 2002 Dec;13(12):1246-52.

126. Franz MR. Current status of monophasic action potential recoding: theories, measurements and interpretations. Cardiovasc Res. 1999 Jan;41(1):25-40.

127. Kongstad O, Xia Y, Liu Y, Liang Y, Olsson B, Yuan S. Ventricular repolarization sequences on the epicardium and endocardium. Monophasic action potential mapping in healthy pigs. J Electrocardiol. 2012 Jan-Feb;45(1):49-56. doi: 10.1016/j.jelectrocard.2011.04.009.

128. Yuan S, Kongstad O, Hertervig E, Holm M, Grins E, Olsson B. Global repolarization sequence of the ventricular endocardium: monophasic action potential mapping in swine and humans. Pacing Clin Electrophysiol. 2001 Oct;24(10):1479-88.

129. S.-G. Yang, O. Kittnar, New Insights Into Application of Cardiac Monophasic Action Potential 1Institute of Physiology, First Faculty of Medicine, Charles University, Prague, Czech Republic, January 15, 2010

130. Narayan SM, Wright M, Derval N, Jadidi A, Forclaz A, Nault I, Miyazaki S, Sacher F, Bordachar P, Clémenty J, Jaïs P, Haïssaguerre M, Hocini M. Classifying fractionated electrograms in human atrial fibrillation using monophasic action potentials and activation mapping: evidence for localized drivers, rate acceleration, and nonlocal signal etiologies. Heart Rhythm. 2011 Feb;8(2):244-53. Epub 2010 Oct 16.

131. Makimoto H, Metzner A, Lin T, Rillig A, Wohlmuth P, Arya A, Antz M, Mathew S, Deiss S, Wissner E, Rausch P, Bardyszewski A, Kamioka M, Li X, Kuck KH, Ouyang F, Tilz RR. Department of Cardiology, Asklepios Klinik St. Georg, Hamburg, Germany. In Vivo Contact Force Analysis and Correlation with Tissue Impedance during Left Atrial Mapping and Catheter Ablation of Atrial Fibrillation. Circ Arrhythm Electrophysiol. 2013 Dec 20.

132. Thiagalingam A, D'Avila A, Foley L, Guerrero JL, Lambert H, Leo G, Ruskin JN, Reddy VY.
Importance of catheter contact force during irrigated radiofrequency ablation: evaluation in a porcine ex vivo model using a force-sensing catheter. J Cardiovasc Electrophysiol. 2010 Jul;21(7):806-11. doi: 10.1111/j.1540-8167.2009.01693.x.

133. Okumura Y, Johnson SB, Bunch TJ, Henz BD, O'Brien CJ, Packer DL.
A systematical analysis of in vivo contact forces on virtual catheter tip/tissue surface contact during cardiac mapping and intervention. J Cardiovasc Electrophysiol. 2008 Jun;19(6):632-40. doi: 10.1111/j.1540-8167.2008.01135.x.

134. Iaizzo PA, Hill AJ, Laske TG: Cardiac device testing enhanced by simultaneous imaging modalities: the Visible Heart®, fluoroscopy, and echocardiography. *Expert Review of Medical Devices* 5:51-58, 2008.

135. Chinchoy E, Soule CL, Houlton AJ, Gallagher WJ, Hjelle MA, Laske TG, Morissette J, Iaizzo PA. Isolated four-chamber working swine heart model. Ann Thorac Surg. 2000 Nov;70(5):1607-14.

136. Mark T. Stewart, Mark Allen Benscoter, Jon Virgil Evans, Timothy G. Laske, Gonzalo Martinez, 2013. Electrophysiology catheter design. US 20140052119, filed Jan 25, 2013

137. Goto E, Nakamura K, Sasaki T, Naito S. Successful Ablation of Cavotricuspid Isthmus-dependent Atrial Flutter Guided by Contact Force Vector in a Patient

After a Tricuspid Valve Replacement. Indian Pacing Electrophysiol J. 2014 Dec 15;14(6):306-8. eCollection 2014 Nov-Dec.

138. Sacher F, Wright M, Derval N, Denis A, Ramoul K, Roten L, Pascale P, Bordachar P, Ritter P, Hocini M, Dos Santos P, Haissaguerre M, Jais P. Endocardial versus epicardial ventricular radiofrequency ablation: utility of in vivo contact force assessment. Circ Arrhythm Electrophysiol. 2013 Feb;6(1):144-50. doi: 10.1161/CIRCEP.111.974501. Epub 2013 Feb 7.

139. Ullah W, Hunter RJ, McLean A, Dhinoja M, Earley MJ, Sporton S, Schilling RJ. Impact of Steerable Sheaths on Contact Forces and Reconnection Sites in Ablation for Persistent Atrial Fibrillation. J Cardiovasc Electrophysiol. 2014 Oct 27. doi: 10.1111/jce.12573. [Epub ahead of print]

140. Matía Francés R, Hernández Madrid A, Delgado A, Carrizo L, Pindado C, Moro Serrano C, Zamorano Gómez JL. Characterization of the impact of catheter-tissue contact force in lesion formation during cavo-tricuspid isthmus ablation in an experimental swine model. Europace. 2014 Nov;16(11):1679-83. doi: 10.1093/europace/eut351. Epub 2013 Nov 13.

141. Jaïs P, Hocini M, Hsu LF, Sanders P, Scavee C, Weerasooriya R, Macle L, Raybaud F, Garrigue S, Shah DC, Le Metayer P, Clémenty J, Haïssaguerre M. Technique and results of linear ablation at the mitral isthmus. Circulation. 2004 Nov 9;110(19):2996-3002. Epub 2004 Nov 1.

142. Tamborero D, Mont L, Berruezo A, Matiello M, Benito B, Sitges M, Vidal B, de Caralt TM, Perea RJ, Vatasescu R, Brugada J. Left atrial posterior wall isolation does not improve the outcome of circumferential pulmonary vein ablation for atrial fibrillation: a prospective randomized study. Circ Arrhythm Electrophysiol. 2009 Feb;2(1):35-40. doi: 10.1161/CIRCEP.108.797944. Epub 2008 Dec 3.

143. Deisenhofer I, Estner H, Zrenner B, Schreieck J, Weyerbrock S, Hessling G, Scharf K, Karch MR, Schmitt C. Left atrial tachycardia after circumferential pulmonary vein ablation for atrial fibrillation: incidence, electrophysiological characteristics, and results of radiofrequency ablation. Europace. 2006 Aug;8(8):573-82.

144. Chae S, Oral H, Good E, Dey S, Wimmer A, Crawford T, Wells D, Sarrazin JF, Chalfoun N, Kuhne M, Fortino J, Huether E, Lemerand T, Pelosi F,

Bogun F, Morady F, Chugh A. Atrial tachycardia after circumferential pulmonary vein ablation of atrial fibrillation: mechanistic insights, results of catheter ablation, and risk factors for recurrence. J Am Coll Cardiol. 2007 Oct 30;50(18):1781-7. Epub 2007 Oct 15.

145. Mesas CE, Pappone C, Lang CC, Gugliotta F, Tomita T, Vicedomini G, Sala S, Paglino G, Gulletta S, Ferro A, Santinelli V. Left atrial tachycardia after circumferential pulmonary vein ablation for atrial fibrillation: electroanatomic characterization and treatment. J Am Coll Cardiol. 2004 Sep 1;44(5):1071-9.

146. Rostock T, O'Neill MD, Sanders P, Rotter M, Jaïs P, Hocini M, Takahashi Y, Sacher F, Jönsson A, Hsu LF, Clémenty J, Haïssaguerre M. Characterization of conduction recovery across left atrial linear lesions in patients with paroxysmal and persistent atrial fibrillation. J Cardiovasc Electrophysiol. 2006 Oct;17(10):1106-11. Epub 2006 Aug 14.

147. Ranjan R, Kato R, Zviman MM, Dickfeld TM, Roguin A, Berger RD, Tomaselli GF, Halperin HR. Gaps in the ablation line as a potential cause of recovery from electrical isolation and their visualization using MRI. Circ Arrhythm Electrophysiol. 2011 Jun;4(3):279-86. doi: 10.1161/CIRCEP.110.960567. Epub 2011 Apr 14.

148. Gerstenfeld EP, Marchlinski FE. Mapping and ablation of left atrial tachycardias occurring after atrial fibrillation ablation. Heart Rhythm. 2007 Mar;4(3 Suppl):S65-72. Epub 2007 Jan 25. Review.

149. Wood MA. Exposing gaps in linear radiofrequency lesions: form before function. Circ Arrhythm Electrophysiol. 2011 Jun;4(3):257-9. doi: 10.1161/CIRCEP.111.963033.

150. Hill AJ, Laske TG, Coles JA, Jr, Sigg DC, Skadsberg ND, Vincent SA, et al. In vivo studies of human hearts. Ann Thorac Surg 2005;79:168-177.

151. Chinchoy E, Soule CL, Houlton AJ, Gallagher WJ, Hjelle MA, Laske TG, et al. Isolated four-chamber working swine heart model. Ann Thorac Surg 2000;70: 1607-1614.

152. Kongstad O, Xia Y, Liu Y, Liang Y, Olsson B, Yuan S., Ventricular repolarization sequences on the epicardium and endocardium. Monophasic action potential mapping in healthy pigs. J Electrocardiol. 2012 Jan-Feb;45(1):49-56.

doi: 10.1016/j.jelectrocard.2011.04.009. Epub 2011 Jun 22.

153. Haïssaguerre M, Sanders P, Hocini M, Takahashi Y, Rotter M, Sacher F, Rostock T, Hsu LF, Bordachar P, Reuter S, Roudaut R, Clémenty J, Jaïs P. Catheter ablation of long-lasting persistent atrial fibrillation: critical structures for termination. J Cardiovasc Electrophysiol. 2005 Nov;16(11):1125-37.

154. Aidonidis I, Poyatzi A, Stamatiou G, Lymberi M, Molyvdas PA. Assessment of local atrial repolarization in a porcine acetylcholine model of atrial flutter and fibrillation. Acta Cardiol. 2009 Feb;64(1):59-64.

155. Narayan SM, Wright M, Derval N, Jadidi A, Forclaz A, Nault I, Miyazaki S, Sacher F, Bordachar P, Clémenty J, Jaïs P, Haïssaguerre M, Hocini M. Classifying fractionated electrograms in human atrial fibrillation using monophasic action potentials and activation mapping: evidence for localized drivers, rate acceleration, and nonlocal signal etiologies. Heart Rhythm. 2011 Feb;8(2):244-53. Epub 2010 Oct 16.